SINGLE AND DUAL BAND QUANTUM WELL INFRARED
PHOTODETECTOR FOCAL PLANE ARRAYS ON InP SUBSTRATES

A THESIS SUBMITTED TO
THE GRADUATE SCHOOL OF NATURAL AND APPLIED SCIENCES
OF
MIDDLE EAST TECHNICAL UNIVERSITY

BY

SÜLEYMAN UMUT EKER

IN PARTIAL FULFILLMENT OF THE REQUIREMENTS
FOR
THE DEGREE OF DOCTOR OF PHILOSOPHY
IN
ELECTRICAL AND ELECTRONICS ENGINEERING

FEBRUARY 2010

Approval of the thesis:

**SINGLE AND DUAL BAND QUANTUM WELL INFRARED
PHOTODETECTOR FOCAL PLANE ARRAYS ON InP SUBSTRATES**

submitted by **SÜLEYMAN UMUT EKER** in partial fulfillment of the requirements for the degree of **Doctor of Philosophy in Electrical and Electronics Engineering Department, Middle East Technical University** by,

Prof. Dr. Canan Özgen   _____
Dean, Graduate School of **Natural and Applied Sciences**

Prof. Dr. İsmet Erkmen   _____
Head of Department, **Electrical and Electronics Engineering**

Prof. Dr. Cengiz Beşikçi   _____
Supervisor, **Electrical and Electronics Engineering Department, METU**

Examining Committee Members:

Prof. Dr. Tayfun Akın   _____
Electrical and Electronics Engineering Dept., METU

Prof. Dr. Cengiz Beşikci   _____
Electrical and Electronics Engineering Dept., METU

Prof. Dr. Mehmet Parlak   _____
Physics Dept., METU

Prof. Dr. Yüksel Ergun   _____
Physics Dept., Anadolu University

Assoc. Prof. Dr. Haluk Külah   _____
Electrical and Electronics Engineering Dept., METU

Date: 05.02.2010

I hereby declare that all information in this document has been obtained and presented in accordance with academic rules and ethical conduct. I also declare that, as required by these rules and conduct, I have fully cited and referenced all material and results that are not original to this work.

Name, Last name: SÜLEYMAN UMUT EKER

Signature   :

ABSTRACT

SINGLE AND DUAL BAND QUANTUM WELL INFRARED PHOTODETECTOR FOCAL PLANE ARRAYS ON InP SUBSTRATES

EKER, Süleyman Umut

Ph.D., Department of Electrical and Electronics Engineering

Supervisor: Prof. Dr. Cengiz BEŞİKCİ

February 2005, 116 pages

Excellent uniformity and mature material properties of Quantum Well Infrared Photodetectors (QWIPs) have allowed the realization of large format, low cost staring focal plane arrays (FPAs) in various thermal imaging bands. AlGaAs/InGaAs and AlGaAs/GaAs materials systems have been the standard systems for the construction of mid-wavelength infrared (MWIR) and long-wavelength (LWIR) QWIPs. However AlGaAs/GaAs QWIP FPAs suffer from low quantum and conversion efficiencies under high frame rate (low integration time) and/or low background conditions limiting the application area of standard QWIPs. This thesis focuses on the growth and development of InP based single and dual band QWIP FPAs. We experimentally demonstrate that QWIPs on InP substrates provide important advantages that can be utilized to overcome the bottlenecks of the standard GaAs based QWIP technology.

InP/InGaAs material system is an alternative to AlGaAs/GaAs for LWIR QWIPs. We demonstrate a large format (640x512) LWIR QWIP FPA constructed with strained InP/InGaAs material system. The strain introduced to the structure shifts the

iv

cut-off wavelength from ~8.5 to 9.7 μm with λ_p=8.9 μm. The FPA fabricated with the 40-well epilayer structure yielded a peak quantum efficiency as high as 12% with a broad spectral response ($\Delta\lambda/\lambda_p$=17%). The peak responsivity of the FPA pixels is larger than 1.4 A/W with conversion efficiency as high as 20% in the bias region where the detectivity is reasonably high (2.6×10^{10} cmHz$^{1/2}$/W, f/1.5, 65 K). The FPA providing a background limited performance temperature higher than 65 K (f/1.5) satisfies the requirements of most low integration time/low background applications where AlGaAs/GaAs QWIPs cannot be utilized due to low conversion efficiency and read-out circuit noise limited sensitivity. Noise equivalent temperature differences (NETD) of the FPA are as low as 19 and 40 mK with integration times as short as 1.8 ms and 430 μs (f/1.5, 65 K), respectively.

We also experimentally demonstrate that the cut-off wavelength of MWIR AlInAs/InGaAs QWIPs can be tuned in a sufficiently large range in the MWIR atmospheric window by only changing the quantum well (QW) width at the lattice matched composition. The cut-off wavelength can be shifted up to ~5.0 μm with a QW width of 22 Å in which case very broad spectral response ($\Delta\lambda/\lambda_p$=~30%) and a reasonably high peak detectivity is achievable leading to a NETD as low as 14 mK (f/2) with 25 μm pitch in a 640x512 FPA.

The advantages of InP based MWIR and LWIR single band QWIPs were combined by growing and fabricating a mid format (320x256) dual band QWIP FPA. The FPA provided NETD (f/1.5, 65 K, 19 ms) values of 27 mK and 29 mK in the MWIR and LWIR modes with an impressively low DC signal nonuniformity of ~ 4%.

The results clearly demonstrate that InP based material systems display high potential for MWIR and LWIR single band and MWIR/LWIR dual band QWIP FPAs needed by third generation thermal imagers by overcoming the limitations of the standard GaAs based QWIPs under high frame rate (low integration time) and/or low background conditions.

Keywords: QWIP, MWIR, LWIR, Dual band, Three-contact FPA

ÖZ

InP TABAN ÜZERİNDE TEK VE İKİ BANTLI KUANTUM KUYULU KIZILÖTESİ FOTODEDEKTÖR ODAK DÜZLEM MATRİSLERİ

EKER, Süleyman Umut

Doktora, Elektrik Elektronik Mühendisliği Bölümü

Tez Danışmanı: Prof. Dr. Cengiz BEŞİKCİ

Şubat 2005, 116 sayfa

Kuantum Kuyulu Kızılötesi Fotodedektörlerin (KKKF) yüksek homojenlik ve olgun malzeme özellikleri, çeşitli termal görüntüleme bantlarında geniş formatlı ve düşük maliyetli taramasız odak düzlem matrislerinin (ODM) gerçeklenmesine olanak sağlamıştır. Orta dalgaboyu kızılötesi (ODK) ve uzun dalgaboyu kızılötesi (UDK) KKKF'lerin yapımında AlGaAs/InGaAs ve AlGaAs/GaAs malzeme sistemleri standart sistemler olmuştur. Bununla birlikte AlGaAs/GaAs KKKF'lerin yüksek resim hızlarında (düşük entegrasyon zamanı) ve/veya düşük arkaplan durumlarında düşük kuantum ve çevirim verimliliğinden dolayı kalitesi düşmekte ve standart KKKF'lerin uygulama alanları sınırlanmaktadır. Bu tez, InP tabanlı tek ve çift bantlı KKKF ODMlerin büyütlmesi ve geliştirilmesine odaklanmıştır. InP taban üzerindeki KKKF'lerin, standart GaAs tabanlı KKKF teknolojisinin tıkanıklıklarının üstesinden gelmek için kullanılabileceği deneysel olarak gösterilmiştir.

UDK KKKFler için InP/InGaAs mazleme sistemi AlGaAs/GaAs malzeme sistemine bir alternatiftir. Gerilimli InP/InGaAs malzeme sitemi ile yapılmış geniş formatlı (640x512) UDK KKKF ODM gösterilmiştir. Yapıya katılan gerilim, kesim

dalgaboyunu ~8.5 μm'den λ_p=8.9 μm olacak şekilde 9.7 μm'ye kaydırmıştır. 40 kuyulu epikatman yapısıyla üretilen ODM, geniş bir spektral tepkisellik ($\Delta\lambda/\lambda_p$=17%) ile %12 kadar yüksek tepe kuantum verimliliği vermiştir. ODM pikselleri, hassasiyetin yeteri kadar yüksek olduğu gerilim aralığında (2.6x10^{10} cmHz$^{1/2}$/W, f/1.5, 65 K) 1.4 A/W'dan daha yüksek tepe tepkiselliği ve %20 kadar yüksek çevirim verimliliği göstermiştir. ODM, 65 K'den daha yüksek sıcaklıklarda (f/1.5) arka plan sınırlı performans sağlayarak AlGaAs/GaAs KKKF'lerin düşük çevirim verimliliğinden ve okuma devresi gürültü sınırlı duyarlılıktan dolayı kalitesinin düştüğü bir çok düşük entegrasyon zamanı/düşük arka plan uygulamalarının gereksinimlerini sağlamıştır. ODM'nin gürültü eşdeğer sıcaklık farkları (GESF) 1.8 ms ve 430 μs gibi kısa entagrasyon zamanlarıyla sırasıyla, 19 ve 40 mK kadar düşüktür (f/1.5, 65K).

Aynı zamanda ODK AlInAs/InGaAs KKKF'lerin kesim dalga boylarının ODK atmosferik penceresinde yeteri kadar geniş bir aralıkta, örgü uyumlu kompozisyonda sadece kuantum kuyusunun (KK) kalınlığını değiştirerek ayarlanabildiği deneysel olarak gösterilmiştir. Kesim dalga boyu 22 Å KK kalınlığı ile ~5.0 μm'ye ötelenmiştir ve bu durumda çok geniş bir spektral tepkisellik ($\Delta\lambda/\lambda_p$=~30%) ve 640x512 ODM'de 25 μm pitch ile 14 mK (f/2) kadar düşük GESF'ye yol açan oldukça yüksek tepe dedektivite değerleri elde edilmiştir.

InP tabanlı ODK ve UDK tek bantlı KKKFlerin avantajı, orta formatlı (320x256) çift bantlı KKKF ODM büyütülerek ve üretilerek birleştirilmiştir. ODM, ODK ve UDK modlarında 27 mK ve 29 mK GESF (f/1.5, 65 K, 19 ms) sağlamıştır ve ~ 4% olan DC sinyal düzgünsülüğü etkileyici bir şekilde düşüktür.

Sonuçlar, InP tabanlı malzeme sisteminin, standart GaAs tabanlı KKKM'lerin yüksek resim hızı (düşük entegrasyon zamanı) ve/veya düşük arkaplan durumlarındaki sınırlamalarının üstesinden gelerek, ODK ve UDK tek bantlı ve ODK/UDK çift bantlı KKKF ODM'lerin üçüncü nesil termal görüntüleyiciler için yüksek potansiyelini ortaya koymuştur.

Anahtar Kelimlere: KKKF, ODK, UDK, Çift bant, Üç kontaklı ODM

To Ezgi and my family

ACKNOWLEDGMENTS

TABLE OF CONTENTS

LIST OF TABLES

TABLES

LIST OF FIGURES

FIGURES

LIST OF ABBREVIATIONS

ABBREVIATIONS

AlGaAs   Aluminium Gallium Arsenide

AlInAs   Aluminium Indium Arsenide

BEP   Beam Equivalent Pressure

BLIP   Background Limited Performance

C-QWIP   Corrugated Quantum Well Infrared Photodetector

FPA   Focal Plane Array

FTIR   Fourier Transform Infrared Spectroscopy

FWHM   Full Width Half Maximum

GaAs   Gallium Arsenide

GaSb   Gallium Antimonide

G-R   Generation Recombination

HgCdTe   Mercury Cadmium Telluride

HRXRD   High Resolution X-Ray Diffractometry

ICP-RIE   Inductively Coupled Plasma-Reactive Ion Etcher

InAs   Indium Arsenide

InGaAs   Indium Gallium Arsenide

InP   Indium Phosphide

IR   Infrared

LWIR   Long-Wavelength İnfrared

MBE   Molecular Beam Epitaxy

MCT   Mercury Cadmium Telluride

METU   Middle East Technical University

MQW   Multi Quantum Well

MWIR   Mid-Wavelength Infrared

NEP   Noise Equivalent Power

NETD   Noise Equivalent Temperature Difference

NIR   Near Infrared

PBN   Pyrolytic Boron Nitride

PECVD   Plasma Enhanced Chemical Vapor Deposition

QDIP   Quantum Dot Infrared Photodetector

QW   Quantum Well

QWIP   Quantum Well Infrared Photodetector

RHEED   Reflection High Energy Electron Diffraction

ROIC   Read-Out Integrated Circuit

SLS   Strained Layer Superlattice

SNR   Signal-To-Noise Ratio

SWIR   Short-Wavelength Infrared

TCR   Temperature Coefficient Of Resistance

UHV   Ultra High Vacuum

VLWIR   Very Long-Wavelength Infrared

CHAPTER 1

INFRARED RADIATION

1.1. History of Infrared

Infrared radiation is a kind of electromagnetic radiation whose wavelength spans from 750 nm to 100 μm of electromagnetic spectrum. It has been first discovered by Sir William Herschel while searching for an optical filter material for telescopes to reduce the brightness of sun during solar observations. He repeated Newton's prism experiment while being interested with the heating effect rather than the visual distribution of the spectrum. He used a mercury-in glass thermometer to measure the temperature at different wavelengths of spectrum [1]. As he moved the thermometer beyond the red end of the visible spectrum, he noticed a significant increase at the temperature. When Herschel revealed his discovery in 1800, he called this portion of the electromagnetic spectrum "thermometrical spectrum". Later on, this part of spectrum was named as "Infrared" [1].

Following Sir William Herschel's work, Seebeck discovered the thermoelectric effect in 1821 and demonstrated the first thermocouple. Several years later, in 1829, Nobili constructed a thermopile by connecting a number of thermocouples in series [2]. In 1856, Charles Piazzi Smyth was able to detect Infrared (IR) radiation from moon with the help of a thermocouple [2].

The development in the field of infrared detection resulted in the discovery of the first bolometer by Longley in 1880. His first bolometer was using two thin ribbons of platinum foil as a part of a Wheatstone bridge. He kept working on improving the performance of his bolometer in the following years and achieved 400 times higher sensitive bolometer. He was able to detect the IR radiation of a cow from a quarter of

mile [2]. The work in IR area had not reached a significant level until breakthroughs were achieved in highly sensitive novel IR detector materials in late 1950s.

Photon detectors were developed during the second half of the 20th century. In 1917, Case developed the first photoconductor [2]. This was followed by the invention of lead sulfide by Kutzscher in 1933 [2]. Following these developments, many materials were investigated for IR detection. Especially, during the World War II, modern IR detectors were originated. The successful and rapid progress in IR sensing area has lead to commercializing of high performance photon detectors. Single pixel photoconductive detectors have been replaced by staring arrays in the last five decades.

1.2 Theory of Infrared Radiation

Every object whose temperature is greater than absolute zero Kelvin emits radiation. The power and the energy of this radiation are directly related to the object's temperature, and these quantities are determined by Planck's Law of Radiation.

1.2.1 Planck's Law of Radiation

A blackbody is defined as an object which absorbs all the radiation impinges on it at any wavelength. According to Kirchhoff's Law, the emissivity of a body or a surface must be equal to its absorptivity at thermal equilibrium. Thus, a blackbody has an emissivity (ε) of 1. Emissivity is defined as the ratio of total energy emitted by a material at temperature T to the total energy emitted by an equivalent blackbody at the same temperature. The spectral photon exitance (M_p) of a blackbody at a specific temperature T is described by Planck's Law

$$M_p = \frac{2\pi h c^2}{\lambda^5 (e^{\frac{hc}{\lambda kT}} - 1)} \qquad (1.1)$$

where c is the speed of light, h is the Planck's constant and k is the Boltzmann's constant. Figure 1.1 shows the spectral photon exitance of blackbody at various temperatures. It is clearly seen from the figure that the peak radiation wavelength shifts to shorter wavelengths as the temperature of the blackbody increases. The peak

radiation wavelength is directly related to blackbody temperature, and it is defined by Wien's Displacement Law. By differentiating Planck's Law with respect to λ and finding the maximum, we obtain the maximum radiation wavelength as

$$\lambda_{max} = \frac{2898}{T} \, (\mu m) \qquad (1.2)$$
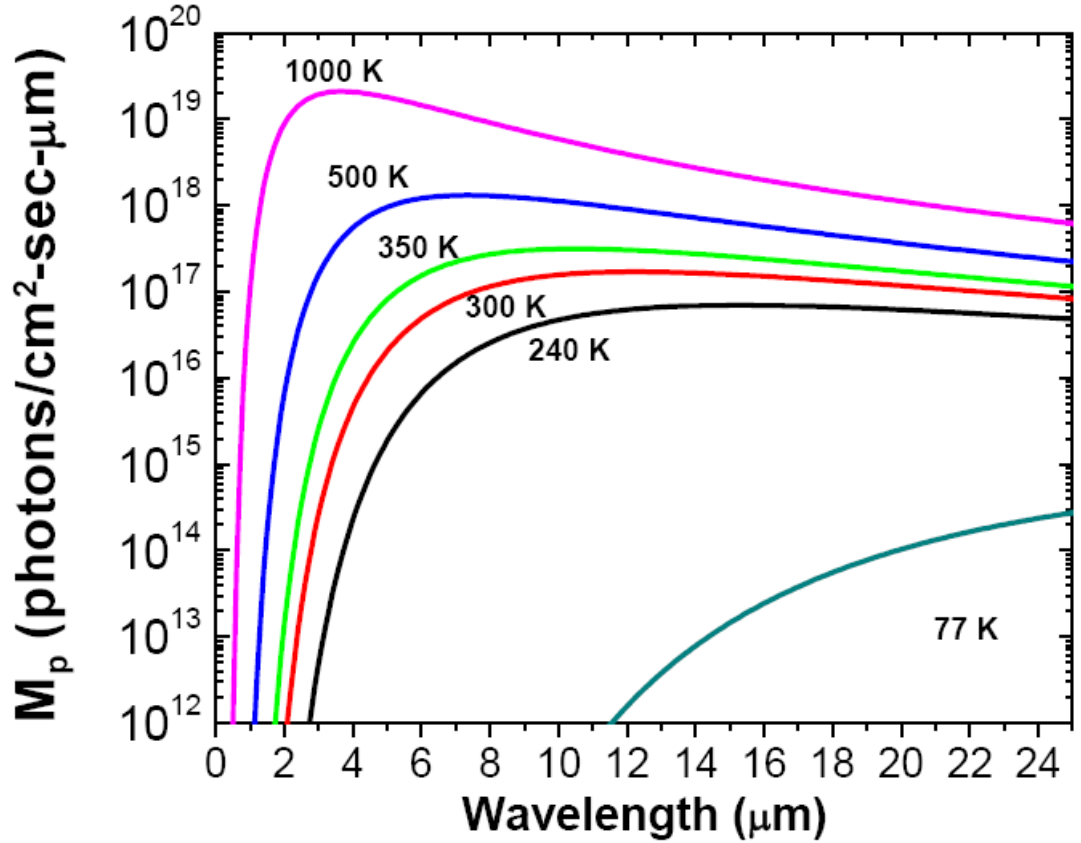
Figure 1.1 Spectral photon exitance of blackbody at various temperatures [3]

1.2.2 Atmospheric Transmission

The photons emitted from a matter propagate through the atmosphere in the form of electromagnetic waves. However, atmosphere is not completely transparent, and the power of the radiation is attenuated with distance. Either scattering from the particles or absorption by the molecules may cause this attenuation. The main gasses which absorb the IR radiation in the atmosphere are H_2O, CO_2 and O_3. The effect of H_2O (water vapor) is dominant on the performance of the infrared imaging systems as the

3

water vapor concentration in the atmosphere varies dramatically depending on the geographical condition and weather. Figure 1.2 shows the transmission of the atmosphere in the IR spectrum. As seen from Figure 1.2, there are some wavelengths where atmosphere's transmission is high which are called as atmospheric windows.
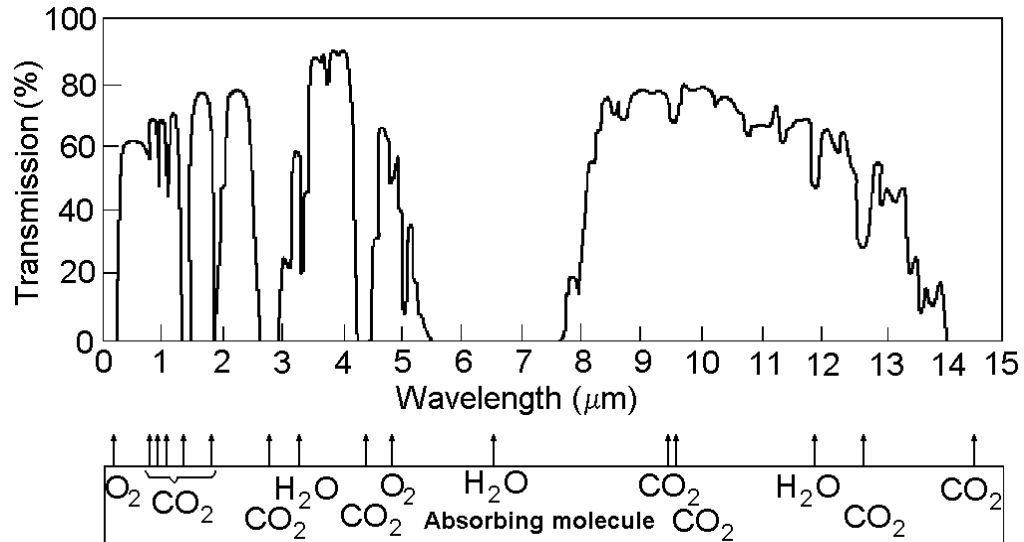
Figure 1.2 Transmission of atmosphere vs. wavelength. Spectrum was measured at sea level and through 6000 ft horizontal path [4]

The atmospheric windows are classified in the literature as follows [5]:

- Near Infrared (NIR): 0.75 to 1.4 μm.
- Short Wavelength Infrared (SWIR): 1.4 to 3 μm.
- Mid Wavelength Infrared (MWIR): 3 to 8 μm.
- Long Wavelength Infrared (LWIR): 8 to 14 μm.
- Very Long Wavelength Infrared (VLWIR): 14 to 1000 μm.

NIR and SWIR windows are sometimes called "reflected infrared" as reflection of light is needed for imaging in these windows. On the other hand, MWIR and LWIR windows are called "thermal infrared" where imaging is performed by directly sensing the photons emitted by the objects. For the purpose of thermal imaging over long distances, 3 to 5 μm band of MWIR window and 8 to 12 μm band of LWIR window are extremely important as near room temperature objects emit sufficient number of photons, and the atmospheric transmission is high enough in these bands. However, each band has advantages and disadvantages with respect to other. The photon flux of near room temperature objects is considerably higher in the LWIR band when compared to MWIR band, and LWIR band is less sensitive to scattering

form molecules as scattering rate is inversely proportional to the radiation wavelength. However, hot targets such as missiles and exhaust gases emit more photons in the MWIR band. On the other hand, IR radiation is less absorbed by water vapor in the MWIR band when compared to LWIR band. Also, in the MWIR band, thermal contrast, which is defined as the percent change in the emitted flux for one Kelvin change in target temperature, is two times larger than that in LWIR band. As a result, depending on the environmental conditions, sometimes MWIR band sometimes LWIR band becomes more useful for thermal imaging.

1.2.3 Components of Thermal Imaging Systems

Thermal imaging systems extend our vision from NIR to VLWIR by making the photons emitted from objects visible. A typical thermal imaging system consists of a detector which converts the infrared radiation to electric signals, a cold stop to define the field of view of the detector, a lens to form the image on the detector and electronics to drive and read the data from the readout integrated circuit (ROIC). This typical scheme is illustrated in Figure 1.3.
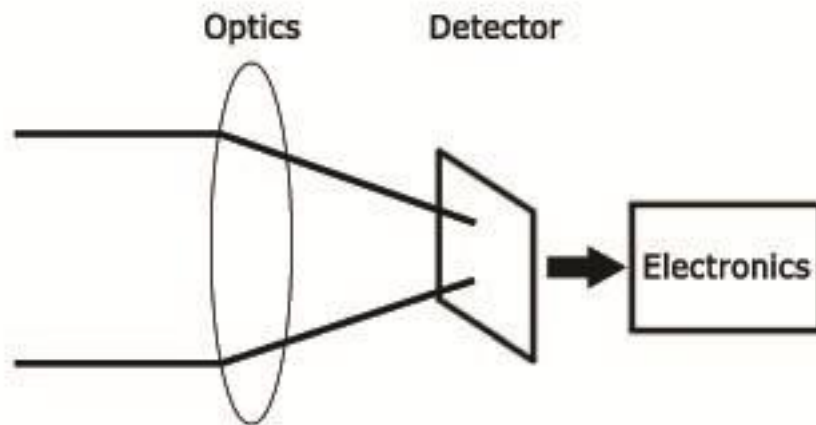
Figure 1.3 Schematic illustration of a thermal imaging system

Materials used to build optics must be selected properly to allow the transmission of IR radiation through it. The most popular materials for IR lens production are amorphous material transmitting IR radiation (AMTIR), germanium (Ge), silicon (Si), zinc selenide (ZnSe), and sapphire. Every material has its own characteristic

transmission. In order to make this transmission nearly 100%, lenses are coated with anti-reflection material optimized for the desired wavelength band.

1.3 Types of Infrared Detectors

An infrared detector is a transducer which converts the IR radiation into electric signal. There are many types of IR detectors, and they can be classified in two main groups based on the detection principle.

     1. Thermal Detectors

     2. Photon Detectors

1.3.1 Thermal Detectors

Thermal detectors use IR radiation as heat source. They mostly deal with the power of the incoming radiation rather than the wavelength as their sensitivity is independent of wavelength. The physical properties of the detector material change as the detector is heated up by IR radiation. This change is converted to electrical signals and sensed by an electronic circuitry. Thermal detectors do not need cryogenic cooling. However, they suffer from low detection capability and slow response time. However, thermal detectors, being low cost, light and compact, are good candidates for low cost/low performance thermal imaging systems. Thermocouple, thermopile, bolometer, pneumatic detectors and pyroelectric detectors are the most common thermal detectors. Among all these detectors, bolometers have achieved the best performance.

Bolometer Bolometers operate based on the principle of conductivity change through absorption of incoming radiation. This temperature-induced change in the conductivity is measured with a suitable circuitry. An active layer, whose temperature coefficient of resistance (TCR) is high, is deposited on a suspended bridge structure in a microbolometer which is a special type of bolometer used as a detector in thermal imaging systems. The most common active layer used in microbolometers is VO_x. VO_x has a high TCR value of 2-3%/K [6]. Today, focal plane arrays (FPAs) with 640×480 resolution and 17 µm pitch are available in

6

commercial market. These FPAs can achieve Noise Equivalent Temperature Difference (NETD) values of 50 mK with $f/1$ optics [7].

Thermocouples and Thermopiles Thermocouples are formed by joining two different materials at one end. Their operation principle is based on Seebeck effect. When two different materials are joined at one end and heated up, there will be a self generated voltage difference at the open end of the materials. The magnitude of the self generated voltage is directly proportional to the difference of Seebeck coefficients of the two materials. Usually, the voltage generated by a single thermocouple can not be measured accurately. Thus, multiple thermocouples are connected in series to increase the output voltage. This new structure is called thermopile. Even though the thermopile based imaging arrays are easy to implement and inexpensive, they suffer from long response time, low responsivity, low resolution/large pixel size and moderately high NETD values (~500 mK) [6,8].

Pneumatic Detector The pneumatic IR detector is first discovered by Golay [9]. It consists of a cavity filled by a gas, and closed at one side by a flexible membrane. The trapped gas is heated by contact with an absorbing layer and expands inducing a deflection of the membrane. By measuring this deflection, the amount of the impinging IR radiation can be measured [9].

Pyroelectric Detector Pyroelectricity is defined as the ability of a polar material to generate a temporary electrical potential when heated. This potential can be measured with the help of two probes which are installed between the opposite faces of the material if the incoming IR radiation is modulated. There are FPAs with 320×240 pixels based on pyroelectric detectors with an NETD value of 40 mK [10].

1.3.2 Photon Detectors

Photon detectors absorb infrared photons and these photons generate free electron-hole pairs. The generated free carriers are then collected at the contacts with the help of an electric field which is applied externally or built internally. The IR photons' energy is small and is comparable with room temperature phonon energy. Thus, photon detectors need to be cooled down to cryogenic temperatures in order to get

rid of phonon interactions. On the other hand, photon detectors show wavelength dependent absorption, fast response time and superior signal to noise ratio once cooled down to cryogenic temperatures. Photon detectors are mainly grouped as photovoltaic and photoconductor detectors. In photovoltaic detectors, the free carriers are collected at the contacts with the help of a built-in electric field. The most general example for this kind of detectors is the p-n junction photodiodes. Beside this, photovoltaic quantum well infrared photodetectors are also reported in the literature [11]. On the other hand, the carrier collection process is done with an external applied bias in photoconductor detectors. Photon detectors may be further divided into several subgroups depending on the interaction way of electrons and photons. The most important types are: intrinsic detectors, extrinsic detectors, photoemissive (metal silicide Schottky barriers) detectors and quantum well detectors [12].

Intrinsic Detectors Intrinsic detector is a type of semiconductor sensor which generates free electron-hole pairs through the absorption of incoming radiation across the bandgap of the semiconductor. Thus, the cut-off wavelength is determined by the bandgap of the material. PbS, PbSe, PbSnTe, HgCdTe, InGaAs, InSb and InAsSb are the most commonly used semiconductor alloys for intrinsic detectors. Among these, InSb and $Hg_xCd_{1-x}Te$ are the most commonly used intrinsic detectors. InSb is a binary material, and it is easy to grow. However, its cutoff wavelength is fixed to 5.5 μm, and dual color detection is not possible with this material system. On the other hand, it has the advantage of well developed and mature technology. $Hg_xCd_{1-x}Te$ has the highest overall performance compared to all other detector types and technology, but it still has some problems. The band gap of $Hg_xCd_{1-x}Te$ is easily tailored by changing the composition of Hg in the ternary alloy. Nonetheless, the bandgap of the $Hg_xCd_{1-x}Te$ is very much dependent to Hg mol fraction especially in the LWIR window. This introduces a high nonuniformity to the detector material which leads to the lack of large format staring arrays. The advantages and disadvantages of various intrinsic detectors are listed in Table 1.1.

Table 1.1 Comparison of the intrinsic detector materials [12].

Detector Type	Advantages	Disadvantages
PbS, PbSe, PbSnTe	• Easy to prepare • Stable materials	• High thermal mismatch with Silicon • Large permittivity
HgCdTe	• Tailorable bandgap • Well developed theory • Multicolor detectors possible	• Nonuniformity over large areas • High cost in growth and processing • Unstable surface
InGaAs, InSb, InAsSb	• Good material and dopant • Mature technology •Possible monolithic integration	• Longwave cut-off wavelength limited to 7 µm

Extrinsic Detectors A large band gap material is intentionally doped, and a generation recombination (G-R) center is formed close to the conduction band in extrinsic detectors. This kind of detectors needs very low cooling temperatures compared to the intrinsic detectors for the same cut-off wavelength. However, for VLWIR detection applications they are the foremost technology. Si:Ga, Si:As, Ge:Au, Ge:Hg, Ge:Cu and Ge:Zn are the most commonly used extrinsic detectors, and they are responsive between 1-17 µm , 1-23 µm, 1-10 µm, 2-14 µm, 2-30 µm, and 2-40 µm, respectively

Photoemissive Schottky Barrier Detectors The most commonly used Schottky barrier photoemissive detector type is the PtSi which is used for detection in the 3-5 µm window [10]. The cut-off wavelength may be extended to 10 µm by replacing PtSi with IrSi [13]. The incoming radiation passes through the p-type Silicon and is absorbed in the metal (PtSi or IrSi) producing hot holes which are then emitted over the potential barrier into the silicon, leaving the silicide charged negatively. Negative charge of silicide is transferred to a CCD by the direct charge injection method. Even though the quantum efficiency of such detectors is low ($\eta \sim 0.1$), they have the advantage of monolithic integration possibility with Silicon very large scale integrated (VLSI) circuits. In addition to this, Schottky emission is independent from

doping concentration, carrier lifetime and alloy composition which results in an excellent spatial uniformity in this kind of detectors. The uniformity is only determined by the geometric definition of detector pixels. Combining all these advantages with the absence of discernible $1/f$ noise, Schottky-barrier devices are a formidable contender to the main-stream infrared systems and applications [12].

Quantum Well and Superlattice Detectors Intrinsic detectors are the best performing IR detectors. In order to detect IR radiation, especially in the LWIR region, a low bandgap material, such as HgCdTe (MCT), is required. However, these low bandgap materials are known to be difficult to grow, process and fabricate as a device. All these difficulties motivated the study of forming low artificial bandgaps in high bandgap materials. Levine et al, proposed the first Quantum Well Infrared Photodetector (QWIP) for infrared detection based on the GaAs/AlGaAs material system in 1987 [14].

A QWIP is formed by combining a large band gap material with a smaller band gap material, thus forming quantum wells. QWIPs operate on the basis of intersubband transition. This intersubband transition takes place in the quantum wells between two localized energy states which is schematically shown in Fig. 1.4. The photon with the energy corresponding to the difference of E_2 and E_1 is absorbed, and the excited electron contributes to the photocurrent.
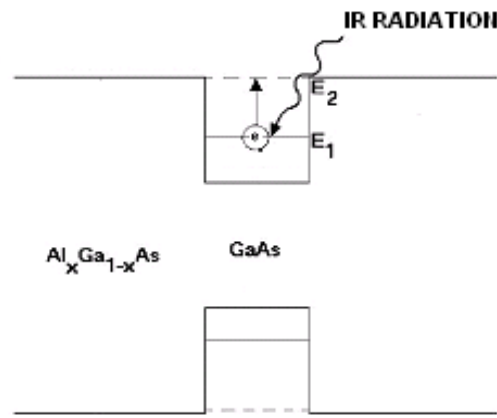
Figure 1.4 Schematic view of intersubband transition between the energy levels E_1 and E_2

The detection wavelength of QWIP is determined by the difference between the two energy levels. These energy levels can easily be tailored by changing the quantum well width or the barrier height. On the other hand, mature material and processing technology of III-V compounds allows developing of large format, highly uniform staring arrays. Combining all these advantages with the possibility of monolithic integration with peripheral electronics, QWIPs have emerged as potential alternatives to conventional infrared detectors utilizing low bandgap semiconductors. More detailed information about the QWIPs and comparison of QWIPs with other detector technologies will be presented in the following chapter.

Recently, InAs/Ga(In)Sb material system based Type-II Strained Layer Superlattice (SLS) detectors emerged as an alternative to the conventional MCT and QWIP detector technology. Type-II SLS detectors have a staggered band alignment such that the conduction band of the InAs layer is lower than the valence band of the Ga(In)Sb layer, thus forming a virtual bandgap. The schematic illustration of the Type-II SLS band structure is given in Fig. 1.5.
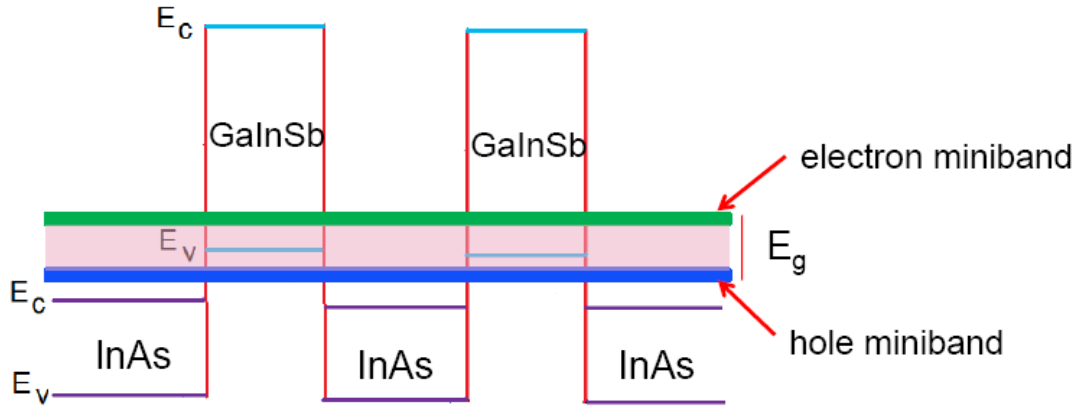
Figure 1.5 Schematic illustration of the Type-II SLS band structure [3]

As shown in Fig. 1.5, heavy holes are largely confined in the GaInSb layers, while electron wave functions overlap considerably from one InAs layer to adjacent InAs layers by the help of very thin barriers. The overlap of the electron wave functions results in the formation of an electron miniband in the conduction band. Spatially indirect transition between the localized heavy holes and the electron miniband determines the infrared detection capability of Type-II SLS structures [15].

Quantum Dot Infrared Photodetectors Quantum dot infrared photodetectors (QDIPs) operate on the basis of intersubband transition like QWIPs. Generically, QDIPs are very similar to QWIPs replacing quantum wells with quantum dots. A simple QDIP structure is shown in Fig. 1.6.
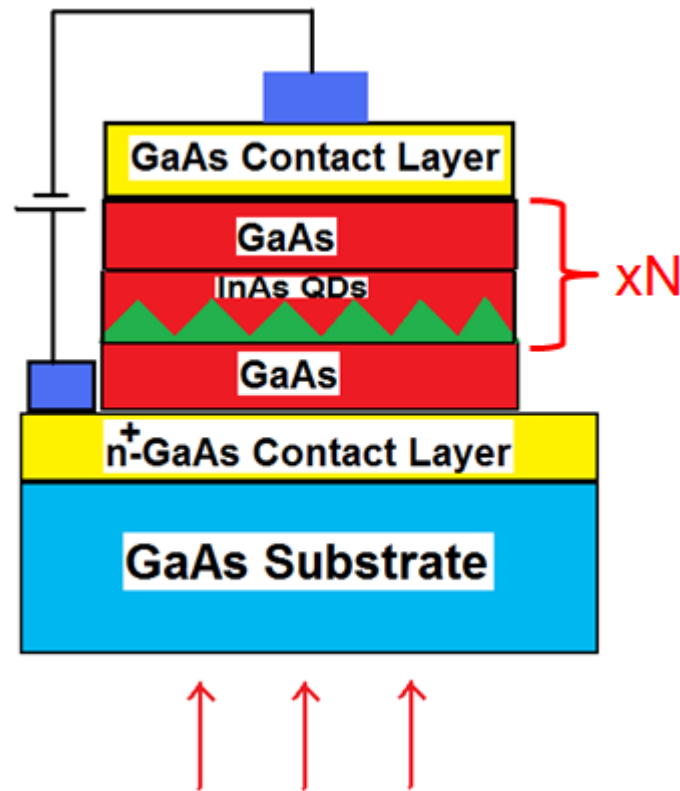
Figure 1.6 A simple QDIP structure [3]

The potential advantages of QDIPs over QWIPs can be summarized as below.

- QDIPs are supposed to detect normal incidence radiation which eliminates the fabrication of grating coupler.
- Thermionic emission is suppressed as a result of confinement in all three dimensions. As a result, electron relaxation time increases due to phonon bottleneck. Thus, signal to noise ratio of QDIPs is expected to be higher than that of QWIPs.
- Dark current of QDIPs are lower than both HgCdTe and QWIP detectors in theory.

As a result of all these advantages, QDIPs have superior characteristics compared to HgCdTe detectors in theory. Theoretically, QDIPs and Type-II SLS detectors are the only detectors that can compete with HgCdTe photodetectors in terms of detector performance. However, the measured 77 K detectivities of QDIPs are inferior to current QWIP and HgCdTe detector performances [16]. The main reason behind this is the difficulties faced with the growth of the QDIP structures. It is almost impossible to control the dot size and the dot shape with the current epitaxial growth techniques. Improving the growth, doping and fabrication conditions may yield QDIPs with better detector performance [17].

1.4 Figures of Merits for Infrared Detectors

In order to have an idea about the performance of an infrared detector, one must know the signal to noise ratio of the detector for unit illumination. This is the ratio of the detector's responsivity to detector's noise. Beside these parameters, in order to assess the performance of the focal plane array (FPA), the minimum detectable temperature difference must be measured. This section will briefly define the figures of merit for infrared detectors and focal plane arrays which can be listed as responsivity, noise, detectivity and noise equivalent temperature difference.

1.4.1 Responsivity

Responsivity is defined as the rate of the change in detector output signal with incoming infrared radiation. The responsivity of photon detectors can be expressed as [18]:

$$R = \frac{q}{h\nu} \eta g \quad \text{(A/W)} \tag{1.3}$$

where q is the electron charge, h is the Planck's constant, ν is the photon frequency, η is the absorption quantum efficiency and g is the photoconductive gain. Absorption quantum efficiency is the ratio of number of generated free electrons to the number of total photons impinging on the detector. While the photoconductive gain is 1 for

photovoltaic detectors, it is defined as the ratio of the mean free path of the excited electrons to the total active layer thickness for the photoconductive detectors.

1.4.2 Noise

Noise can be defined as undesired signals at the output. There are several noise mechanisms for photodetectors such as 1/f noise, Johnson noise, shot noise, and generation-recombination (G-R) noise.

Pink noise or $1/f$ noise is a signal or process with a frequency spectrum such that the power spectral density is inversely proportional to the frequency [19]. This noise is observed in many different systems; however the origin of this noise is not defined yet. It has been shown that, QWIPs do not have 1/f noise down to 30 mHz which allows QWIP base instruments to operate with high integration times [20].

Johnson noise arises from the agitation of carriers in conductors when the temperature is higher than 0 K and it is defined as

$$i_n^2 = \frac{4kt\Delta f}{R}$$

(1.4)

Johnson noise may arise when there is not any applied bias on the conductor. However, because of the very high differential resistance of QWIPs, the contribution of Johnson noise to the total noise is negligible.

Shot noise arises from the random arrival of photons to the detector and this level is the minimum noise level that a detector can achieve.

Under typical operating conditions, Johnson noise is not dominant and the total noise of the photoconductor detectors is determined by G-R noise. Due to the totally random nature of G-R mechanisms, a fluctuation at the output signal arises. The G-R noise is photo and dark current assisted in QWIPs, and it is defined as

$$i_n^2 = 4q(I_{photo} + I_{dark})g_{noise}\Delta f$$

(1.5)

where q is the elementary charge, Δf is the measurement bandwidth and g_{noise} is the noise gain of the detector. Under moderately large biases g_{noise} is equal to g_{photo} [21].

Even in the absence of radiation falling on the detector, there is an unavoidable current flowing through the detector which is called the dark current. Thus, the total current of the detector is equal to the sum of dark and photo currents of the detector, and both of these currents generate G-R noise. If the photo current of the detector is much higher than the dark current of the detector, the detector's performance is limited with the background radiation. A detector's performance that operates under this circumstance is called as background limited performance (BLIP). For a BLIP detector, the dark current is negligible when compared to the photo current, and the G-R noise current of the detector can be simplified to

$$i_n^2 = 4qI_{photo}g_{noise}\Delta f \tag{1.6}$$

The photo current of a detector can be calculated by the multiplication of its responsivity with the radiation power impinging on the detector. For an imaging system, the power falling on the detector can be expressed as

$$P = A\frac{1}{4f_\#^2 + 1}M_p(\lambda) \tag{1.7}$$

where A is the detector area, $M_p(\lambda)$ is the spectral radiant exitance, and $f_\#$ is the f-number of the lens which is defined as the ratio between its focal length and the lens diameter [18]. Thus, the photocurrent of a BLIP detector can be defined by combining Eq.(1.3) with Eq. (1.7) as

$$I_{photo} = A\frac{1}{4f_\#^2 + 1}M_p(\lambda)\frac{q}{h\nu}\eta g \tag{1.8}$$

1.4.3 Detectivity

The detectivity is defined as the inverse of noise equivalent power (NEP), where NEP is the minimum amount of signal power in order to obtain unity signal-to-noise ratio. However, as the square of the noise current is directly proportional to the detector area and the measurement bandwidth, a sensitivity parameter which is independent from the detector area and measurement bandwidth should be defined, so called specific detectivity D^* expressed as

15

$$D^* = \frac{R\sqrt{A\Delta f}}{i_n} \qquad (1.9)$$

where R is the responsivity, A is the detector area, Δf is the measurement bandwidth, and i_n is the noise current. From this point on, specific detectivity will be shortly called detectivity throughout this thesis. If the detector is operated under BLIP conditions, the detectivity can be expressed as

$$D^* = \frac{\sqrt{(4f_\#^2 + 1)\eta}}{2\sqrt{h\nu M_p(\lambda)}} \ \text{cm}\sqrt{\text{Hz}}/\text{W} \qquad (1.10)$$

by combining Eq. (1.3), (1.6), (1.8), and (1.9). It is clear from Eq. (1.10) that increasing $f_\#$ and η will increase the detectivity (as long as the detector stays BLIP).

1.4.4 Noise Equivalent Temperature Difference (NETD)

Responsivity and detectivity are generally used to define the performance of a single pixel detector. In order to assess the performance of an imaging system, another parameter is defined, NETD. The NETD can be described as the minimum temperature difference in a scene which produces a unity SNR. In other words, NETD is the temperature difference of the scene which produces a power difference equal to NEP of the detector [22]. Therefore NETD can be expressed as [18]

$$NETD = \frac{NEP}{dP_B / dT} \qquad (1.11)$$

where P_B is the background power and the derivative of P_B with respect to T is

$$\frac{dP_B}{dT} = A\frac{1}{4f_\#^2 + 1}\frac{dM(\lambda)}{dT} \qquad (1.12)$$

Taking into account that NEP is the inverse of detectivity ($\frac{\sqrt{A\Delta f}}{D^*}$) and combining Eq. (1.11) and (1.12), the NETD is defined as

$$NETD = \frac{(4f_\#^2 + 1)\sqrt{\Delta f}}{\sqrt{A} \int D^*(\lambda) \frac{dM(\lambda,T)}{dT} d\lambda} \qquad (1.13)$$

The detectivity and the target exitance are the functions of wavelength.

1.5 Objective and Presentation of the Thesis Work

In the last two decades there has been significant progress in the quantum well infrared photodetector (QWIP) technology leading to large format focal plane arrays as lower cost alternatives to HgCdTe sensors especially for long wavelength infrared (LWIR) and dual/multiband detection. While the current concentration on quantum structured infrared photodetectors tends to shift from QWIPs to quantum dot infrared photodetectors (QDIPs) at the research level, QDIPs have not yet displayed their expected potential. Considering the fact that most QWIP work, both at single detector and focal plane array (FPA) level, has been focused on the characteristics of QWIPs grown on GaAs substrates, it seems that there still remains significant room for QWIP research on alternative material systems.

Material system alternatives on InP substrate offer various structures which are promising for both single- and dual/multi-band QWIP FPAs. AlInAs-InGaAs is particularly important by providing a lattice matched alternative to the strained AlGaAs-InGaAs material system for both mid-wavelength infrared (MWIR) single band and stacked multi-band QWIP FPAs. On the other hand, the InP-$In_{0.53}Ga_{0.47}As$ system provides an alternative to the AlGaAs/GaAs for LWIR QWIPs.

The main objectives of this thesis can be summarized as follows:

- Investigate the potentials of the InP/InGaAs and AlInAs/InGaAs material systems for LWIR and MWIR QWIP FPA applications, respectively
- Investigate the potential of the combination of the above material systems for MWIR/LWIR dual band QWIP FPAs for third generation thermal imagers.

This thesis work has yielded very important results for overcoming the bottlenecks of QWIPs through utilization of nonstandard material systems. Exceptionally high quantum and conversion efficiencies achieved with strained LWIR InP/InGaAs

QWIPs, as well as desirable detector characteristics and imaging performance obtained with AlInAs/InGaAs MWIR QWIPs are very encouraging for the future of these detectors which seem to remain as the lowest cost alternative for dual/multi band thermal imagers of the near future.

In the second chapter of the thesis, detailed information on operation principles of QWIPs will be presented along with their comparison with HgCdTe and Type-II SLS photodetectors. This chapter will also include the state of the art single-and dual/multi-band QWIP work reported in the literature.

In chapter three, single band MWIR and LWIR QWIPs on InP substrate realized in this work will be discussed in detail. The molecular beam epitaxy (MBE) growth, fabrication and characterization of single band LWIR InP/InGaAs and MWIR AlInAs/InGaAs QWIPs will be presented along with a comparison of their performance with that of GaAs based standard QWIPs.

Chapter four will be dedicated to MWIR/LWIR dual-band QWIPs. This chapter will cover the growth, fabrication and characterization of InP based three-contact dual-band QWIP FPA, as well as a large format voltage tunable dual-band GaAs based QWIP FPA.

Finally, chapter five will list of the important conclusions of this thesis work as well as a summary of future work.

CHAPTER 2

QUANTUM WELL INFRARED PHOTODETECTORS

In this chapter of the thesis, Quantum Well Infrared Photodetectors (QWIPs) will be investigated in detail. The operation principle and the design parameters that affect the device performance will be presented. Comparison of QWIPs with HgCdTe and Type-II SLS photodetectors will also be covered. The chapter will be concluded with the state-of-the art in QWIP technology.

2.1 Operation Principle of QWIPs

QWIPs are formed by combining large bandgap materials with low band gap ones. This combination results in formation of quantum wells in conduction and valence bands of the heterostructure. QWIPs operate on the basis of intersubband transition in contradiction with intrinsic photodetectors which rely on interband absorption. The photon absorption in a QWIP takes place among the ground state and the first excited state of the quantum well. The schematic view of the intersubband absorption is given in Fig. 2.1.
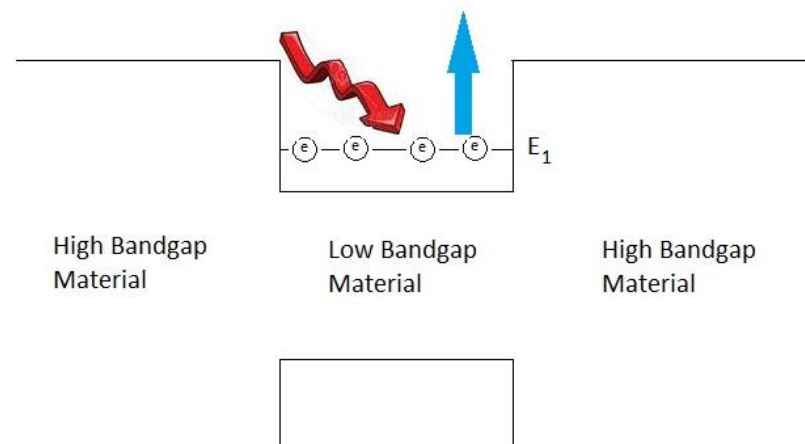
Figure 2.1 Schematic representation of QWIP operation

QWIPs are classified according to the position of the excited state energy level with respect to potential barrier edge. The excited state can lie below the potential barrier edge, at the potential barrier edge or over the potential barrier edge in which case the device type is called bound-to-bound, bound-to-quasi bound or bound-to-continuum, respectively. The schematic representation of the classification of QWIPs is shown in Fig. 2.2.
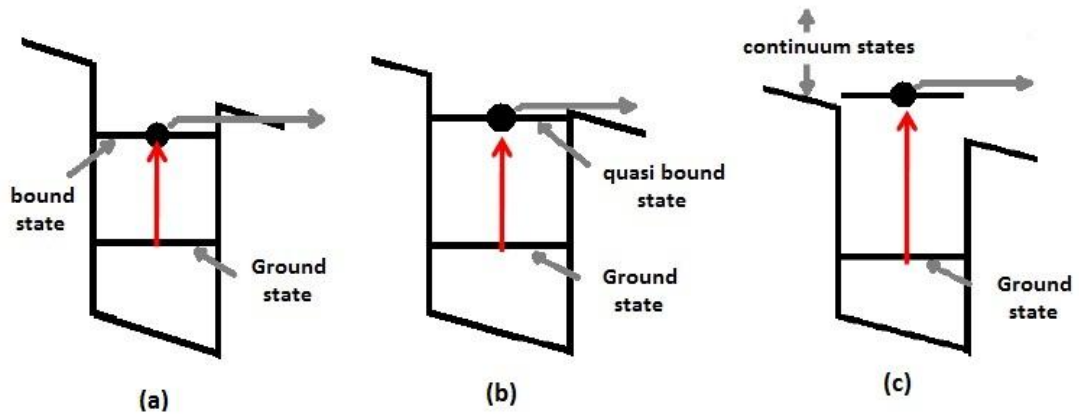
Figure 2.2 Simplified conduction band diagram for (a) Bound-to-bound QWIP (b) Bound-to-quasi bound QWIP, and (c) Bound-to-continuum QWIP

For bound-to-bound QWIPs, the excited electron contributes to photocurrent with the help of tunneling through the potential barrier. The escape probability of excited electrons from the quantum well is very low under low biasing voltages. Thus, this kind of QWIPs need high biasing voltages for lowering the effective potential barrier width which results in higher power consumption when compared to other types. However, this type of QWIP has the highest peak quantum efficiency. This is an outcome of high oscillation strength between the ground and excited state. The oscillation strength can be defined as a dimensionless quantity which expresses the strength of a possible transition of an electron from ground state to the excited state. It is a kind of probability function, and the highest achievable value is 1. High oscillation strength in bound-to-bound QWIP is a result of good confinement of electrons in the ground and excited state, but this confinement ends up with a narrow absorption spectrum.

In order to increase the escape probability, QWIP structure can be designed to have only the ground state lying in the quantum well (bound-to-continuum QWIP). The excited energy state is now in continuum in the form of a miniband, and the probability of re-capturing the electron in the same well is low. Therefore, a lower biasing voltage will be enough to obtain the same photocurrent with the bound-to-bound QWIP structure. However, the dark current of a bound-to-continuum QWIP is larger than that of the bound-to-bound QWIP under the same biasing voltage.

It has been shown that the dark current is dominated by thermionic emission for the detector temperatures higher than 45 K [20]. Thus, locating the excited state just at the quantum well top will end up with high escape probability as well as a sufficiently large energy barrier for thermionic emission (small enough dark current). So far, bound-to-quasi bound type QWIPs have the best performance among all.

The peak detection wavelength of QWIPs is determined by the energy difference between the ground state and the first excited state. This difference can be adjusted to the desired wavelength by changing the quantum well width or the potential barrier height. Schrödinger equation with proper boundary conditions must be solved to obtain these energy levels.

Fermi's Golden Rule defines the total transition rate from the ground state to the first excited state as follows [3]

$$W = \frac{2\pi}{\hbar} \sum_{f,i} |M|^2 F_i (1 - F_f) \delta(E_f - E_i - \hbar w).$$ (2.1)

In Eq.(2.1), F stands for Fermi factor and M is the matrix element which is defined as [3]

$$M = \frac{q}{m^*} \sqrt{\frac{\phi h}{2\varepsilon_0 n_r wc}} [\delta_{k_{x,y}} \delta_{k'_{x,y}}] Sin\theta < \psi_{z,n'} |p_z| \psi_{z,n} >$$ (2.2)

where ϕ is the photon flux, n_r is the refractive index and θ is the angle between the optical beam and the surface normal. Combining Eq. (2.1) and (2.2), and taking the density of two dimensional electrons in the quantum well into account, the quantum efficiency, η, can be expressed as [3]

$$\eta = \frac{q^2 h}{4\varepsilon_0 n_r m^* c} \frac{Sin^2\theta}{Cos\theta} n_{2D} f \delta(E_2 - E_1 - \hbar w) \qquad (2.3)$$

where n_{2D} is the density of two dimensional electrons in the quantum well, and f is the oscillator strength. The angle between the optical beam and the surface normal of the absorbing layer has a great importance in QWIPs. As seen from Eq.(2.3), if this angle is 0 degree, no optical absorption takes place. Thus, a non-zero optical electric field component must exist in the growth direction (normal to the absorbing layer) for absorption of the incoming radiation.

The simplest way to create an optical electric field component normal to the absorbing layer is to use 45° facet structures as shown in Fig.2.3. However, these structures are only feasible for fabricating test detectors, and they cannot be used for imaging arrays.
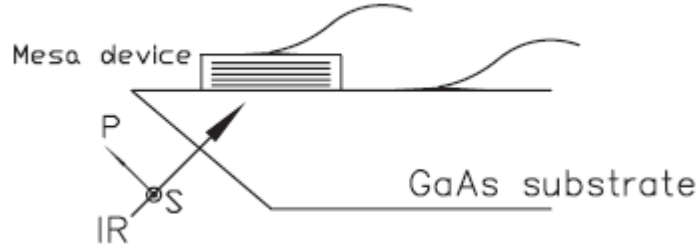
Figure 2.3 45° edge facet light coupling geometry [18]

For focal plane arrays, optical coupling is achieved by either fabricating diffraction grating structures on top of each mesa or by fabricating corrugated mesa structures. Several different monolithic grating structures, such as linear gratings, two-dimensional (2-D) periodic gratings and random-reflectors have demonstrated efficient light coupling to QWIPs, and have made two dimensional QWIP imaging arrays feasible. These gratings deflect the incoming light away from the direction normal to the surface enabling intersubband absorption [20]. A simple diffraction grating structure including the reflector metal is shown in Fig. 2.4.
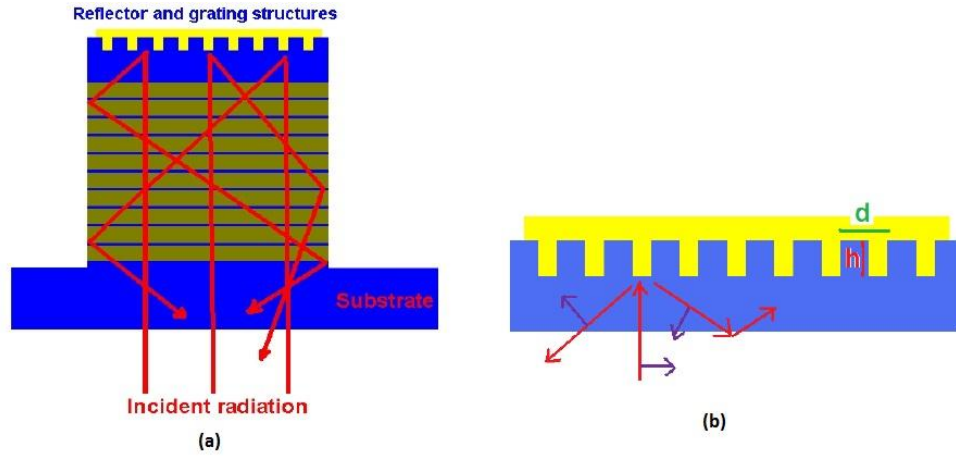
Figure 2.4 (a) Diffraction grating structure and reflector metal on top of it, (b) close look to the grating structure [3] [4]

The period and the depth of the grating coupler play a significant role in tuning the wavelength at which the maximum diffraction occurs. For the optimum coupling, the period and depth are chosen to be half and one quarter of the peak wavelength, respectively [18]. On the other hand, diffraction gratings are tuned for single wavelength, and it is impossible to have optimum coupling for a broad spectrum. Thus, it is not possible to achieve optimum optical coupling for each color in multi-color QWIPs. Beside this, small changes in mesa physical structures and the number of periods of absorbing layer or substrate thickness will result in a change of the quantum efficiency, thus the detector performance.

In order to increase the quantum efficiency, corrugated QWIP (C-QWIP) structures are proposed. The schematic representation of the C-QWIP geometry is shown in Fig. 2.5.
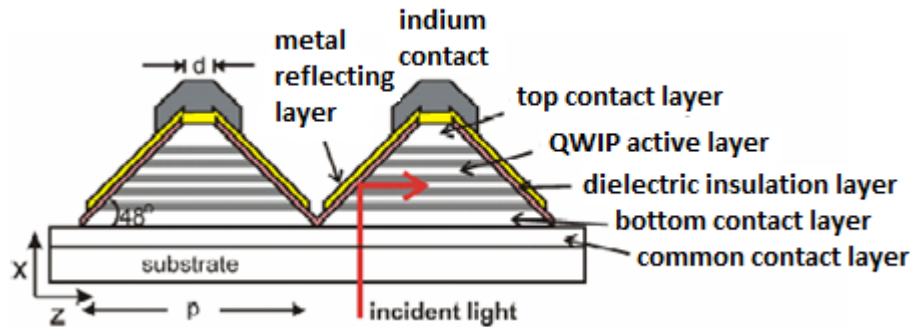
Figure 2.5 Illustration of corrugated QWIP structure [23]

The incoming light passes through the detector staying unabsorbed until it reaches to the reflecting side wall of the mesa structure. As the incoming light impinges on the reflecting sidewall, its propagation is turned normal to the absorbing layer resulting with the absorption of the incoming light. If we assume that the incident light is unpolarized, the maximum achievable quantum efficiency is 50%. As the optical coupling is not tuned for a fixed wavelength, these detectors will reflect the natural absorption spectrum of the detector material. The full width half maximum (FWHM) of the absorption spectrum of C-QWIPs are broader compared to the QWIPs with diffraction grating. Hence, the integrated responsivity of C-QWIPs expected to be larger.

Current responsivity of a QWIP can be expressed as [3]

$$R_i = q\frac{\lambda}{hc}\eta_a p_e g = q\frac{\lambda}{hc}\eta g \qquad (2.4)$$

where η_a is the absorption quantum efficiency and p_e is the escape probability which is defined as

$$p_e = \frac{1}{1 + \dfrac{\tau_e}{\tau_r}} \qquad (2.5)$$

In the above expression, τ_e is the time required for a carrier to escape from the vicinity of the well, and τ_r is the carrier recapture time. The escape probability must approach to unity in order to have high responsivity.

The capture and emission processes in QWIPs are given schematically in Fig. 2.6.
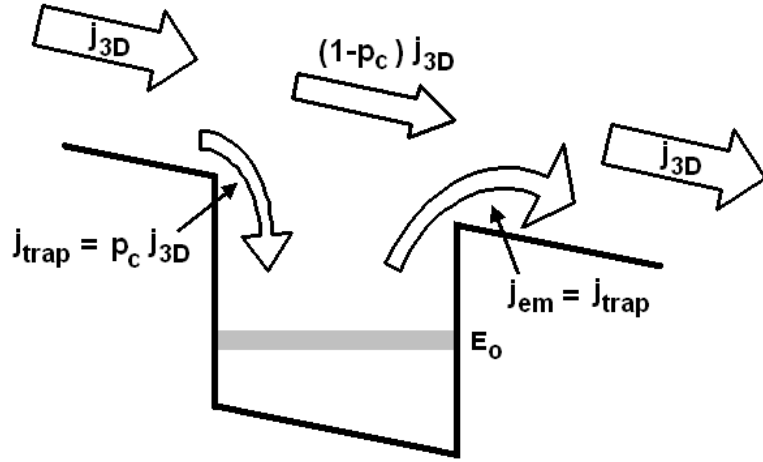
Figure 2.6 Illustration of emission and capture processes in QWIPs [4]

In order to satisfy the current continuity, the current captured by the well must be equal to the current emitted by the same well. Thus,

$$p_c j_{3D} = j_{em}$$ (2.6)

where p_c is the capture probability defined as the probability of an electron to be captured in a well, and j_{3D} is the free electrons in 3-dimensions. If we assume that the total current flowing through the QWIP device is dominated by the photo current, then the emitted current from a single well (j_{em}) and j_{3D} can be expressed as

$$j_{em} = q\phi\eta_{singlewell}$$ (2.7)

$$j_{3D} = q\phi\eta g$$ (2.8)

where ϕ is the total number of photons falling on the detector in one second. Taking the current continuity into account and inserting Eq.(2.7) and (2.8) into Eq. (2.6), the photoconductive gain of the QWIP is found as

$$g = \frac{1}{p_c} \frac{\eta_{singlewell}}{\eta}$$ (2.9)

Since it is a known fact that the quantum efficiency for a single well is low (<<1%), the total quantum efficiency can be expressed as $\eta = \eta_{singlewell} N$. Therefore, the photoconductive gain expression can be simplified to

$$g = \frac{1}{p_c N} \qquad (2.10)$$

The photoconductive gain can also be expressed as [24]

$$g = \frac{\tau_L}{\tau_t} = \frac{\tau_L v_{drift}}{\tau_t v_{drift}} = \frac{L_{drift}}{L_{device}}. \qquad (2.11)$$

The responsivity of the detector is an important parameter in order to sense the incoming radiation with an acceptable signal-to-noise ratio (SNR). However, high responsivity is not the only need for good performance. The detector must also have low dark current originated noise. There are mainly three mechanisms which cause dark current in QWIPs. These mechanisms are illustrated in Fig. 2.7.
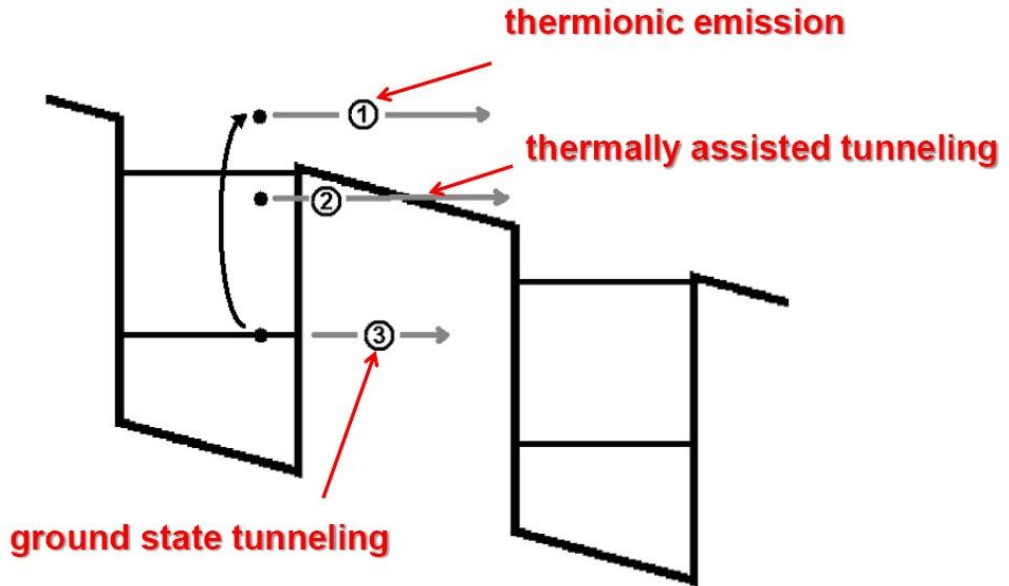
Figure 2.7 Dark current mechanisms for QWIP [3]

The thermionic emission is the dominant dark current mechanisms for QWIPs when the detector temperature is over 45 K [20], and it increases exponentially when the detector temperature increases [24]. In order to suppress the dark current, QWIPs must be operated at cryogenic temperatures. The dark current arising from thermally assisted tunneling is mainly due to the trap levels within the barriers. The density of these traps can be reduced by improving the layer quality in the barriers. Ground

26

state tunneling is weakly temperature dependent, and it is a dominant dark current mechanism below 45 K. Extending the width of barriers (>500 Å) will decrease this component of the dark current in many orders of magnitude [24]. Considering all these factors, the dark current due to thermal generation is expressed as [3]

$$I_{dark}(V) = q \times n_{thermal}(V) \times v_d(V) \times A \qquad (2.12)$$

where $n_{thermal}$ is number of thermally generated carriers, v_d is the drift velocity and A is the detector area.

The dominant noise mechanism for QWIPs is the G-R noise. 1/f noise and Johnson's noise are negligibly small in these devices. If the dark current is dominant (at elevated detector temperature or under no illumination), the total noise current is expressed as

$$i_n^2 = 4qI_{dark}g\Delta f. \qquad (2.13)$$

This noise arises because of the random nature of thermal generation of free carriers. If the detector is exposed to IR illumination, the photocurrent will also create a noise component because of the random arrivals of the photons. In this case, the noise current expression will be

$$i_n^2 = 4q(I_{dark} + I_{photo})g\Delta f. \qquad (2.14)$$

If the detector is operated under dark current limited conditions, the detectivity of the QWIP is found to be

$$D_{dark}^* = \frac{\eta}{2hc/\lambda}\sqrt{\frac{\tau_L}{n_{thermal}NL_p}} \qquad (2.15)$$

by combining Eqs. (1.9),(2.4), (2.11), (2.12), and (2.13).

On the other hand, if the detector is operating at BLIP condition, the detectivity is expressed as

$$D_{BLIP}^* = \frac{\lambda_p}{2hc}\sqrt{\frac{\eta_p}{\phi_b}}. \qquad (2.16)$$

2.2 Material Systems for QWIPs

One of the major advantages of QWIPs over HgCdTe detectors is the realization of infrared detection by using mature III-V semiconductors. The most common material system for QWIPs operating in the LWIR region is $Al_xGa_{1-x}As/GaAs$. The Al mole fraction determines the potential energy barrier, and higher the mole fraction higher the barrier height. However, $Al_xGa_{1-x}As$ ternary compound has an indirect band gap when Al mole fraction exceeds 0.45 in which case higher dark currents are observed. Thus, it is not possible to use this material system for MWIR detection. In order to make efficient detection in MWIR window, the difference between the ground and first excited states must be higher than ~250 meV. In order to achieve this much energy difference (barrier height), $In_xGa_{1-x}As$ is used in the quantum wells instead of GaAs while keeping the Al mole fraction less than 0.4 in the potential barriers. However, this calls for lattice mismatched epitaxy. Lattice constant matching is important for the growth of thin layers of materials on other materials. When the lattice constants differ, strain is introduced into the layer which prevents epitaxial growth of thicker layers without defects. The lattice parameters and energy bandgap data of various III-V compounds are given in Fig.2.8. If the lattice constant of the thin film is larger than the lattice constant of the substrate, the film is tensely strained while the film is compressively strained if the lattice constant of the thin film is lower than the lattice constant of the substrate. When a thin film is epitaxially grown on a substrate, the lattice constant of the thin film adopts to the lattice constant of the substrate through the in plane direction. The lattice distance along the surface normal direction is adjusted such that the thin film keeps its original Poisson's ratio. Thus, the strain introduced to the thin film is a result of the distortion in the lattice constant of the thin film along the surface normal direction.

28
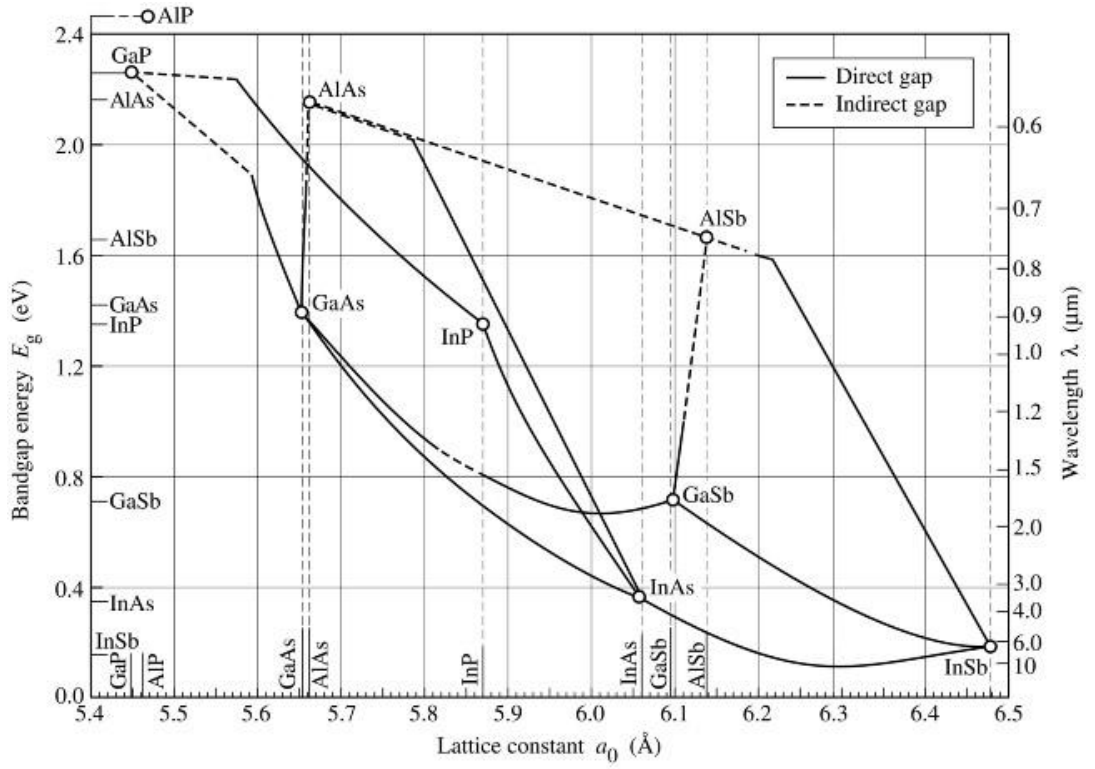
Figure 2.8 Bandgap energy and lattice constants of various III-V compounds at room temperature [25]

Although most of the QWIP work has been focused on GaAs based material systems, there still remains a significant room for QWIP research on alternative material systems. One of the best alternatives to GaAs based QWIPs is the InP based QWIPs. For LWIR detection, InP can act as the potential barrier while $In_{0.53}Ga_{0.47}As$ or InGaAsP can be used for quantum wells. The main disadvantage of using lattice matched ternary $In_{0.53}Ga_{0.47}As$ to form the quantum wells is the short cut-off wavelength around 8.5 μm [26]. This issue can be overcome by replacing $In_{0.53}Ga_{0.47}As$ with InGaAsP as the quantum well material in which case the cut-off wavelength may be extended up to 9 μm [27]. One of the main advantages of using InP based QWIPs for LWIR region is the high photoconductive gain arising from the large energy spacing between Γ and L valleys of InP [28]. On the other hand, $In_{0.52}Al_{0.48}As/In_{0.53}Ga_{0.47}As$ material system which is lattice matched to InP is a good alternative to the strained $In_xGa_{1-x}As/Al_xGa_{1-x}As$ QWIPs for MWIR detection. It has been shown that, MWIR detectors with a cut-off wavelength of ~5 μm can be achieved with excellent imaging performance [29].

2.3 Growth of QWIP Structures

High precision systems are needed to grow QWIP structures as the thicknesses and the compositions of the materials must be controlled accurately. QWIP structures are usually grown with Metal Organic Chemical Vapor Deposition (MOCVD) or Molecular Beam Epitaxy (MBE). In the course of this thesis work, MBE technique is used to grow our QWIP structures. Brief information about this technique will be presented in this section.

MBE was developed in the early 1970s as a means of growing high-purity epitaxial layers of compound semiconductors [30]. Since that time it has evolved into a popular technique for growing III-V compound semiconductors as well as several other materials. MBE can produce high-quality layers with very abrupt interfaces and good control of thickness, doping, and composition. Because of the high degree of control possible with MBE, it is a valuable tool in the development of sophisticated electronic and optoelectronic devices [31]. A typical diagram of MBE chamber and photographs of the METU Epineat III-V MBE reactor are given in Fig.2.9 and Fig.2.10 respectively.
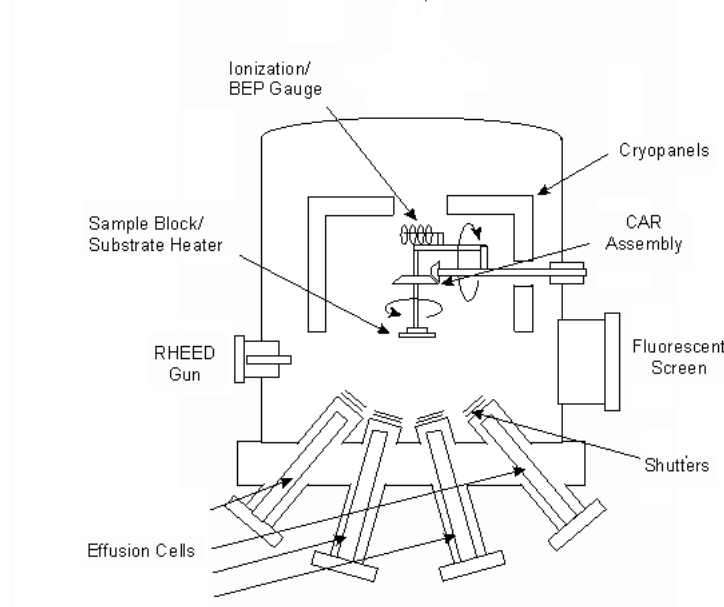
Figure 2.9 Diagram of a typical MBE growth chamber [31]
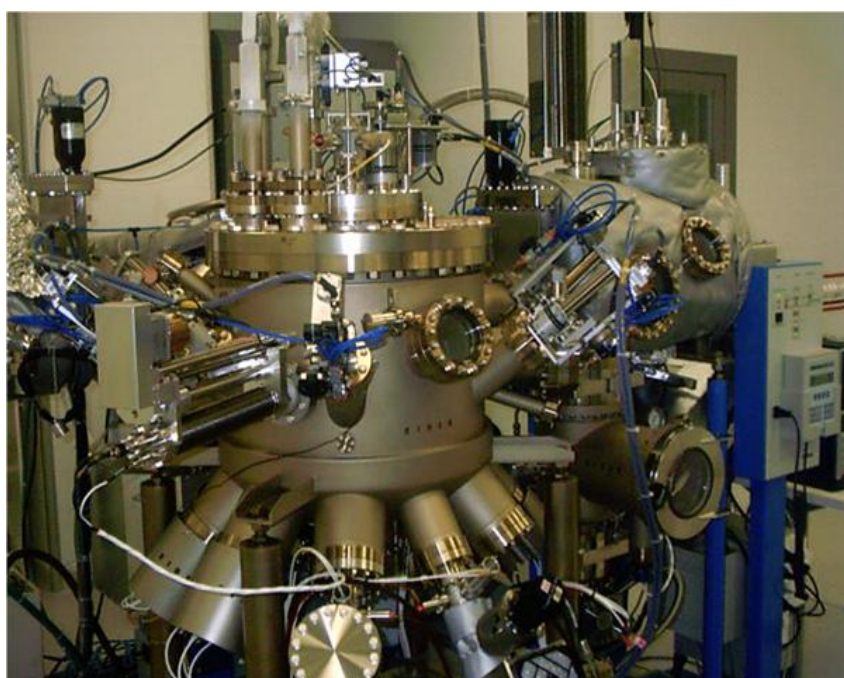
Figure 2.10 Photographs of METU Riber Epineat MBE Reactor

An MBE system is typically constructed with three chambers; loading chamber, buffer and the growth chamber. The loading chamber allows the user to load the substrates without venting the ultra-high vacuum (UHV) environment. The buffer is used for pretreatment of the substrate surface, and the growth chamber is used for growing epilayers.

In the MBE technique, the constituent elements of a semiconductor in the form of 'molecular beams' are deposited onto a heated crystalline substrate to form thin epitaxial layers. The 'molecular beams' are typically from thermally evaporated elemental sources. These high purity sources are loaded into pyrolytic boron nitride (PBN) crucibles which are located in the effusion cells. The reason to choose PBN is the low rate of gas desorption from this material. All the cells have a shutter in front of them to interrupt the fluxes from the cells immediately if needed. To obtain high-purity layers, it is critical that the material sources be extremely pure and that the entire process be done in an UHV environment. UHV environment is obtained by several pumps installed on the system and cryopanels. During the growth of the epilayer, the cryopanels are cooled with liquid nitrogen and acts as an efficient pump. UHV environment allows installing several in-situ characterization tools to the system, where the most important one is Reflection High Energy Electron Diffraction (RHEED) equipment. RHEED is a technique used to characterize the surface of crystalline materials. With the help of RHEED, the phase transitions, the growth rate, and the strain can be monitored during the growth. Beside RHEED, a residual gas analyzer who measures the partial pressures of the molecules inside the chamber and a pyrometer for measuring the substrate temperature are also mounted on the system.

Another important feature is that the growth rates are typically on the order of a few Å/s, and the beams can be shuttered in a fraction of a second allowing atomically abrupt transitions from one material to another [31]. The growth rates of III-V compounds are determined by the group III materials. The sticking coefficient of group V materials is zero over a certain temperature. At typical growth temperatures, group V materials stick to the substrate with the assistance of group III materials.

The growth rates of the group III materials are determined by their fluxes, in other words, with their beam equivalent pressures (BEP) impinging on the substrate. As the BEP of a group III material increase, the growth rate also increases. Before starting the growth, the BEPs of all the group III sources are measured with an ionization gauge which is located just below the substrate and precisely calibrated to the desired value. The calibration is done by either increasing or decreasing the cell temperature. This gauge is retractable so that it does not shadow the BEPs of the sources during the growth. Once the growth rates of all binary compounds are known, the mole fraction of each material in a ternary compound can be calculated easily. For example, for an $Al_xGa_{1-x}As$ ternary compound, the Al mole fraction x is defined by the ratio of AlAs growth rate to the total growth rate which is the sum of the growth rates of AlAs and GaAs.

The doping of the QWIP structures is provided by intentionally incorporating impurities during the growth. Silicon (Si) facilitates n-type doping of the layers. During the growth, Si cell shutter is also opened, and Si is incorporated to the layer.

High quality growth of the QWIP epilayer structure is extremely important in order to obtain a high performance QWIP FPA. Especially, the possible defects in the barrier region will dramatically degrade the performance of the QWIP. The main concerns during the growth can be summarized as below.

- Precise of control of material thickness and composition
- Low unintentional doping concentration
- Low compensation ratio
- High carrier mobility
- High crystal quality
- Perfect surface morphology
- Uniform material composition

All the above goals can be achieved by using high purity materials, keeping the growth chamber as clean as possible and optimizing the growth conditions.

2.4 Fabrication of QWIP FPAs

Once the QWIP structure is epitaxially grown, the wafer is exposed to QWIP FPA fabrication steps. The fabrication starts with forming alignment marks on the sample for single bump FPAs. After the alignment marks are formed, the necessary lithography and dry etching steps are followed to create the grating couplers on the sample. Following this step, mesa structures are etched either by dry or wet etching techniques in order to isolate the pixels from each other. Then, the ohmic contacts are evaporated, and the sample is annealed at high temperatures in order to provide the diffusion of the ohmic contact metals. As the quantum efficiency of QWIPs is low, a thin reflector metal layer is formed on each mesa so that the unabsorbed light is directed back to the absorbing layer. Afterwards, the passivation layer is deposited and the contact points are etched through the passivation layer down to the contact metal. Later, under bump metallization is evaporated in order to provide a stick surface for the indium bumps as well as to form a barrier for In diffusion. Finally, indium bumps are formed through electro plating. Then, the sample is diced and flip-chip bonded to the ROIC. After flip-chipping, an underfill epoxy is injected between the FPA and ROIC to increase the mechanical stability. Because of the large thermal mismatch between the ROIC material and the QWIP material, the FPA must be thinned down to ~ 10 micrometers in order to prevent possible cracking during thermal cycles and to minimize the optical crosstalk between the pixels. As the final step, the FPA is coated with anti-reflection material. The flow diagram of a single bump FPA fabrication is illustrated in Fig. 2.11.
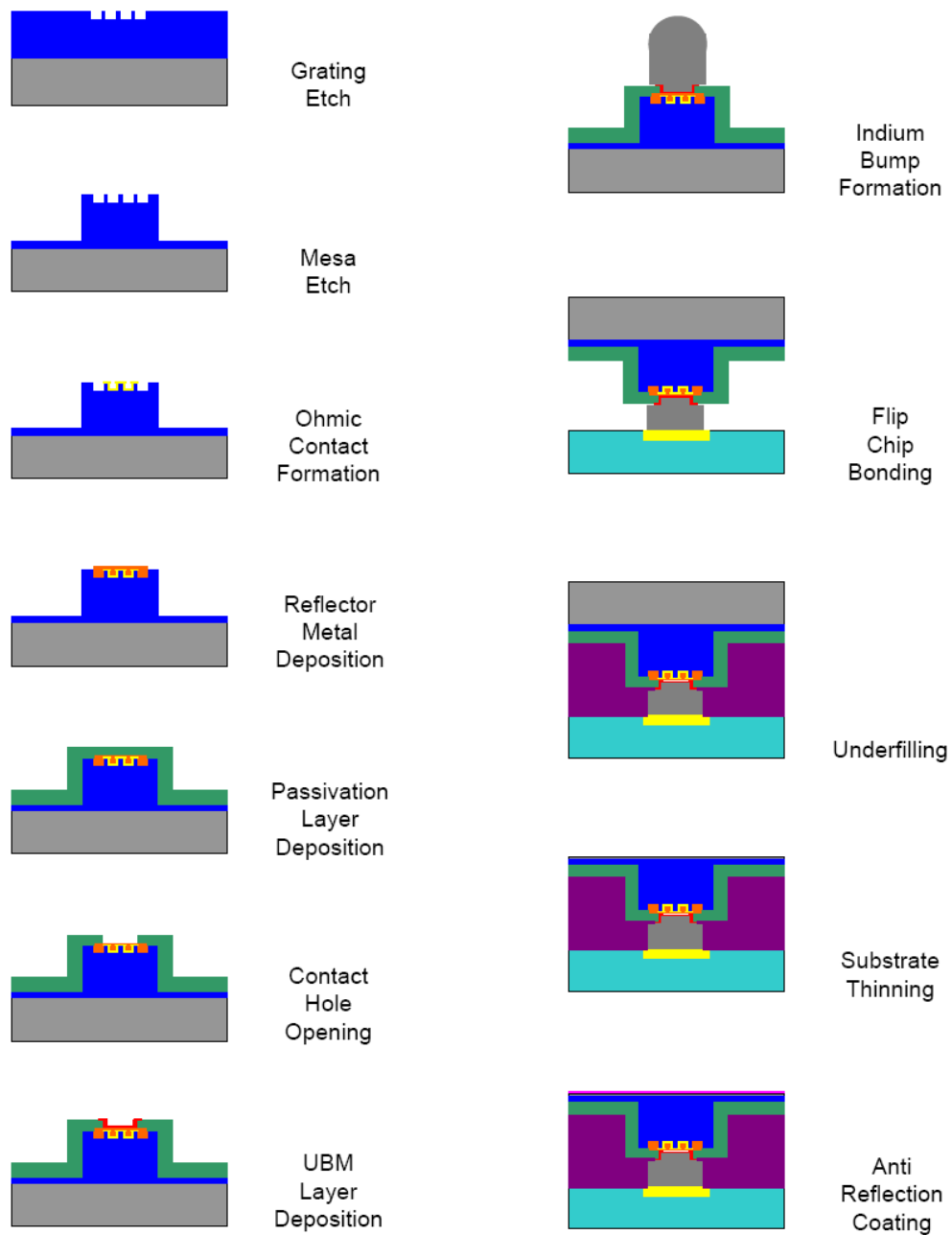
Figure 2.11 Flow diagram of single bump QWIP FPA fabrication steps [32]

2.5 Comparison of QWIPs with HgCdTe and Type-II SLS Photodetectors

$Hg_xCd_{1-x}Te$ is known to be the best material system for infrared detection. Its tailorable band gap allows this material system to cover a large spectrum, starting from SWIR and extending to VLWIR. The band gap of the material is controlled by changing the Hg mole fraction in the ternary compound. The variation of the wavelength with respect to Hg mole fraction at 77 K is given in Fig 2.12.
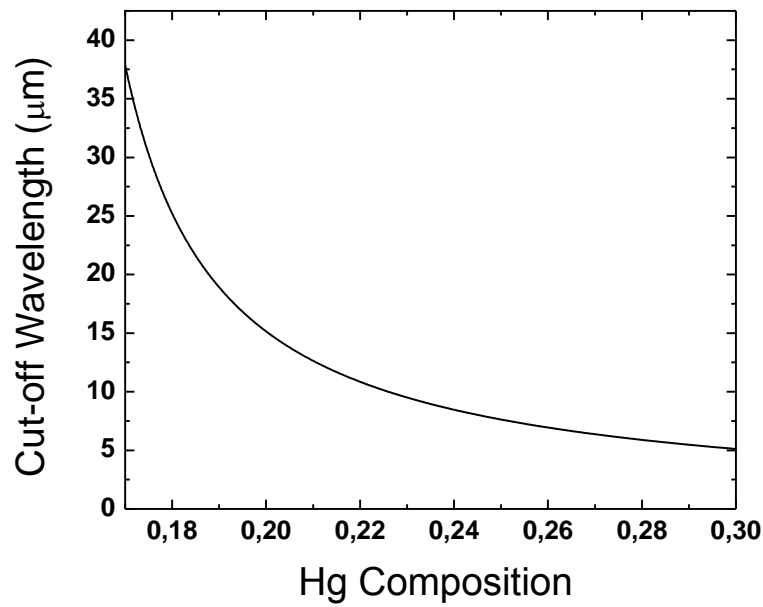
Figure 2.12 Variation of cut-off wavelength of $Hg_xCd_{1-x}Te$ with respect to Hg mole fraction at 77 K detector temperature

As seen from Fig 2.12, the cut-off wavelength of $Hg_xCd_{1-x}Te$ photodetectors is very much dependent on the Hg mole fraction especially in the LWIR and VLWIR region. Hence, a little variation of the Hg composition through the wafer during the growth will introduce a large non-uniformity over the detector array which is usually the case as the growth of this low bandgap material is a real challenging issue. The research work on $Hg_xCd_{1-x}Te$ detector technology has been carried out for 60 years, and it is still not possible to find commercially available large format staring LWIR FPAs. Very large format $Hg_xCd_{1-x}Te$ FPAs are available for SWIR and MWIR detection. However, it is hard for $Hg_xCd_{1-x}Te$ to compete with InGaAs and InSb technology at these bands because of the higher cost of $Hg_xCd_{1-x}Te$ technology. On

the other hand, $Hg_xCd_{1-x}Te$ photodetectors show the best performance when they are grown on $Cd_{0.96}Zn_{0.04}Te$ substrate which is almost lattice matched to $Hg_xCd_{1-x}Te$ for a large range of x value. Nevertheless, the limited substrate size, purity problems, Te precipitations and high cost (50-500 $/cm^2$) are still the problems to be solved. This substrate still seems to be important in the future since the detector performance on alternative substrates (Si, Ge, GaAs) has not emerged the performance limit of lattice matched HgCdTe detectors. Beside the difficulties in the growth of HgCdTe, fabricating this material into FPA is another issue. The brittleness of the material and the limitations during the process decrease the yield and increases the price of the FPA.

Type-II SLS photodetector technology is an emerging technology, and it is the only detector technology which has theoretically a better performance than the HgCdTe photodetectors. It combines the advantages of mature III-V technology with the high quantum efficiency which is biggest bottleneck of QWIPs. Type-II SLS photodetectors are expected to have high uniformity, low tunneling dark current as a result of higher effective mass and low Auger recombination rate as the heavy and light holes are separated. Thus, for the same cut-off wavelength, it is theoretically predicted that a type-II SLS photodetector will display the performance of an HgCdTe detector at a 30 K higher operating temperature [33]. However, this technology is in a very early stage of development and has some problems. The growth of good quality layers is a tradeoff between smooth interfaces which is obtained at high growth temperatures and low residual background carrier concentration (achieved at lower end of the growth window) [2]. Even though, the SLS FPAs operating in the MWIR region are commercially available, the problems with LWIR FPAs still persist. The main problem for LWIR FPAs is the passivation of the mesa structures. The high lattice mismatches between the detector materials and the passivation layers cause a band bending at the interface creating a high leakage current. Several types of dielectric layers are deposited such as silicon nitride, silicon oxide, ammonium sulfide, and aluminum gallium antimonide alloys [2]. However, it was not possible to reach the theoretical predictions.

Encouraging results in Type SLS photodetector technology are obtained by replacing the standard superlattice with an M structure. The quantum efficiency of a LWIR detector with 10.5 μm cut-off wavelength was reported to be 60% where the detectivity value of $2x10^{11}$ Jones was measured [34]. The band diagram of an M-structure along with a standard structure Type-II SLS are given in Fig. 2.13.
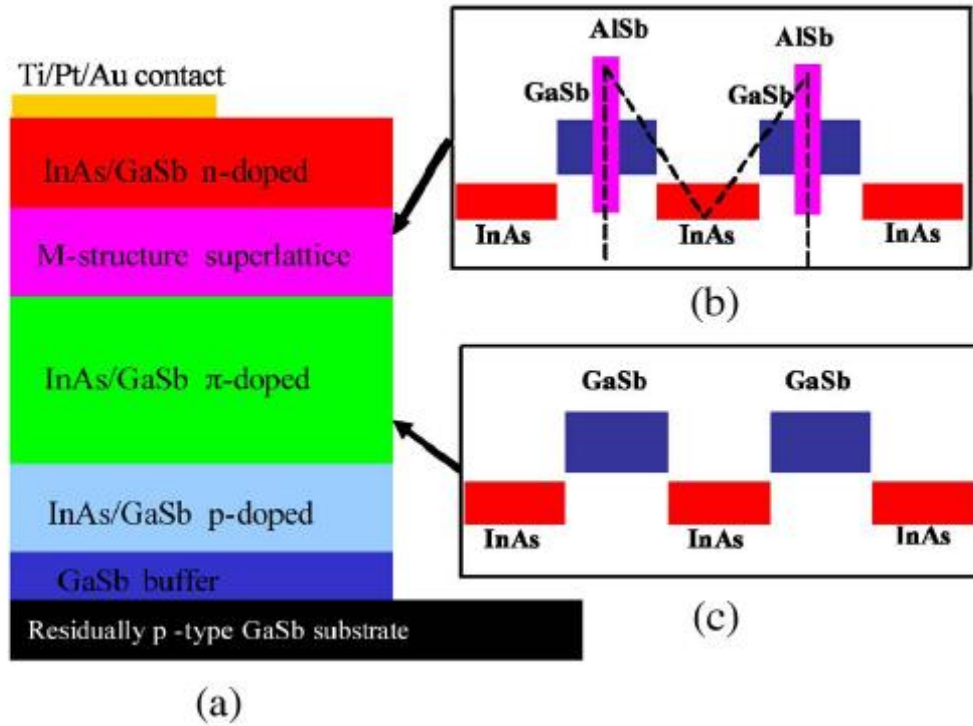
Figure 2.13 (a) Schematic diagram of a p-π-M-n superlattice photodiode design, (b) the band alignments of the M-superlattice structure; the dashed line shows the M-shape of the band alignment, and (c) band alignment of standard Type II superlattice [34].

Even though, the performance of the LWIR SLS FPAs has not been proven completely, these detectors are still presumed to be the best candidate in the VLWIR region due to the nonuniformity of HgCdTe detectors and the very low operating temperature of QWIPs in this wavelength range.

QWIPs cover a wide spectrum with proper bandgap engineering. They also offer excellent uniformity and the advantages of III-V materials. At the same time, the residual non-uniformity of QWIP FPAs is the lowest among all detector types. The mature growth and processing technologies of III-V materials end up with high yield

which dramatically decreases the cost of the FPA. The main disadvantage of the QWIP technology is the low quantum and conversion efficiency (ηg product). However, this bottleneck can be overcome by investigating new material systems. A conversion efficiency as high as 20% was achieved with a strained $InP/In_{0.48}Ga_{0.52}As$ QWIP structure along with a high detectivity in this work [35]. Considering the fact that the photoconductive gain saturates around 0.3 in conventional AlGaAs/GaAs QWIPs [36], and the highest quantum efficiency is 40% [33], the maximum achievable conversion efficiency is 12% in AlGaAs/GaAs QWIPs. Actually, this value is hypothetical and the real conversion efficiency of conventional AlGaAs/GaAs QWIPs is lower than this value. Therefore, the dramatic increase in the conversion efficiency by just switching to a new material system is an encouraging result, and the performance of QWIP may be further improved by improving the design parameters.

2.6 QWIP Design Considerations for Optimum Performance

The design of a QWIP structure depends on several factors. The desired peak and cut-off wavelengths, the desired sensitivity, environmental conditions, and the desired operating temperature are the main factors affecting the design parameters. As stated in section 2.1, QWIPs show the best performance when the excited energy state is located just at the barrier edge (bound-to-quasi bound case). Thus, the well width and the potential barrier height should be designed carefully such that the QWIP act as a bound-to-quasi bound device. After proper selection of the well width and the potential barrier height, the doping density must be chosen. The doping density directly affects the absorption quantum efficiency and the dark current of the detector. The absorption quantum efficiency increases linearly with the doping density [37], while the dark current increases exponentially [24]. In order to find the maximum BLIP temperature of the detector, the dark current and the photo current of the detector can be equated, and the condition for maximizing the photo current can be determined. The photo current and the dark current can be expressed and equated as

$$\eta_{singlewell}\tau_{scatt}\phi_B = \frac{m^*}{\pi\hbar^2}k_BT_{blip}\exp(\frac{E_f}{k_BT_{blip}} - \frac{hc}{\lambda_c k_BT_{blip}}) \quad (2.17)$$

where $\eta_{singlewell}$ is the quantum efficiency of a single well, τ_{scatt} is the scattering time from subband to continuum, ϕ_B is the integrated background number of photons per unit area, T_{blip} is the BLIP temperature, and λ_c is the cut-off wavelength of the detector. Knowing that the $\eta_{singlewell}$ is proportional to the doping density N_D [37], and the Fermi energy E_f can be expressed as $E_f = \frac{\pi\hbar^2}{m^*}N_D$, Eq. (2.17) can be simplified as

$$\frac{E_f}{k_BT_{blip}}\exp(-\frac{E_f}{k_BT_{blip}}) = Constant \times \exp(-\frac{hc}{\lambda_c k_BT_{blip}}). \quad (2.18)$$

Maximizing the left hand side of Eq. (2.18) will tell that the maximum BLIP temperature is reached when $E_f = k_BT_{blip}$ [37]. On the other hand, the detector limited detectivity is maximized when $E_f = 2k_BT$ condition is reached [18]. Hence, there is a tradeoff between high operating temperature and high detectivity when selecting the doping density. Thus, mainly the system requirements determine the doping density. For a particular application, if sufficient cooling is available, QWIP can be designed to have the maximum detectivity or if higher operating temperature is needed the doping level must be chosen to obtain the highest possible BLIP temperature.

The barrier width also plays an important role for the dark current of QWIP. If the barrier is not chosen wide enough, the contribution of dark current generated by the ground state sequential tunneling can not be neglected any more. In order to minimize the affect of ground state sequential tunneling, barrier widths larger than 300 Å are needed.

As a result, there is not a rule of thumb for designing a QWIP. All the parameters must be chosen properly such that the need for the application is fully satisfied.

2.7 State-of-the-Art in QWIP, HgCdTe and Type-II SLS FPA Technologies

There has been a great progress in the development of infrared cameras in the last 50 years, thanks to the rapid development of infrared FPAs and ROICs. It is now possible to find 1024x1024 QWIP FPAs commercially [38]. As the pixel sizes approaches the diffraction limit in the LWIR mode, it does not seem to be possible to fabricate LWIR FPAs with a resolution higher than 1Kx1K. Gunapala et.al has reported 1Kx1K LWIR and MWIR QWIP FPAs [39]. They have obtained very good results in terms of mean NETD and operability. In the MWIR detector, they have used the standard AlGaAs/InGaAs material system. However, they have used coupled wells with different well widths in order to broaden the responsivity spectrum. They have reported a mean NETD of 17 mK with *f*/2.5 optics, 60 ms integration time and 300 K background at 90 K detector temperature. The operability of the FPA was 99.98% which means that the number of the defected pixels is only around 500. The LWIR array also showed superior performance. They have used the standard AlGaAs/GaAs material system. The NETD value of the FPA was 16 mK with *f*/2.5 optics and 29 ms integration time. The detector temperature was 72 K during the measurements. The operability of the megapixel LWIR FPA was 99.98%, thanks to the high uniformity and high yield of mature GaAs technology.

Beside single color QWIP FPAs, a lot of work has been done on dual-band/color QWIP FPAs. There are different approaches for fabricating two color FPAs. One of them is fabricating three-contact FPAs which has three indium bumps per pixel. This option allows simultaneous detection of the scene in different bands, but the formats are restricted to 320x256 with a 40 μm pixel pitch. There is a megapixel dual-band QWIP FPA with two bumps per pixel and a common bump for mid contact, however this FPA suffers from having large dimensions (3.8 cm x 3.5cm) [40].

The other approach in forming a dual/multi band FPA is the spatially shared FPA technique where the spatially selected pixels are fabricated to detect one wavelength. In spite of the fact that this approach also allows simultaneous detection, the data acquired from the pixels is not registered in this approach. Thus, this technique suffers from low fill factor and low resolution.

Dual/multi-band detection can also be achieved by changing the detection wavelength by changing the applied bias, thus using standard single bump FPA fabrication technique. This technique does not allow exactly simultaneous detection, however large format low cost dual-band FPAs can be fabricated easily with this approach. The illustrations of three approaches are given in Fig. 2.14.
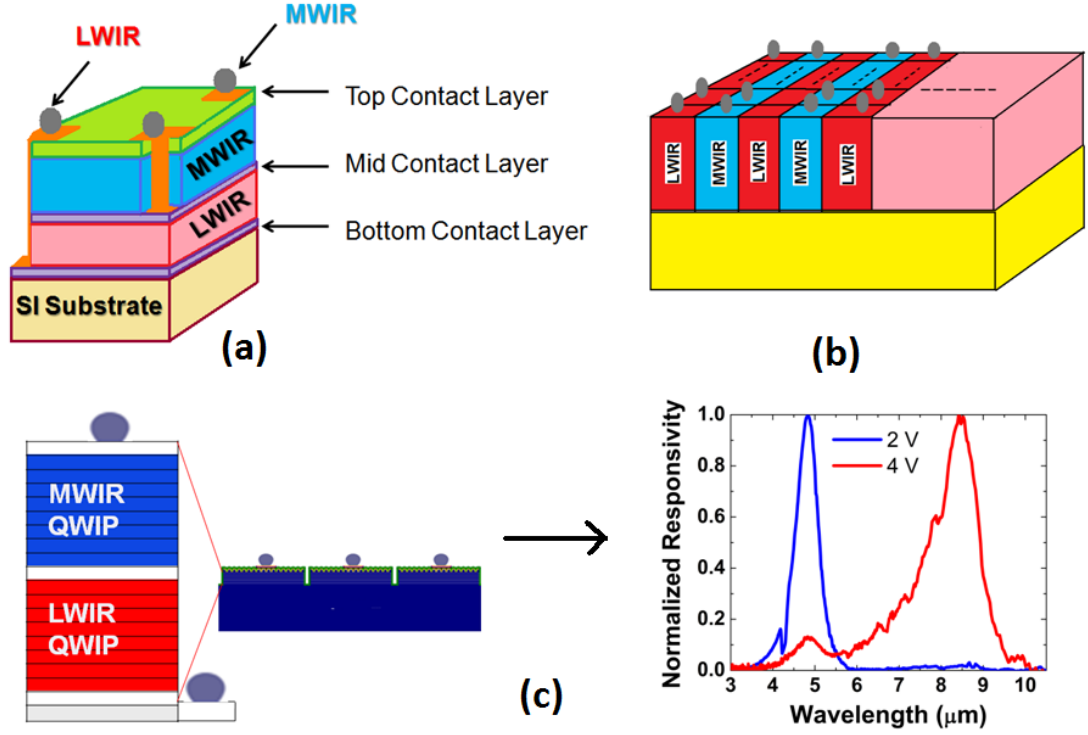
Figure 2.14 Illustration of (a) three-contact, (b) spatially shared, and (c) voltage tunable dual color FPAs.

Most of the work on dual-band FPAs is done for MWIR/LWIR detectors. The first spatially registered simultaneous detection 256x256 QWIP MWIR/LWIR FPA is reported by Goldberg et.al. [41]. Later, Sundaram et.al. reported mid-format (256x256) MWIR/MWIR, MWIR/LWIR and LWIR/LWIR QWIP FPAs with the three-contact approach [42]. The MWIR/LWIR FPA has displayed NETD values better than 35 mK in both bands with *f/*2 optics, 100 Hz frame rate and 65 K detector temperature. The operability of the FPA was around 97%. Later, Schneider et. al. reported a dual-band QWIP FPA with 384x288 format [43]. This detector was made up of a photoconductive MWIR part and a photovoltaic LWIR part and had NETD

values of 17 mK and 43 mK with 7.6 ms integration time and *f/*2 optics in the MWIR and LWIR bands, respectively.

Recently, Gunapala et.al. have fabricated a mega pixel dual-band QWIP FPA [44]. Their FPA was able to detect the radiation from each band simultaneously. However, their design differs from the conventional three-contact approach. They placed two indium bumps per pixel, and the top detector's common was shorted to the bottom detector's common via a metal line. The schematic representation of this new approach together with the conventional one is given in Fig. 2.15.
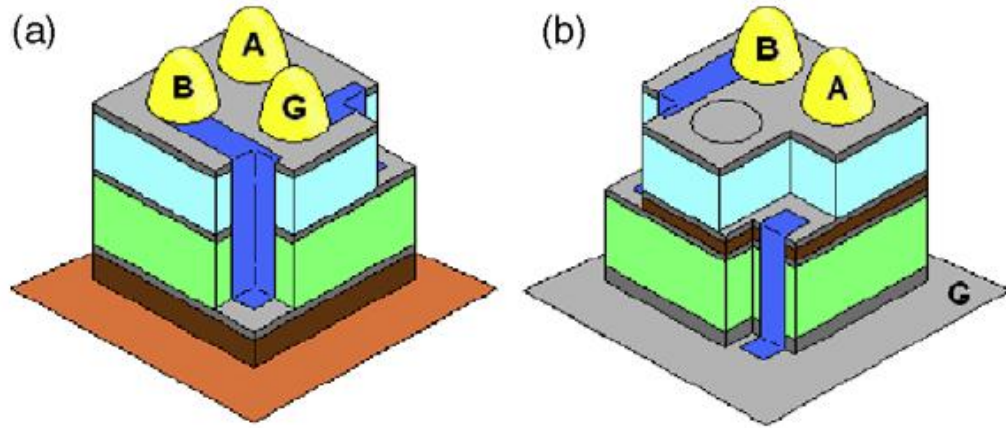
Figure 2.15 Illustration of (a) conventional three bumps (b) two bumps mesa structure [44]

The MWIR part was made of coupled InGaAs/AlGaAs material system where the LWIR part was constructed with the AlGaAs/GaAs material system. The MWIR part is responsive between 4.4-5.1 μm where the LWIR part's spectral response covers 7.8 to 8.8 μm. At 90 K FPA temperature, MWIR stack is under BLIP condition with *f/*2.5 optics up to -1 V bias and exhibits a peak detectivity of 4×10^{11} cmHz$^{1/2}$/Watt. LWIR stack is BLIP at 72 K temperature with -1 V bias and *f/*2.5 aperture. Peak detectivity for LWIR stack is 1×10^{11} cmHz$^{1/2}$/Watt at 70 K FPA temperature. The reported NETD values were 27 and 40 mK at 70 K FPA temperature with *f/*2 optics for MWIR and LWIR bands, respectively. Because of the high complexity of the fabrication process, the operability of the FPA was 90%.

Beside the three-contact dual color FPA approach, there are also reports on spatially shared FPAs. Bandara et.al. reported a 4-color FPA, where each color is made up of 640x128 pixels [45]. The illustration of the structure is given in Fig. 2.16.
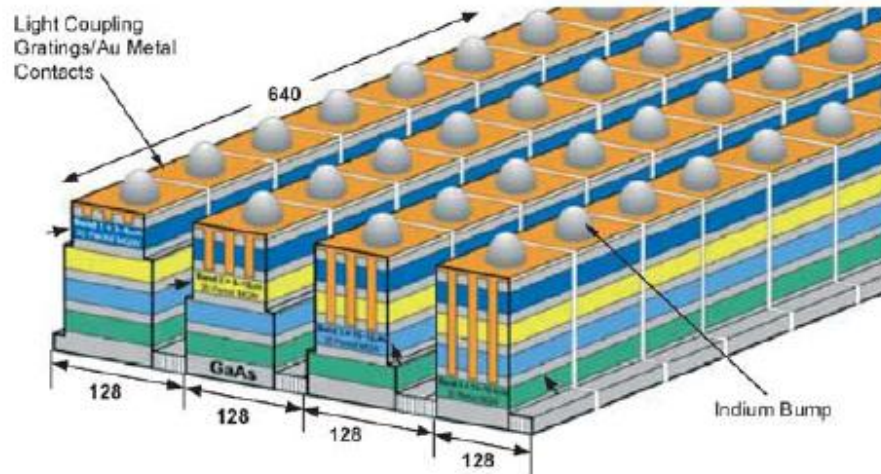
Figure 2.16 Illustration of spatially shared four-band QWIP [45]

In this FPA, each column is responsive to different wavelengths which are 4–5.5, 8.5–10, 10–12, and 13–15.5 μm. This is achieved by growing proper structures on top of each other and separating them with heavily doped n^+ contact layers. For a serial connection of different detectors, the applied bias mostly drops on the stack with the shortest detection wavelength. Depending on this rule of thumb, they have activated the QWIP stacks with longer wavelengths by short circuiting the QWIP stacks with shorter wavelength by a metal line. However, the final operating temperature of the FPA is determined by the longest wavelength. Thus, this FPA has been operated at 45 K as the QWIPs working in the VLWIR region needs to be cooled down to very low temperatures. They have reported NETD values of 21.4, 45.2, 13.5 and 44.6 mK for 4–5.5, 8.5–10, 10–12, and 13–15.5 μm spectral bands, respectively at 40 K FPA temperature.

Up to now, very limited work has been done on voltage tunable dual-band Quantum Structured Infrared Photodetector (QSIP) FPAs. Varley et.al., reported a DWELL

QDIP [46]. The NETD of the FPA was reported as 55 mK and 70 mK in the MWIR and LWIR modes, respectively.

Choi et.al. realized a voltage tunable 256x256 C-QWIP FPA. They have switched the polarity of the applied bias in order to switch from MWIR to the LWIR band. The FPA was operated at 50 K, and the NETD values were 27 mK in the MWIR mode with 98.4% operability and 90 mK in the LWIR mode with 95.9% operability.

Dual-band HgCdTe FPAs have also been reported. Raytheon Vision Systems developed a 1280x720 MWIR/LWIR HgCdTe FPA [47]. The structure is made of two back-to-back diodes as shown in Fig. 2.17. Two-color detection is achieved by changing the bias polarity. Only one of the diodes is under forward in compliance with the applied bias polarity, and the reverse biased diode acts as the detecting element. By alternating between two predetermined bias values, the stack can be adjusted to detect in the MWIR or LWIR mode. The bias switching can be done on a frame by frame basis or many times in a frame. The junction closer to the substrate is designed such that the shorter wavelength radiation is absorbed in this junction. Thus, this junction is transparent to longer wavelengths, and the long wavelength radiation is absorbed in the upper junction. Detector arrays are formed by etching mesa structures down to the bottom n layer. As a result, only a single indium bump per pixel is required for ROIC interconnection. The 1280x780 array showed excellent properties. The cut-off wavelength for the LWIR part is greater than 10.5 µm at 78 K. The LWIR part has achieved an NETD value less than 30 mK, and the operability was greater than 98% with *f*/3.5 aperture. The operability of the MWIR part was 99.9% , and it displayed an NETD below 20 mK with *f*/3.5 aperture.
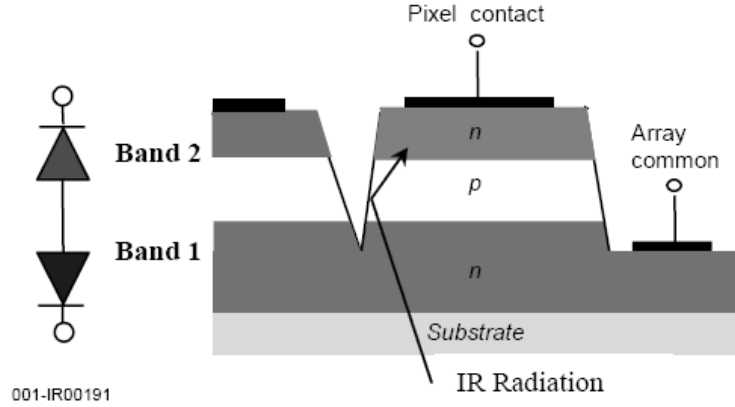
Figure 2.17: Structure of a back-to-back diode. The lower junction is designed to absorb in the MWIR band where the higher junction operates in the LWIR band. [47]

As the Type-II SLS detector technology is not mature enough in the LWIR band, the only dual-band operation with this technology is reported for MWIR/MWIR detection. Rehm et. al. have investigated MWIR/MWIR Type II superlattice detectors fabricated with the three bump approach [48]. The 384×288 FPA had two colors with cutoff wavelengths of 4 μm and 5 μm. The NETD values measured in these bands were 29.5 mK and 16.5 mK, respectively with 73 K detector temperature, $f/2$ optics and 2.8 ms integration time. The operability values were reported as 98% and 99% for the channels having 4 μm and 5 μm cutoff wavelengths, respectively.

The fundamentals and design considerations of QWIPs have been presented in this chapter along with QWIP state of the art and comparison with the competing infrared photodetector technologies. The next chapter will present the work done in this thesis on InP based MWIR and LWIR QWIPs with the main objective of overcoming the low conversion efficiency bottleneck of the standard GaAs based QWIP technology.

CHAPTER 3

MWIR AND LWIR QWIPs ON InP SUBSTRATE

Material system alternatives on InP substrate offer various structures which are promising for both single- and dual/multi-band QWIP FPAs. AlInAs-InGaAs is particularly important by providing a lattice matched alternative to the strained AlGaAs-InGaAs material system for both mid-wavelength infrared (MWIR) single band and stacked multi-band QWIP FPAs. On the other hand, the InP/In$_{0.53}$Ga$_{0.47}$As system provides an alternative to AlGaAs/GaAs for LWIR QWIPs in case high external quantum efficiency is needed [26]. The semiconductor material systems based on mature technologies are listed in Table 3.1 for QWIP applications in the MWIR and LWIR windows.

Table 3.1 Comparison of basic parameters of different mature semiconductor material systems used for QWIP applications [3]
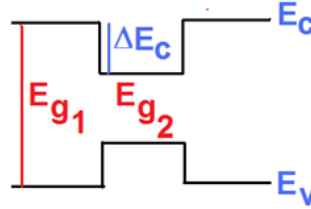
Material System	Eg1 (eV)	Eg2 (eV)	ΔEc (eV)	Comments
Al$_x$Ga$_{1-x}$As/GaAs	Variable	1.43	Variable	Used for LWIR QWIPs ΔEc insufficient for MWIR QWIPs with acceptable x
Al$_x$Ga$_{1-x}$As/In$_y$Ga$_{1-y}$As	Variable	Variable	Variable	Used for MWIR QWIPs
InP/In$_{0.53}$Ga$_{0.47}$As	1.35	0.75	0.25	Used for LWIR QWIPs High R$_i$, λ$_c$ seems to be adjustable with strain
Al$_{0.52}$In$_{0.48}$As/In$_{0.53}$Ga$_{0.47}$As	1.45	0.75	0.5	Used for MWIR QWIPs

3.1 Advantages of InP Based QWIPs

The biggest bottleneck of QWIPs is the low quantum efficiency and low gain. Although, the imaging performance of the QWIP FPA is excellent if the integration time is kept long enough, standard QWIP performance is questionable for high frame rates or low background targets. In order to achieve satisfactory imaging capability with low integration times and/or backgrounds, the absorption quantum efficiency and the gain of the detector must be high enough. The absorption quantum efficiency and gain of a standard AlGaAs/GaAs LWIR QWIP FPA is typically 5% and 0.5, respectively. This results in an insufficient conversion efficiency (η.g product) under high frame rates (low integration times) and/or low background conditions. Under such conditions, the signal to noise level of the FPA/ROIC hybrid becomes limited by the ROIC noise which may considerably exceed the detector noise level.

The absorption quantum efficiency is directly proportional to the density of two dimensional electrons in the quantum well (n_{2D}) and the oscillator strength (f) as shown in Eq.(2.3) where n_{2D} and f are defined as

$$n_{2D} = \frac{m^* kT}{\pi \hbar^2}(1 + e^{\frac{E_F}{kT}}) \qquad (3.1)$$

and

$$f \equiv \frac{2m^*\omega}{\hbar}\langle z \rangle^2 = \frac{2m^*\omega}{\hbar}\left(\frac{16}{9\pi^2}\right)L_w^2 \qquad (3.2)$$

respectively. For infinitely large barriers, the solution of Schrödinger's equation gives that the energy difference between the ground state and the first excited state can be expressed as

$$E_2 - E_1 = \frac{3\hbar^2\pi^2}{2m^* L_w^2}. \qquad (3.3)$$

Extracting L_w form Eq.(3.3) and inserting it into Eq.(3.2) shows that the oscillator strength (f) is independent of m^* for fixed $E_2 - E_1$. This makes the quantum efficiency inversely proportional to the effective mass. As a result, smaller m^* is

expected to yield higher absorption quantum efficiency for a given n_{2D}. The effective mass of the electrons in the Γ valley of GaAs is $0.067m_0$ [49], while it is $0.041m_0$ in $In_{0.53}Ga_{0.47}As$ [50]. Thus, the quantum efficiency of an InP/ $In_{0.53}Ga_{0.47}As$ LWIR QWIP is expected to be 1.63 times higher than that of an AlGaAs/GaAs QWIP for the same quantum well 2-D doping density. However, it should be noted that the Fermi level in InP/ $In_{0.53}Ga_{0.47}As$ QWIP will be at a higher energy due to smaller effective mass as shown in Eq. (3.1). This results in a higher dark current in InP/ $In_{0.53}Ga_{0.47}As$ QWIP.

Let's consider an AlGaAs/GaAs and an InP/ $In_{0.53}Ga_{0.47}As$ QWIP with 50 Å thick quantum wells and the same optical activation energy, $E_b - E_1$, (Fig. 3.1). The doping level in both QWIPs is assumed to be 4×10^{17} cm^{-3} ($n_{2D} = 2 \times 10^{11}$ cm^{-2}) which is in the order of the optimum doping level for highest detectivity in AlGaAs/GaAs QWIPs. We also assume that all the other parameters (such as device gain) are similar in the two QWIPs.

At the given quantum well doping density, the differences between the Fermi level and the ground state (E_1) are expected to be 5.33 and 10.93 meV in AlGaAs/GaAs and InP /$In_{0.53}Ga_{0.47}As$ QWIPs, respectively.
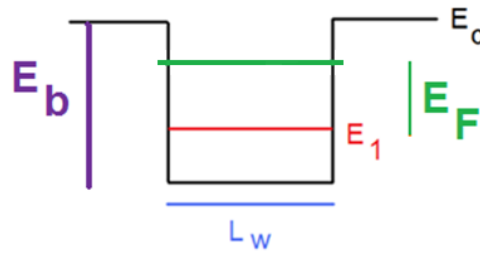
Figure 3.1 Energy band diagram of the quantum well in QWIP. E_F represents the Fermi level, E_1 is the ground state energy and E_b-E_1 is the optical activation energy [3].

As the quantum efficiency of InP based QWIP is 1.63 times higher than the GaAs based QWIP, it can be estimated that

$$I_{P_{InP}} = 1.63 I_{P_{GaAs}} \tag{3.4}$$

where I_p is the pure photocurrent arising from the absorption of impinging photons.

The dependence of the dark current on the temperature can be defined as [24]

$$I_{dark} \propto Tm^{*} e^{-\frac{E_b - E_1 - E_F}{kT}}.$$
(3.5)

By using the relation given in Eq. (3.5) and assuming operation at 65 K, the dark current ratio of InP and GaAs based QWIPs can be calculated as

$$\frac{I_{darkInP}}{I_{darkGaAs}} = \frac{m_{InP}^{*}}{m_{GaAs}^{*}} \frac{e^{\frac{E_{FInP}}{kT}}}{e^{\frac{E_{FGaAs}}{kT}}} = \frac{m_{InP}^{*}}{m_{GaAs}^{*}} \frac{e^{\frac{m_{GaAs}^{*}}{m_{InP}^{*}} \frac{E_{FGaAs}}{kT}}}{e^{\frac{E_{FGaAs}}{kT}}} = \frac{1}{1.63} e^{0.61 \frac{E_{FGaAs}}{kT}} = 1.67.$$
(3.6)

We conclude that

$$\frac{(I_P / I_{dark})_{InP}}{(I_P / I_{dark})_{GaAs}} = \frac{1.63}{1.67} \approx 1.$$
(3.7)

This result is important in the sense that for the same doping level, InP based QWIPs offer almost 60% higher quantum efficiency than the GaAs based QWIPs while keeping the same I_P / I_{dark} ratio at the same operating temperature.

On the other hand, if the same absorption quantum efficiency is targeted in these QWIPs, InP based QWIP can be doped at a density 1.63 times lower than that in GaAs based QWIP (N_d=4x10^{17} cm^{-3}) since the absorption quantum efficiency is directly proportional to the doping level [37]. In this case, the difference between the Fermi level and the ground state will be around 5.12 meV in InP based QWIP while it is still 5.33 meV in GaAs based QWIP. Then the dark current ratio of InP and GaAs based QWIPs can be calculated as

$$\frac{I_{darkInP}}{I_{darkGaAs}} = \frac{m_{InP}^{*}}{m_{GaAs}^{*}} \frac{e^{\frac{E_{FInP}}{kT}}}{e^{\frac{E_{FGaAs}}{kT}}} = \frac{1}{1.63} \frac{2.49}{2.59} = 0.59$$
(3.8)

for 65 K operating temperature. It should be noted that the photocurrents will be at the same level due to the same quantum efficiency. Hence, for the same quantum efficiency, I_P / I_{dark} of InP based QWIP is 1.7 times higher than that of GaAs based QWIP. This results in a roughly 3 K higher BLIP temperature in InP based QWIP if

the targeted peak responsivity wavelength is ~ 9 μm. By decreasing the power consumption of the integrated detector dewar cooler assembly (IDDCA), this much difference in the BLIP temperature is important in terms of cooler lifetime and operating requirements.

In the above analysis, we have assumed that the two QWIPs have similar transport characteristics resulting in comparable device gains. However, the most important advantage of InP based LWIR QWIPs is the higher responsivity as a result of larger gain offered by this material system which arises from the higher drift distance of the photo excited electrons. Larger drift distance in InP based QWIPs can be attributed either to better transport properties of the binary InP or the larger photo excited carrier lifetime. Detailed ensemble Monte Carlo (EMC) simulations were carried out in order to clarify the reason behind the larger gain in InP based QWIPs in the course of another work [28] [51]. Due to the complicated physics of QWIP operation, reliable evaluation of device characteristics requires precise modeling of internal device mechanisms. Both three-dimensional (3D) and two-dimensional (2D) electrons were simulated by taking size quantization into account in the Γ and L valleys of the conduction band [28]. The rates of the simulated 2D$\leftrightarrow$2D, and 2D$\leftrightarrow$3D scattering processes were calculated using the wave function solutions of the Schrödinger's Equation [28]. The drift distance was extracted from the device gain obtained by dividing the number of electrons injected into the device by the total number of the excited electrons that escape from quantum wells. Electron lifetime was calculated by dividing the average drift distance of the excited electrons by the average velocity of these electrons extracted from the simulation [28]. An important difference between GaAs and InP based QWIPs in terms of carrier transport characteristics is the Γ-L energy spacing in the barrier material which is considerably larger in InP. While, the EMC simulations were carried out for standard photoconductive LWIR QWIPs based on the $Al_{0.3}Ga_{0.7}As/GaAs$ material system, they were repeated by artificially increasing barrier material Γ-L energy spacing to a value equivalent to that in InP in order to isolate the effects of this parameter on the device characteristics [51].

An important information extracted from the EMC simulations was the creation of an efficient capture path through the L valley quantum well [28] [51] as the electrons scatter to satellite valleys. Fig. 3.2 and 3.3 show the drift distance, photoexcited carrier lifetime and average electron velocity versus the average E-field in the device with two different Γ-L energy spacings in the barrier material [51].
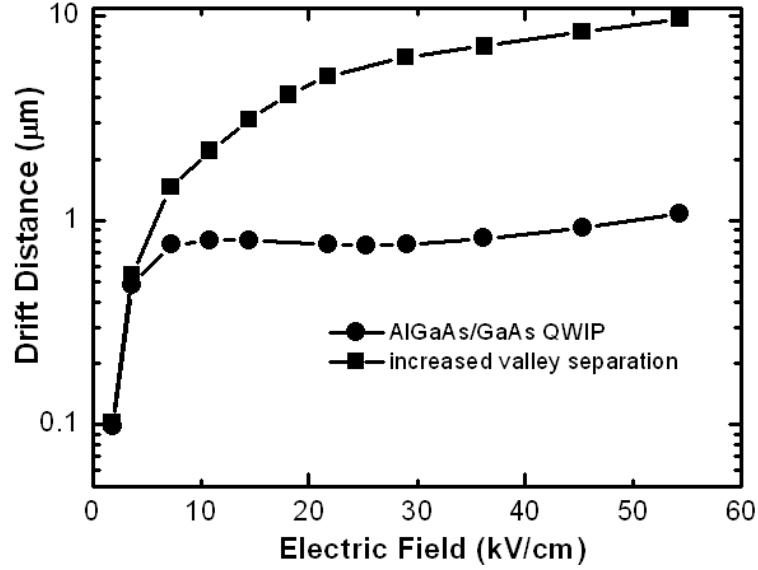
Figure 3.2 Drift distance in $Al_{0.3}Ga_{0.7}As$/GaAs QWIP calculated through ensemble Monte Carlo simulations. The drift distance calculated with increased Γ-L energy separation in the barrier is also shown [51].
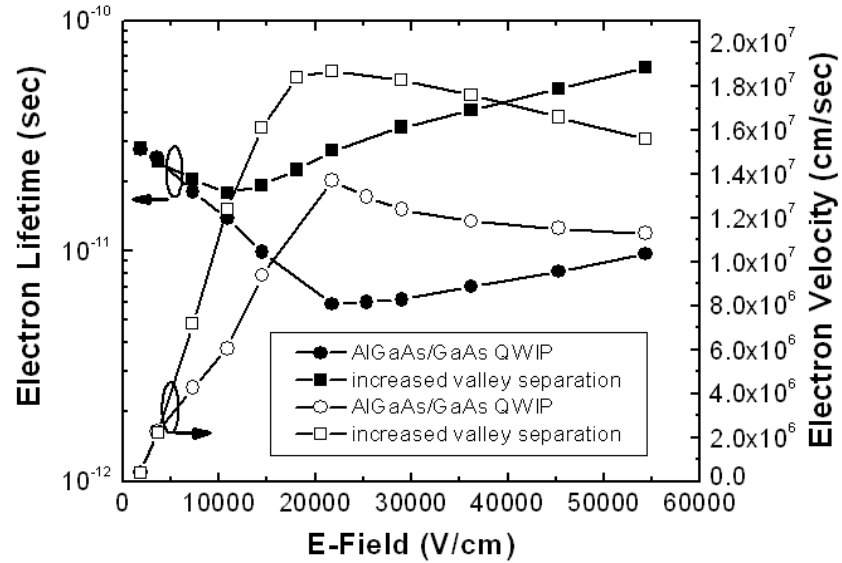
Figure 3.3 Photoexcited electron lifetime and velocity for $Al_{0.3}Ga_{0.7}As$/GaAs QWIP calculated through ensemble Monte Carlo simulations. The lifetime and velocity calculated with increased Γ-L energy separation in the barrier are also shown [51].

52

The dependence of the drift distance on the E-field is in good agreement with the experimental observations on AlGaAs/GaAs and InP/InGaAs QWIPs. As shown in Fig. 3.3, increased energy spacing between the central and satellite valleys (equal to those in InP) results in an improvement in the average electron velocity by a factor of ~1.5, while the excited electron lifetime increases by a factor of ~6 resulting in an improvement in the gain by a factor of ~10 under moderate and large bias voltages [51]. These results suggest that the gain improves with increasing energy spacing between the central and satellite valleys mainly through the increase in the excited electron lifetime [51]. According to the results, relatively high gain observed in InP/In$_{0.53}$Ga$_{0.47}$As QWIPs is not due to the higher mobility in InP as suggested earlier [52]; it can mainly be attributed to higher excited electron lifetime as a result of relatively large Γ-L energy spacing and higher Γ valley occupancy of the continuum electrons with relatively high kinetic energy [51].

It should be noted that the drift distance and gain in AlGaAs/GaAs based QWIPs saturate at a value significantly smaller than that achievable with InP/InGaAs QWIPs. A high conversion gain (η.g product) is desirable in the case of high frame rates and/or low backgrounds. AlGaAs/GaAs QWIPs suffer from read-out noise limited sensitivity under such conditions due to low gain and conversion efficiency. However, InP based QWIPs offer the flexibility of a bias adjustable gain and therefore the possibility of much larger gain values whenever required. This issue will be explained in further detail in Section 3.6.

While LWIR AlGaAs/GaAs QWIPs have extensively been investigated, there has been relatively small amount of work on the characteristics of Al-free InP/InGaAs QWIPs offering higher responsivity. A presumable disadvantage of this material system is the lack of flexibility in adjusting the detection wavelength by changing the barrier/well material composition in the lattice matched structure which yields a cut-off wavelength around 8.5 μm. However, it has been shown by Gusakov et. al. [53] that the operating wavelength can be extended up to 11 μm by incorporating strain as an additional design parameter. It is also possible to increase the cut off wavelength to 9 μm by using InGaAsP instead of InGaAs as the quantum well material [27] [54].

53

The characteristics of LWIR InP/InGaAs QWIPs grown by metal organic molecular beam epitaxy were first discussed by Gunapala *et. al.* [55]. The authors reported peak responsivities significantly exceeding those of AlGaAs/GaAs QWIPs under large bias voltages [55]. Andersson *et. al.* [56] reported similar observations on metal organic vapor phase epitaxy grown InP/InGaAs QWIPs. Large gain and responsivity in InP/InGaAs QWIPs were also reported by other groups [57] [58] [59] [52]. The first InP/InGaAs QWIP FPA with mid format (256x256) was reported by Jiang *et. al.* [52] using metal organic chemical vapor deposition grown material. Our group have recently reported the first large format (640x512) InP/InGaAs and InP/InGaAsP FPAs with desirable thermal imaging performance [26] [27].

While InP/InGaAs on InP material system offers an alternative to standard AlGaAs/GaAs QWIPs for LWIR imaging applications, AlInAs/InGaAs system offers a lattice matched alternative to the strained AlGaAs/InGaAs system for MWIR QWIP applications. The limited conduction band discontinuity of the AlGaAs/GaAs system makes it impossible to grow AlGaAs/GaAs epilayer structures sensitive in the 3-5 μm MWIR window with acceptable Al mole fractions. Providing sufficiently large conduction band discontinuity, AlGaAs/InGaAs material system has been the standard system for MWIR QWIPs, in spite of the degrading effects and limitations of lattice mismatched epitaxy.

There has been very limited amount of work on AlInAs/InGaAs QWIPs. The potential of the AlInAs/InGaAs system for MWIR QWIPs was first investigated by Levine *et al* [60] with 50-well AlInAs-InGaAs structure including 50 Å InGaAs wells and 100 Å thick AlInAs barriers. The structure resulted in a bound to bound QWIP with an absorption peak wavelength of 4.4 μm and $\Delta\lambda/\lambda_p{\sim}7\%$. Hasnain *et al* [61] broadened the absorption linewidth to 93 meV by decreasing the QW width to 30 Å. The maximum peak responsivity of the detectors was 25 mA/W at $\lambda_p{=}4$ μm. Recently, Fathimulla *et al* [62] reported a 320x250 MWIR QWIP FPA on InP substrate with NETD of 90 mK and 88% operability. Recently, the first large format InP based MWIR FPA with 4.6 μm cut-off wavelength was reported by our group [63].

In spite of the above mentioned advantages, there has been very limited amount of work reported on the characteristics of InP based QWIPs, while QWIPs on GaAs substrate have extensively been investigated. It is one of the main objectives of this thesis work to investigate the potential of InP/InGaAs and AlInAs/InGaAs material systems on InP substrate for single and dual-band QWIP FPAs. The remaining part of this chapter is organized as follows. Section 3.2 is devoted to the presentation of the work done on the molecular beam epitaxy growth of single band MWIR AlInAs/InGaAs and LWIR InP/InGaAs QWIP structures which was done through collaboration with Y. Arslan [64] and M. Kaldırım [32]. Section 3.3 is reserved for the fabrication and characterization of large format MWIR AlInAs/InGaAs QWIP FPAs, while Section 3.4 discusses the work done on LWIR InP/InGaAs QWIP FPAs. Finally Section 3.5 presents the conclusions of this work. The dual-band FPA applications of these material systems will be presented in the following chapter. The results are very encouraging for overcoming the bottlenecks of the QWIP technology

3.2 Molecular Beam Epitaxy Growth of QWIP Structures on InP Substrates

In this thesis work, MBE technique was used for growing the QWIP structures. The structures were grown on 3-inch semi-insulating (SI) InP substrate using the 4-inch Riber Epineat MBE system. The substrate is first loaded into the loading chamber of the MBE system and then transferred to the buffer chamber for preparation for the growth. The substrate is degassed at 300 °C for 30 minutes before transferring to the growth chamber. Once the substrate is transferred to the growth chamber, it is heated under Phosphorus (P_2) flux, until the surface oxide is removed while the phase transition of the surface is observed on the RHEED screen. After the oxide is removed from the surface, the substrate temperature is adjusted to a predetermined value which is proper for the growth of desired material. When the substrate temperature is stabilized the corresponding group-III shutters are opened. The fluxes of the group-III materials must be controlled precisely as $Al_xIn_{1-x}As$ and $In_yGa_{1-y}As$ are lattice matched to InP at only certain x and y values. Thus, multiple calibration runs are performed in order to achieve lattice matched compositions for AlInAs and InGaAs during optimization of the growth conditions.

The mole fraction in a ternary compound is determined by the growth rates of the binary compounds forming the compound. For example, the mole fraction of $Al_xIn_{1-x}As$ is determined by the growth rates of AlAs and InAs. The ratio of the growth rate of AlAs to the total growth rate (sum of the growth rates of AlAs and InAs) will determine the Al mole fraction in the $Al_xIn_{1-x}As$ ternary. The growth rates are determined by group-III fluxes in III-V Epitaxy as the sticking coefficients of the group V materials is almost zero over a specific substrate temperature. During optimization of the growth of AlInAs and InGaAs, In flux was kept constant, and the Al and Ga fluxes were adjusted properly. Changing the In flux needs abrupt changes at the effusion cell temperatures causing transients and instability in the corresponding fluxes. Once the growth rates of InAs and AlAs were determined by X-Ray Diffractometery (XRD) technique, the AlAs growth rate was adjusted properly for the lattice matched composition while keeping the InAs growth fixed at the predetermined value.

XRD is a non-destructive measurement technique which is used to characterize the quality and the structure of the crystal. X-rays primarily interact with electrons in atoms. When X-ray photons collide with electrons, some photons from the incident beam are deflected away from the direction where they originally travel, much like billiard balls bouncing off one another. If the wavelength of these scattered X-rays do not change (meaning that X-ray photons do not lose any energy), the process is called elastic scattering (Thompson Scattering) meaning that only momentum has been transferred in the scattering process. These are the X-rays that we measure in diffraction experiments, as the scattered X-rays carry information about the electron distribution in materials [65]. Diffracted waves from different atoms can interfere with each other, and the resultant intensity distribution is strongly modulated by this interaction. If the atoms are arranged in a periodic fashion, as in crystals, the diffracted waves consist of sharp interference maxima (peaks) with the same symmetry as in the distribution of atoms. Measuring the diffraction pattern therefore allows us to deduce the distribution of the atoms in a material.

The intensity peaks in the X-Ray Diffraction pattern are directly related with the atomic distance of the crystal, and it is defined by famous Bragg's Law which is expressed as

$$n\lambda = 2d\mathrm{Sin}\theta. \tag{3.9}$$

Here λ is the wavelength of the X-Ray, d is the spacing between the atoms and θ is the angle of incidence of the X-Ray. If the examined sample is a single crystal, then the spacing between the atoms will be equal to the lattice constant of the crystal. Thus, by rotating the sample around the Bragg's angle, a diffraction intensity curve is obtained. This curve is called rocking curve and critical structural information such as layer thicknesses and mole fractions may be extracted from this curve. A simple illustration of rocking curve measurement is given in Fig. 3.4.
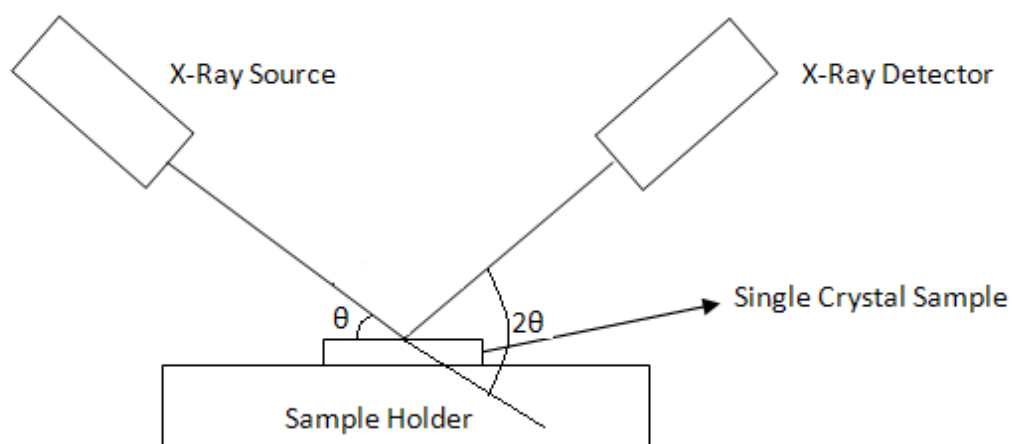
Figure 3.4 Illustration of Rocking curve measurement setup

Once the rocking curve of a crystal is obtained, different lattice constants in the crystal can be resolved by the help of intensity peaks. Each lattice constant will correspond to a different intensity peak, and the mole fraction of any layer can be determined by fitting the measurement curve to the well defined theory with a computer program.

The XRD measurements were made with a Rigaku 4 crystal High Resolution X-Ray Diffractometer (HR-XRD) system which is shown in Fig. 3.5.

Figure 3.5 Photograph of the Rigaku HR-XRD system

Fig. 3.6 shows the rocking curve of InAlAs layer grown on InP substrate. There is only one intensity peak in the measurement suggesting that the AlInAs and InP epilayers have the same lattice constant (lattice-matched condition).
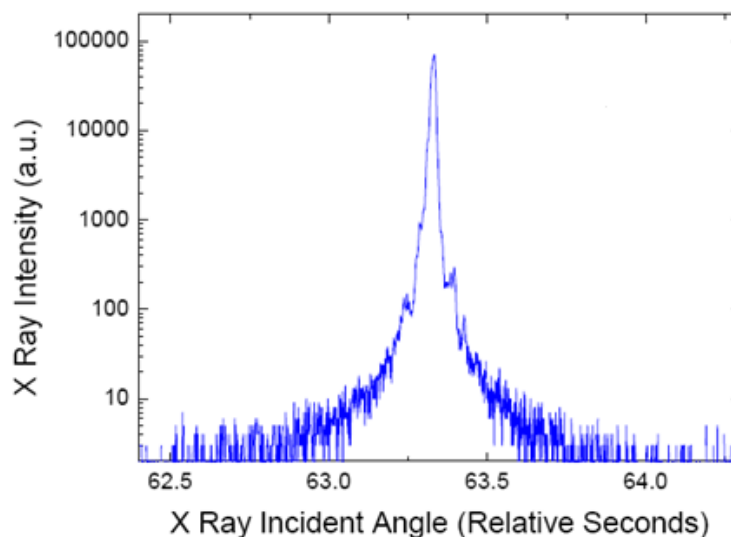
Figure 3.6 Rocking curve measurement result of InAlAs layer grown on InP

The growth rates for $In_xGa_{1-x}As$ were also optimized by using the same methodology, and In mole fraction of 0.53 ± 0.01 was obtained during the growths.

When dealing with the growth of In including compounds, the substrate temperature is a key parameter. Good quality layers are obtained at high substrate temperatures [2]. However, the sticking coefficient of In starts to decrease when the substrate temperature exceeds 530 °C [66] . In this work, the growth of In including layers were performed at 480 °C substrate temperature. When a low bandgap material such as InGaAs is deposited on InP substrate, the emissivity is changed, and the substrate temperature starts to increase with increasing InGaAs thickness. However, it is important to maintain the substrate temperature within ±5 °C during the growth; otherwise the InGaAs layer may relax ending up with a useless epilayer. Therefore, the substrate temperature was decreased with a special profile after the InGaAs growth was started, and the temperature of the substrate was held within the acceptable limits throughout the growth.

Doping (n-type) of quantum wells during the MBE growth is performed by intentionally incorporating Silicon. The doping density is determined by the amount of Si atoms incorporated to the layer, and the effusion cell temperature defines the number of Si atoms impinging on the substrate. Thus adjusting the Si effusion cell temperature to a predefined value provides the desired doping level. In order to determine the relation between the Si effusion cell temperature and the doping density, calibration runs were performed, and the doping densities were measured. The measurements were performed on a Hall Effect measurement setup with Van der Pauw configuration.

3.3 AlInAs/InGaAs MWIR QWIP FPAs on InP Substrates

Earlier work on AlInAs/InGaAs MWIR QWIPs reported cut-off wavelength considerably smaller than 5 μm. However, the photon exitance spectrum of near 300 K objects calls for detector cut-off wavelengths near 5 μm in order to increase the photon flux received by the sensor. For this purpose, we have investigated AlInAs-InGaAs QWIP epilayer structures consisting of thirty $In_{0.53}Ga_{0.47}As$ QWs with different thicknesses in the range of 22-30 Å [67] [29] [32]. The $Al_{0.48}In_{0.52}As$ barriers were 300 Å thick in the structures. The top and bottom contact layers were InGaAs doped to $1x10^{18}$ cm^{-3}.

In order to assess the promise of the AlInAs/InGaAs material system at large format FPA level, 640x512 QWIP arrays were fabricated with the above described epilayer structures. Optical grating and mesas with 25 μm pitch were defined by optical lithography. Following the formation of ohmic contacts, reflector, passivation, and under-bump metallization, indium bumps were formed through electro-plating process. The FPA was flip-chip bonded to Indigo ISC9803 read out circuit and the processing was completed by underfill injection and substrate thinning with a high resolution lapping/polishing system.

Detailed pixel level characterization was performed on test QWIPs having the same dimensions (~21x21 μm^2) with the pixels of a typical large format FPA. These test QWIPs, which were fabricated through our FPA process, include all the features of a typical QWIP FPA pixel, and were hybridized to a fan out substrate by flip-chip bonding in order to allow optical characterization with backside illumination. The characterization of the detectors in this manner facilitates accurate estimation of the FPA pixel characteristics due to the identical structures of test detectors and FPA pixels. Due to the very high electrical resistance of the small size detectors, test detectors were parallel connected in matrix form in order to facilitate reliable electrical and optical measurements. While the detectors were not anti-reflection coated, backside reflection loss was taken into account in the related measurements. The test detectors were installed in a Dewar with $f/1.5$ optical aperture. The Dewar window was transparent to the radiation in the wavelength interval of 3-12 μm. The responsivity spectrum of the test detectors were measured with an FTIR system and a preamplifier with the setup shown in Fig. 3.7 schematically.

First the spectrum of the infrared light source of the FTIR is measured with a pyrolytic reference detector. This reference detector's response is almost flat, and it is independent of the wavelength. Following this measurement, the test detectors installed in the dewar are placed in the sample compartment of the FTIR system, and the responsivity spectrum of the test detectors is measured. Finally, the measured data is normalized using the reference detector data.
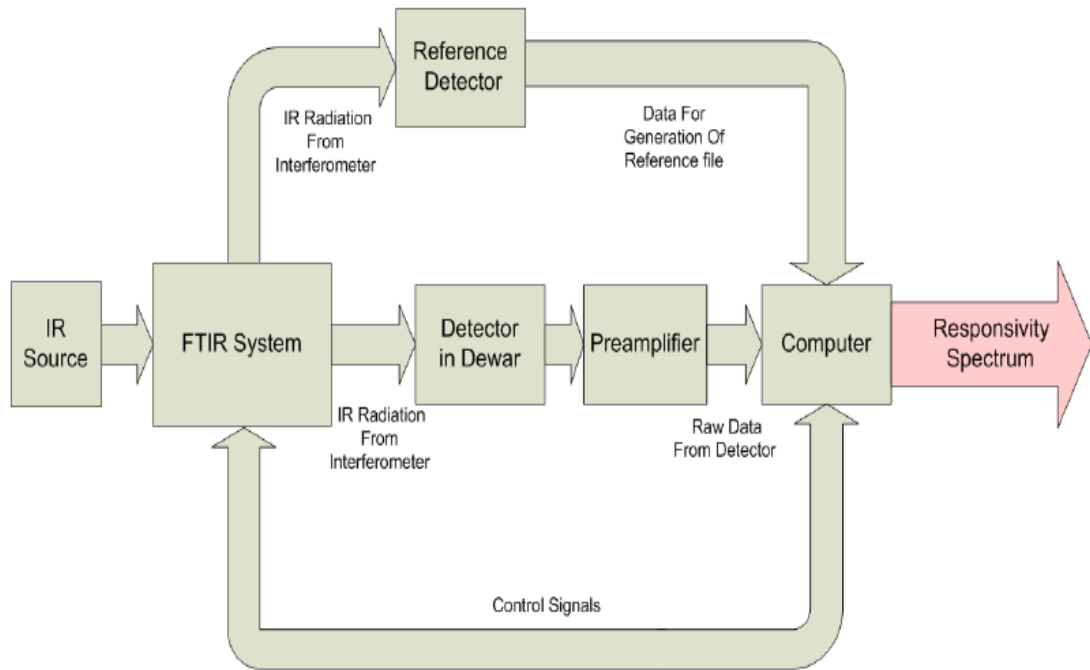
Figure 3.7 Schematic representation of test setup for measuring responsivity spectrum [32]

By using this method, the characteristic of the IR source, and the absorption of air are cancelled out, and the actual spectrum of the QWIP is measured. On the other hand, there is no information on the power impinging on the detector during the measurement. Thus, the responsivity values obtained by this measurement are arbitrary and provide no information about the detector performance.

After measurement of the dark and photo current, the responsivity and detectivity of the test detectors were measured by using a blackbody source, a chopper, a preamplifier and a lock-in amplifier. The instruments were controlled by a PC and the incidence on the detector was calculated by a software based on the distance between the detector and blackbody source, the detector area, the blackbody aperture and the blackbody temperature. Test detectors were placed in front of the blackbody source whose radiation was modulated with the chopper installed in front of it. The detector was biased through the preamplifier, and the response of the detectors to the black body was measured with the lock-in amplifier by correlating the chopper frequency and the measurement frequency of the lock-in amplifier. By the help of this setup, the blackbody voltage responsivity of test detectors was measured. In

order to obtain the blackbody current responsivity, the blackbody voltage responsivity was multiplied with the gain of the preamplifier. Peak responsivity of the detector was calculated by multiplying the blackbody responsivity with the peak factor of the detector.

The noise level of the detectors is needed to be measured in order to be able to calculate the detectivity. The noise is measured at the modulation frequency of responsivity measurement when the detectors are seeing 300 K background. Once the peak current responsivity, noise current, detector area, and the measurement bandwidth is known the peak detectivity can be calculated. The setup for measuring the responsivity and the detectivity is given in Fig. 3.8.
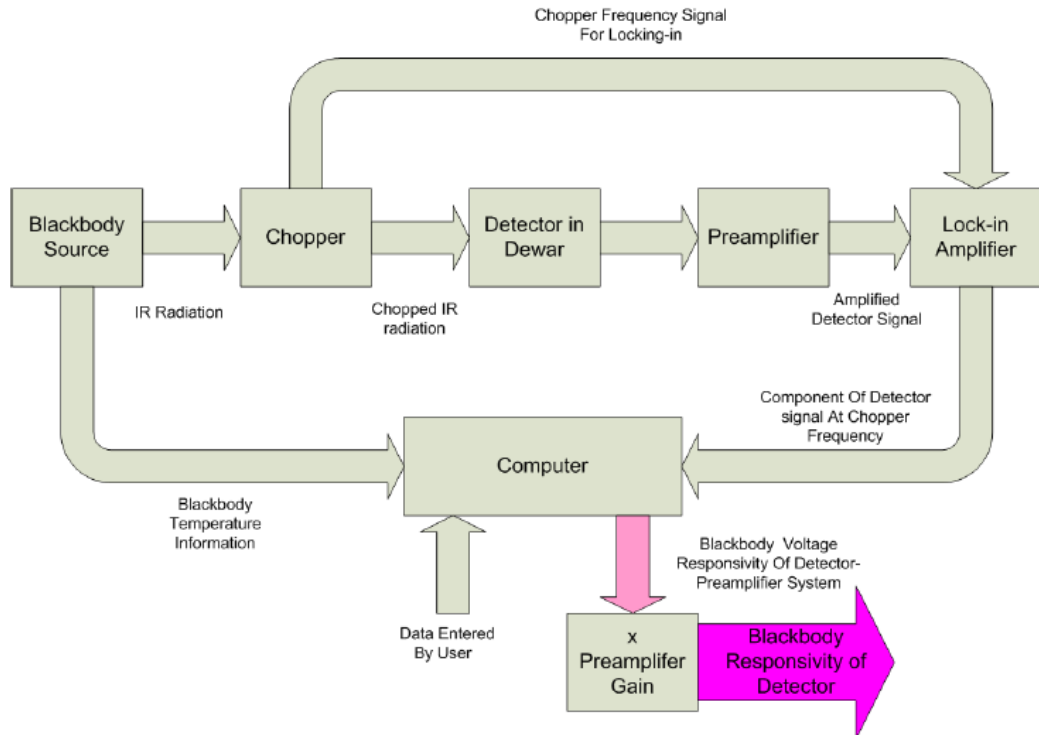
Figure 3.8 Illustration of responsivity and detectivity measurement setup [32]

Fig. 3.9 shows the normalized responsivity spectrum of the test detectors with 22 and 23 Å QW thicknesses grown in our laboratory in comparison with those of two other AlInAs/InGaAs QWIPs with 26 and 30 Å thick QWs, which were grown at IQE Inc. While the peak responsivity wavelength does not change significantly, the cut-off wavelength is shifted from 4.15 to 5.1 μm with significant broadening in the

spectrum as the QW thickness is decreased from 30 to 22 Å in which case $\Delta\lambda/\lambda p$ becomes as high as 32% [67]. This is an important achievement as the photon exitance spectrum of near 300 K objects calls for detector cut-off wavelengths near 5 μm in order to increase the photon flux received by the sensor.
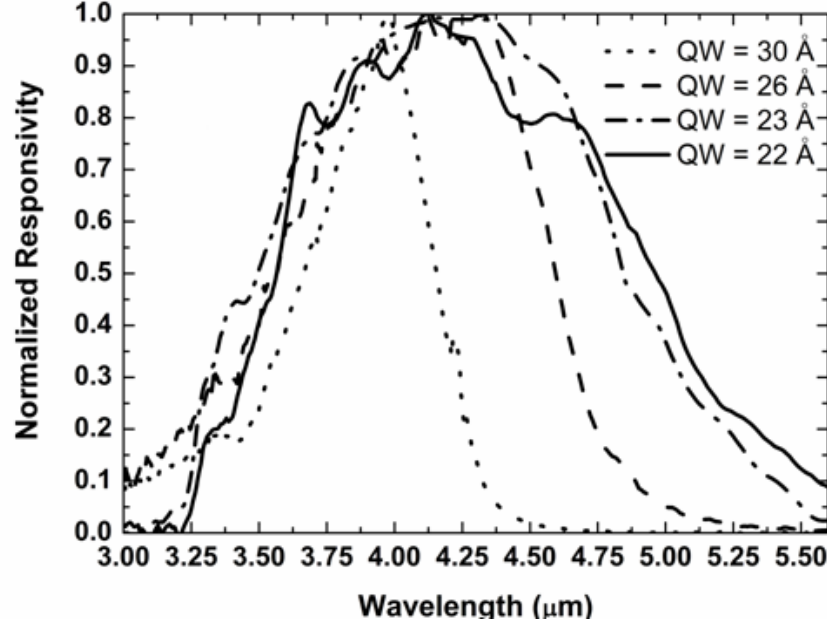
Figure 3.9 Normalized responsivity spectrums of the test detectors with 22, 23, 26 and 30 Å thick quantum wells [67].

Fig. 3.10 shows the detectivity ($f/2$) versus temperature characteristic of the test detectors with 23 Å QW thickness (QW doping density=4×10^{18} cm^{-3}) [67] [29]. The inset shows the photocurrent ($f/2$, 300 K background) and dark current of one pixel versus reverse bias (mesa top negative). The detectors are BLIP at a temperature as high as 112 K with $f/2$ optics up to a reverse bias voltage of 2.75 V. Both the dark and photocurrent were observed to be slightly smaller under forward bias (mesa top positive) suggesting a larger barrier for AlInAs on InGaAs interface when compared with InGaAs on AlInAs interface.

The BLIP peak detectivity of the detectors with 23 Å QW thickness is ~7×10^{10} cmHz$^{1/2}$/W with $f/2$ aperture. The broad spectral response and reasonably high peak responsivity provide a large integrated blackbody response. The peak responsivity and the noise gain of this device saturate at ~70 mA/W and ~0.5, respectively, when the bias approaches 3 V. The peak quantum efficiency (η) of the test detectors is determined to be around 4%. The measured detector gain (0.5) is similar to those of

AlGaAs-GaAs and AlGaAs-InGaAs QWIPs. However, the gain is significantly lower than that of LWIR QWIPs with InP barriers possibly due to the lower energy separation between central (Γ) and satellite valleys in the conduction band of $Al_{0.48}In_{0.52}As$.
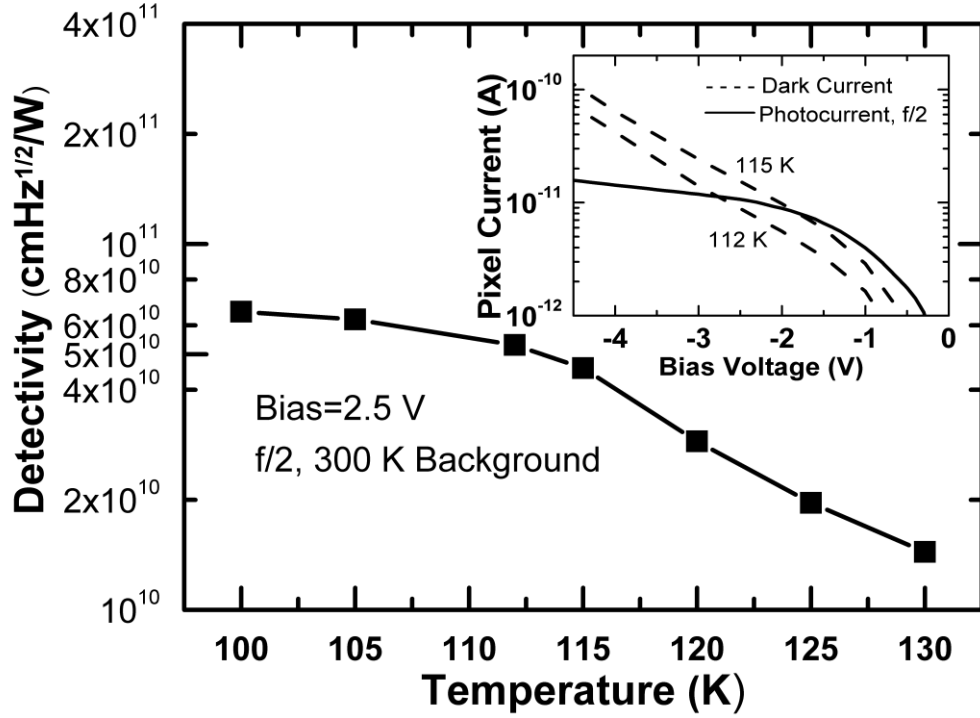
Figure 3.10 Temperature dependence of the peak detectivity (*f/2*) of the test detectors with 23 Å quantum well thickness. The inset shows the pixel photocurrent (*f/2*, 300 K background) and dark current [67] [29]

It is clear from Fig. 3.10 that the detector is BLIP at 112 K operating temperature up to approximately -3 V biasing voltage with *f/2* optics. Under sufficiently high temperatures and low bias voltages, the normalized dark current of QWIP depends on temperature as follows [24]

$$\frac{I_D}{T} \propto e^{-\frac{(E_C - E_F)}{kT}} \tag{3.10}$$

where E_C is the energy difference between the barrier height (E_b) and bound ground state (E_1), and E_F is the Fermi level measured with respect to E_1. Figure 3.11 shows the activation energy E_A of the dark current under various bias voltages.

64
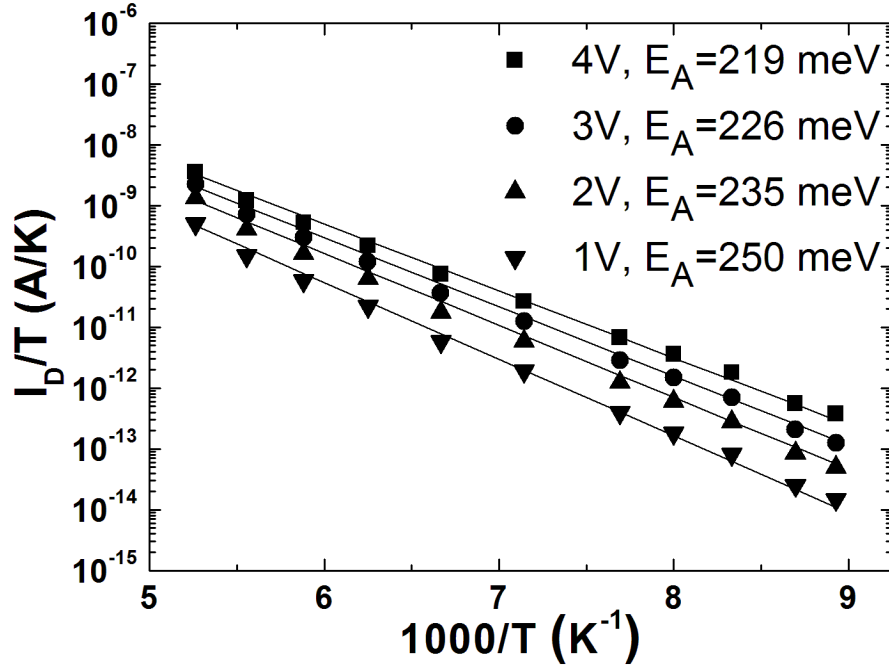
Figure 3.11 Activation energies under various bias voltages

As expected, the activation energy, $E_A=E_C-E_F$, decreases with increasing bias due to barrier lowering effects [68]. The measured activation energy under low bias (1 V) is in reasonable agreement with the cut-off energy of 253 meV yielded by the optical measurements.

The 640x512 AlInAs-InGaAs QWIP FPA was characterized using a Dewar with *f*/2 aperture connected to imager electronics yielding 14-bit digital output, as well as analog video output. The digital output (14-bit) of the FPA was recorded by a computer while the FPA was looking at a large area differential blackbody. The differential blackbody had two large area plates. One of these plates was floating at room temperature while the other plate was being heated by a controller in order to achieve a fixed temperature difference between the plates. 128 frames of data set were recorded with the software when the FPA was looking to the room temperature plate (cold data). This was followed by another 128 frames of data set recording when the FPA was exposed to heated plate (hot data). Later, these frames were averaged and the average cold and hot data were obtained. The difference between the hot and the cold data gives the response of the detector to a fixed temperature difference. The temporal noise of the FPA was calculated by finding the standard

deviation of each pixel from the mean value of the average data. Later all, NETD was obtained by dividing the noise value to the responsivity value and multiplying it with the temperature difference. The mean NETD of the FPA was calculated by averaging the NETD values of the pixels. The pixels whose NETD value was higher than triple of the mean NETD were denoted as dead pixels. The operability was defined as the ratio of number of the good pixels to the number of the dead pixels.

Fig. 3.12 shows the NETD histogram of the FPA measured at 80 K under 3 V reverse bias with *f*/2 optical aperture and 20 ms integration time. The mean NETD is as low as 14 mK with an operability of 99.4%. The NETD nonuniformity of the FPA is 18% without calibration and field of view correction. Fig. 3.13 shows a thermal image recorded with this QWIP FPA.
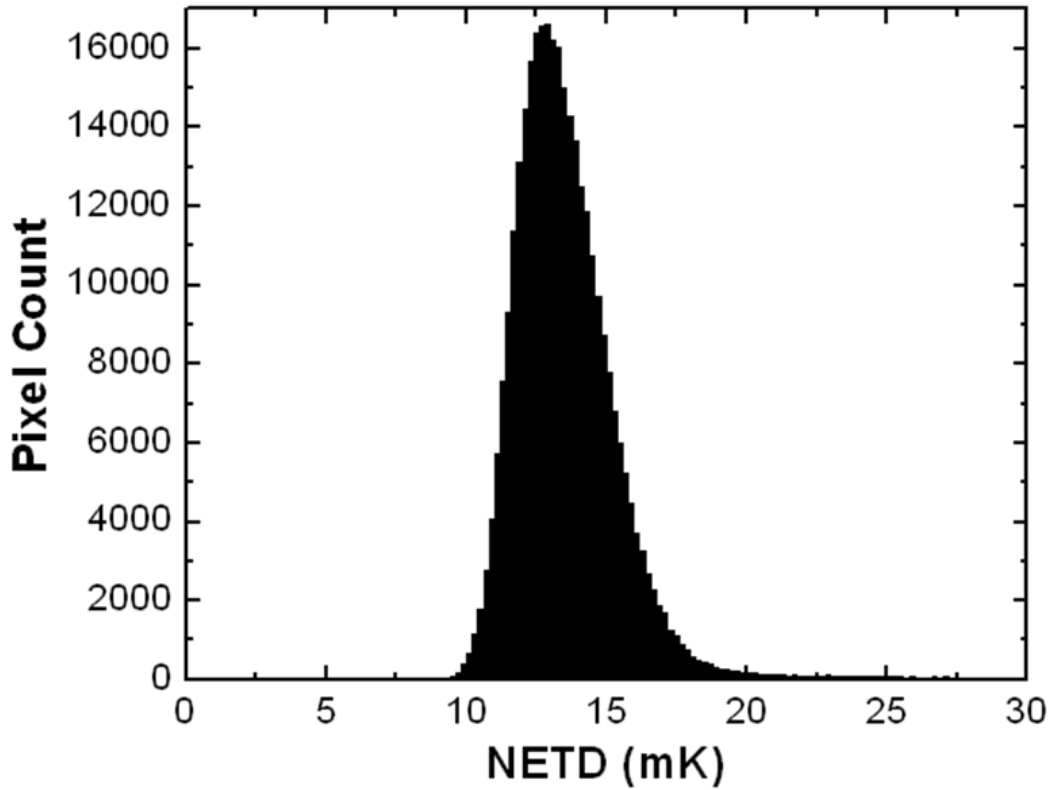
Figure 3.12 NETD histogram of the 640x512 AlInAs/InGaAs QWIP FPA fabricated using the structure with 23 Å QW thickness (80 K FPA temperature, -3 V bias, *f*/2 optical aperture and 20 ms integration time). The mean NETD is 14 mK [67] [32].

Figure 3.13 An indoor thermal image recorded with AlInAs/InGaAs QWIP FPA [67]

The above observations are comparable to the best results reported for MWIR AlGaAs/InGaAs QWIPs both at pixel and FPA level [39]. It should be noted that the pixel responsivity and the FPA NETD can significantly be improved by optimization of the optical grating structure.

The above described work demonstrates the potential of the AlInAs/InGaAs material system on InP substrate for MWIR QWIP applications. Sufficiently high peak responsivity and detectivity with broad spectral response and suitable cut-off wavelength, as well as high BLIP T and good uniformity make this material system an excellent lattice matched alternative to the standard strained AlGaAs/InGaAs system which suffers from the degradations of lattice mismatched epitaxy. In conclusion, AlInAs/InGaAs material system displays high potential for both single band MWIR QWIPs as well as fully lattice matched MWIR/LWIR dual-band QWIPs when combined with the InP/InGaAs or InP/InGaAsP material systems.

3.4 LWIR Strained InP/InGaAs QWIPs on InP Substrate

The preceding section presented the characteristics of InP based MWIR QWIPs in the pixel and FPA levels. In this section, we will discuss the potential of the strained InP/InGaAs material system for LWIR QWIPs. It will be demonstrated that QWIPs based on the strained $InP/In_{0.48}Ga_{0.52}As$ system provide excellent characteristics and desirable spectral response eliminating the need for the utilization of a quaternary material in order to extend the cut-off wavelength. We also experimentally demonstrate that the InP/InGaAs material system at this composition satisfies the requirements of most low integration time/low background applications where AlGaAs/GaAs QWIPs can not be utilized due to low conversion efficiency and read-out circuit noise limited sensitivity.

The epilayer structure of the InP/InGaAs QWIP was grown in our laboratory on 3-inch semi-insulating InP substrate by solid source molecular beam epitaxy using optimized growth parameters as discussed in section 3.2. The QWIP epilayer structure is made up of forty $In_{0.48}Ga_{0.52}As$ QWs (55 Å thick, $N_D=5.5x10^{17}$ cm^{-3}) which were sandwiched between 400 Å thick InP barriers. The top and bottom $In_{0.53}Ga_{0.47}As$ contacts layers were doped at $N_D=1x10^{18}$ cm^{-3}. The structure of strained LWIR QWIP is given in Fig. 3.14.
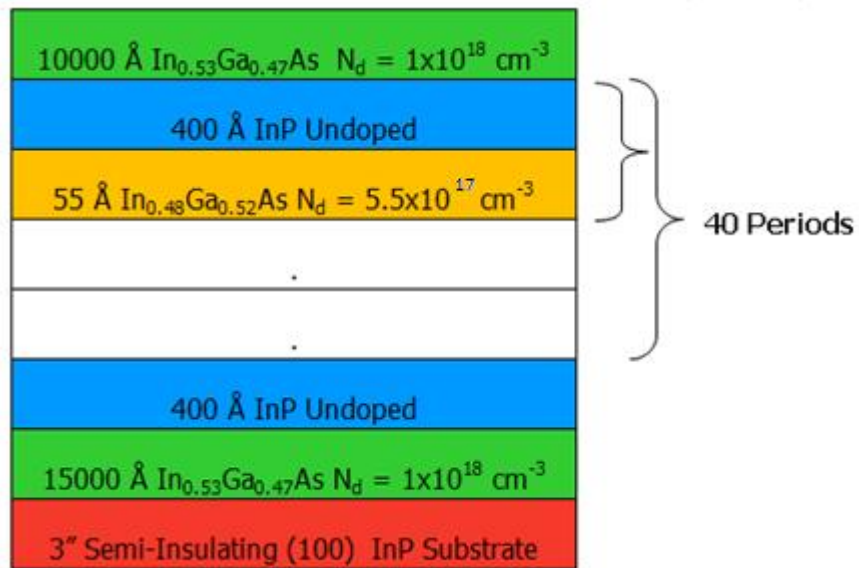
Figure 3.14 The structure of slightly strained LWIR QWIP

A large format (640x512) FPA was fabricated from the wafer with the fabrication steps described in section 2.4. A cross type optical grating structure was defined by optical lithography and dry etching. Mesas with 25 µm pitch were formed by reactive ion etching with $SiCl_4$:Ar mixture using an inductively coupled plasma system. Following the formation of ohmic contacts, reflectors and underbump metallization, In bumps were grown on the mesas through electro-plating. The FPA was hybridized to Indigo ISC9803 ROIC using a high precision flip-chip aligner/bonder. After underfill injection, the substrate of the FPA was thinned to 10 µm followed by polishing with a high resolution lapping/polishing system.

Test detectors (21x21 $µm^2$) with features identical to the FPA pixels were fabricated using the same wafer. The test detectors were flip-chip bonded to a fan-out substrate for pixel level electrical and optical characterization. Due to their high electrical resistances, test detectors were parallel connected for reliable electrical and optical measurements. While the detectors were not anti-reflection coated, backside reflection loss was taken into account in the related measurements.

Fig. 3.15 shows the normalized spectral response of the InP/$In_{0.48}Ga_{0.52}As$ test QWIPs with a cut-off wavelength (λ_c=9.7 µm) considerably larger than that of lattice matched InP/$In_{0.53}Ga_{0.47}As$ QWIPs (λ_c~8.5 µm) [26]. The peak responsivity of the detectors is at 8.9 µm with $\Delta\lambda/\lambda_p$=17%. Extending the cut-off wavelength above 9 µm is important especially for applications targeting long distance detection under high humidity conditions. In order to achieve this, sufficiently high quantum efficiency is needed to keep the detector operating temperature at an acceptable level
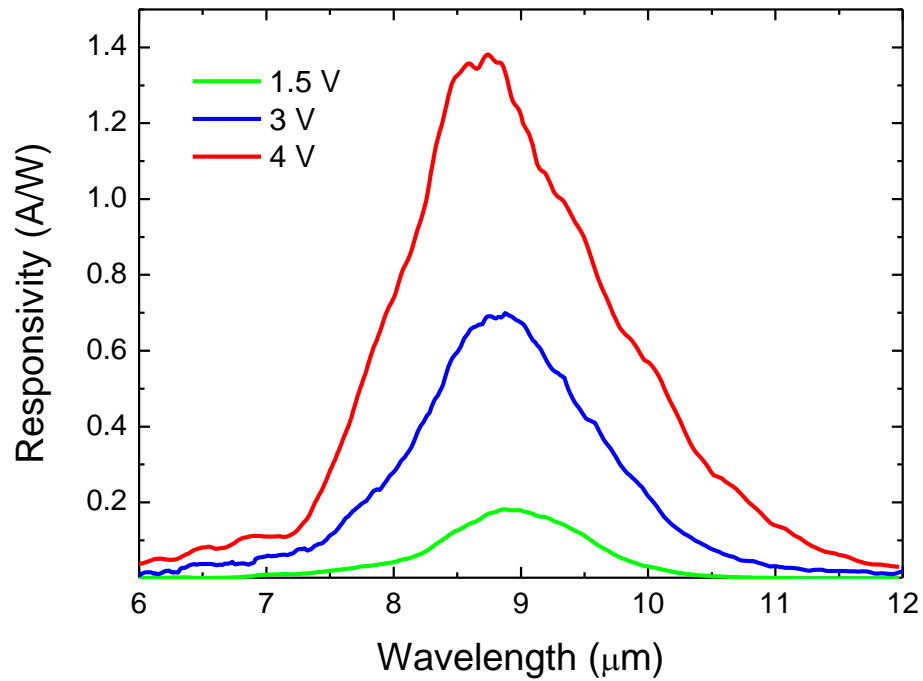
Figure 3.15 Responsivity spectrum of InP/In$_{0.48}$Ga$_{0.52}$As test QWIPs under various bias voltages (mesa top negative) [35]

The transmission of water vapor decreases dramatically, when the precipitation increases. Precipitation is defined as the height of a cylinder which condensates all the H$_2$O molecules in an air cylinder [3] and it is denoted by "h". The schematic representation for definition of precipitation is given in Fig. 3.16.
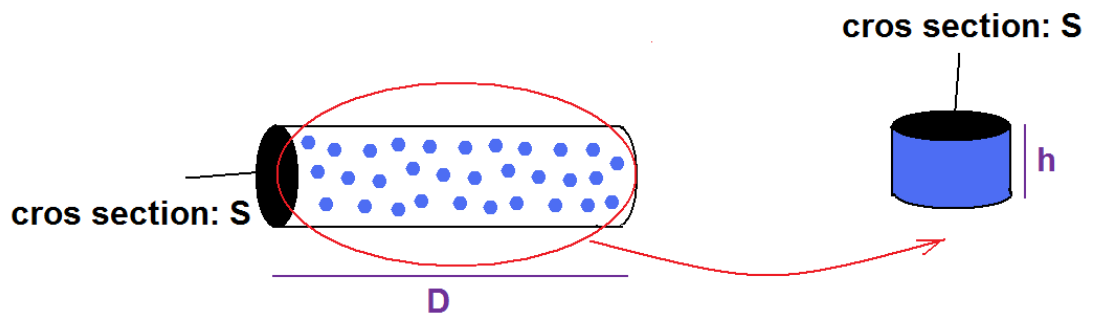
Figure 3.16 Schematic representation of precipitation [3]

The transmission of water vapor for different precipitation levels is shown in Fig. 3.17.
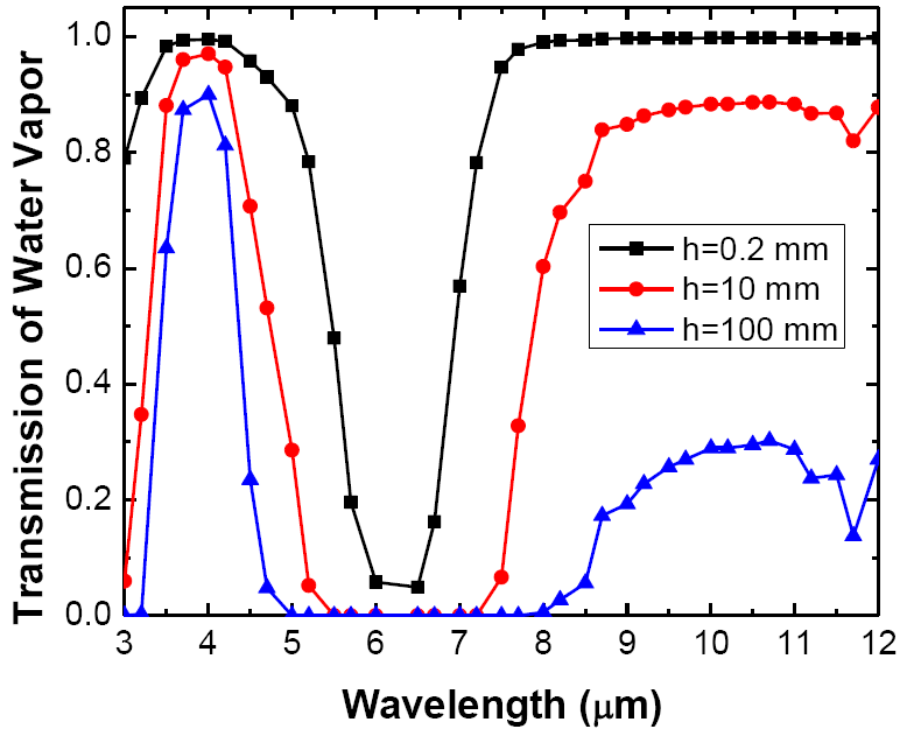
Figure 3.17 Transmission of water vapor vs. wavelength for different precipitation levels [3] (data from [69])

The conventional AlGaAs/GaAs QWIPs are usually designed to make detection between 8-9 μm. However, it is seen from Fig 3.17 that the transmission of water vapor is low between 8-9 μm under high precipitation levels. Thus, the imaging performance of these QWIP FPAs is significantly degraded under high humidity conditions due to the high absorption through the imaging path. Extending the cut-off wavelength above 9 μm is important especially for applications targeting long distance detection under high humidity conditions. However, the dark current of the QWIP increases exponentially with increasing cut-off wavelength. Hence, sufficiently high quantum efficiency is needed to keep the detector operating temperature at an acceptable level in order to extend the cut-off wavelength above 9 μm.

Fig. 3.18 shows the dark current versus bias characteristics and the photocurrent (*f*/1.5) of the test detectors (identical to FPA pixels). Despite the long cut-off wavelength, the device displays background limited performance (BLIP) at a temperature of 67 K under moderately large reverse bias voltages.
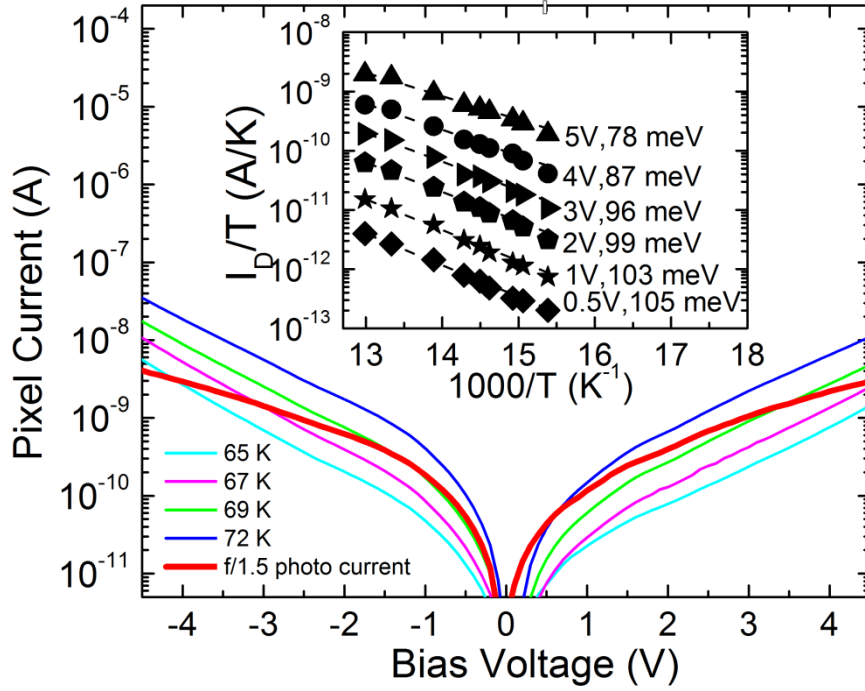
Figure 3.18 Current-voltage characteristics of the test detectors (identical to FPA pixels) and the dark current activation energy plot for different reverse bias voltages [35].

The dark current activation energy plot is shown in the inset of Fig. 3.18. Based on the QW doping concentration, the Fermi level is expected to be ~20 meV above E_1. The measured thermal activation energy under low bias is in reasonable agreement with the optical activation energy yielded by the spectral response measurements.

Fig. 3.19 shows the peak responsivity and the photoconductive (g_p) and noise (g_n) gains versus bias voltage. The noise gain of the device was extracted from noise and current measurements at 77 K detector temperature. The noise measurements were performed with a low noise preamplifier and a lock in amplifier at low frequencies in order to remain within the bandwidth of the preamplifier. The noise and photoconductive gains of the device are expected to be nearly equal under moderately large bias voltages in which case the peak quantum efficiency is determined to be as high as 12%. The variations of the gain and responsivity with bias are in good agreement under moderately large voltages if η is kept constant at 12% showing that η does not considerably change with bias in this range. The photoconductive gain of the device is extracted from the responsivity measurement

72

results using this value of η. The noise gain deviates from the photoconductive gain under large bias voltages which is attributed to impact ionization [70].
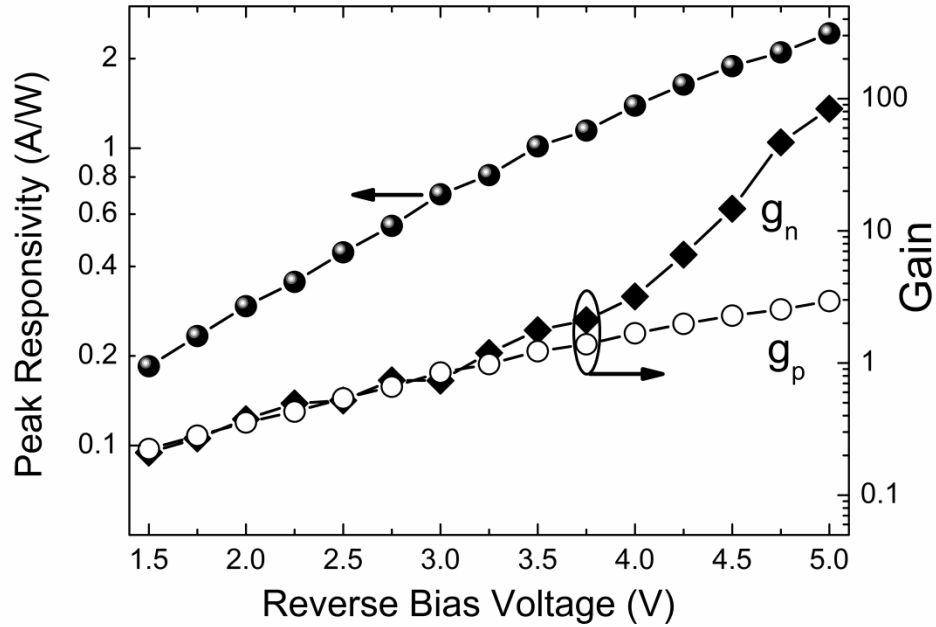
Figure 3.19 Bias dependency of the peak responsivity and the photoconductive and noise gains [35].

Fig. 3.20 shows the variation of the peak detectivity (f/1.5) with the detector temperature under various bias voltages offering different photoconductive gains and responsivities. Variation of the 65 K peak detectivity (f/1.5) with bias voltage is shown in the inset. It should be noted that the detectors provide reasonably high detectivities with impressively large responsivities. The conversion efficiency of the device ($\eta.g$=20% under 4 V) is larger than that of a typical AlGaAs/GaAs QWIP by a factor of four. On the other hand, the gain (and responsivity) of the detectors can be varied in a wide range with the applied bias while preserving the detectivity at a sufficiently high level. The photoconductive gain changes by nearly an order of magnitude when the bias voltage is changed in the range of 1.5-4 V which is not possible with the QWIPs fabricated with the standard material system AlGaAs/GaAs due to the saturation of the gain (drift distance) at considerably smaller values [24]. In this sense, InP/InGaAs QWIPs offer an important advantage over AlGaAs/GaAs QWIPs as explained below.
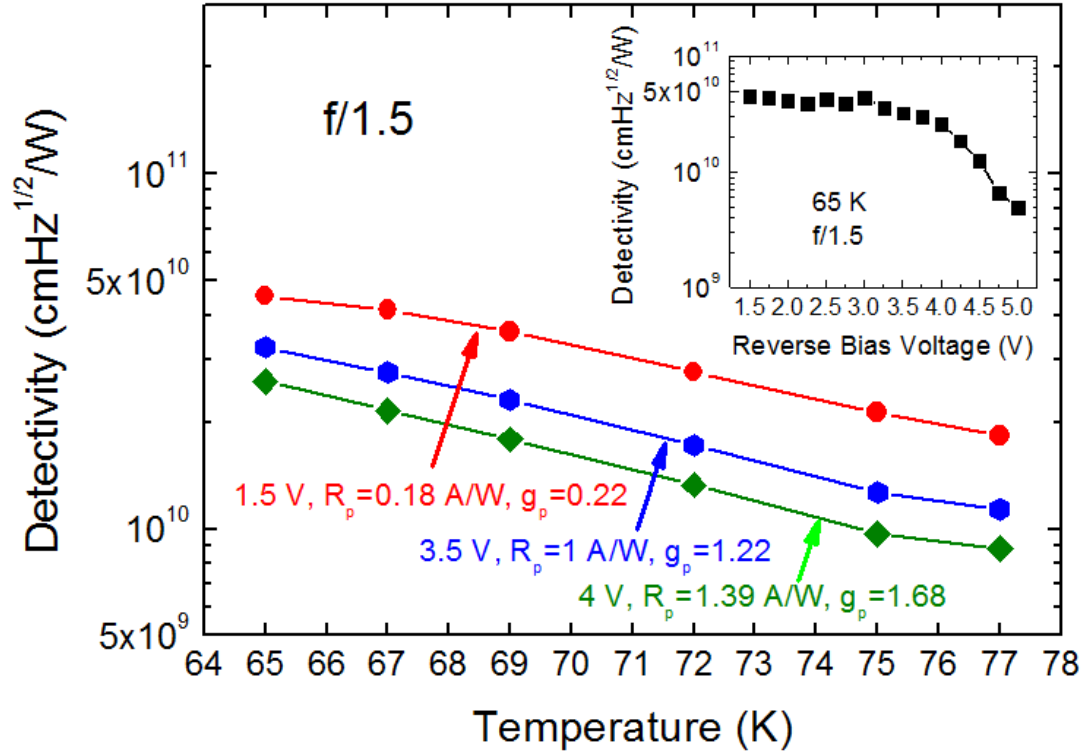
Figure 3.20 Variation of the peak detectivity (*f*/1.5) with detector temperature under various bias voltages. Variation of the 65 K peak detectivity with bias voltage is shown in the inset [35].

While a large gain improves the conversion efficiency and responsivity of the device, the detectivity is independent of the gain. This makes the temporal noise equivalent temperature difference (NETD) of the FPA virtually gain independent under BLIP conditions. However, the FPA NETD becomes dependent on gain due to the limited capacity of the read out integrated circuit (ROIC) capacitors when there is substantial photon flux or when the signal to noise ratio of the FPA/ROIC hybrid is limited by the ROIC noise under low background conditions.

In the operating wavelength range of LWIR sensors, NETD of a BLIP sensor (excluding ROIC noise) can be expressed approximately as [11] [18]

$$NETD = \frac{kT^2}{h\nu}\sqrt{\frac{2g}{N_s}} \tag{3.11}$$

where $h\nu$ is the photon energy and N_s is the collected photoelectrons. Since N_s depends on the photoconductive gain (g) of the sensor through the responsivity,

NETD is independent of the gain if there is no limitation imposed by the limited capacity of the ROIC capacitors. However, the integration time (τ) must be adjusted properly to prevent the ROIC capacitors from saturating, if the FPA is exposed to substantial photon flux with a sufficiently large integration time. This limitation on N_s by the ROIC capacitors makes the NETD of the device under this condition proportional to $g^{1/2}$ as discussed by Schneider *et al.* [11]. If the integration time is not limited by the application, large device gain degrades the camera sensitivity in this case due to the need for short integration times as a result of high sensor responsivity. On the other hand, large gain is needed in the case of low background or high frame rate (short integration time) conditions where the read-out noise becomes important in determining the system sensitivity. Under these conditions, NETD can be expressed as [18]

$$NETD = \frac{kT^2}{h\nu} \frac{Q_{ROIC}}{\tau R \varphi_B} \tag{3.12}$$

where Q_{ROIC} is the noise charge of the ROIC, R is the responsivity and ϕ_B is the background radiation power. If the expression for the responsivity ($R = \frac{q\eta g}{h\nu}$) is inserted into Eq.(3.12), it can be seen that NETD becomes inversely proportional to the gain and integration time as follows

$$NETD = \frac{kT^2}{\varphi_B} \frac{Q_{ROIC}}{q\eta g \tau}. \tag{3.13}$$

High frame rate (short integration time) applications impose an upper limit on τ calling for a large gain in order to achieve acceptably low NETD values under such conditions.

Fig. 3.21 shows the noise- and photo-electrons generated by a fully BLIP QWIP FPA pixel with dimensions of 20x20 μm^2 while looking at blackbody targets at 260 and 290 K with *f/*2 aperture and different integration times. The calculations are made for different gain values while assuming that the detector is sensitive in the wavelength

range of 8.0-9.0 µm with η=10%. The noise (500 e⁻) and 50% electron capacity (5x10⁶ e⁻) levels of a typical ROIC are also shown in Fig. 3.21 for comparison.
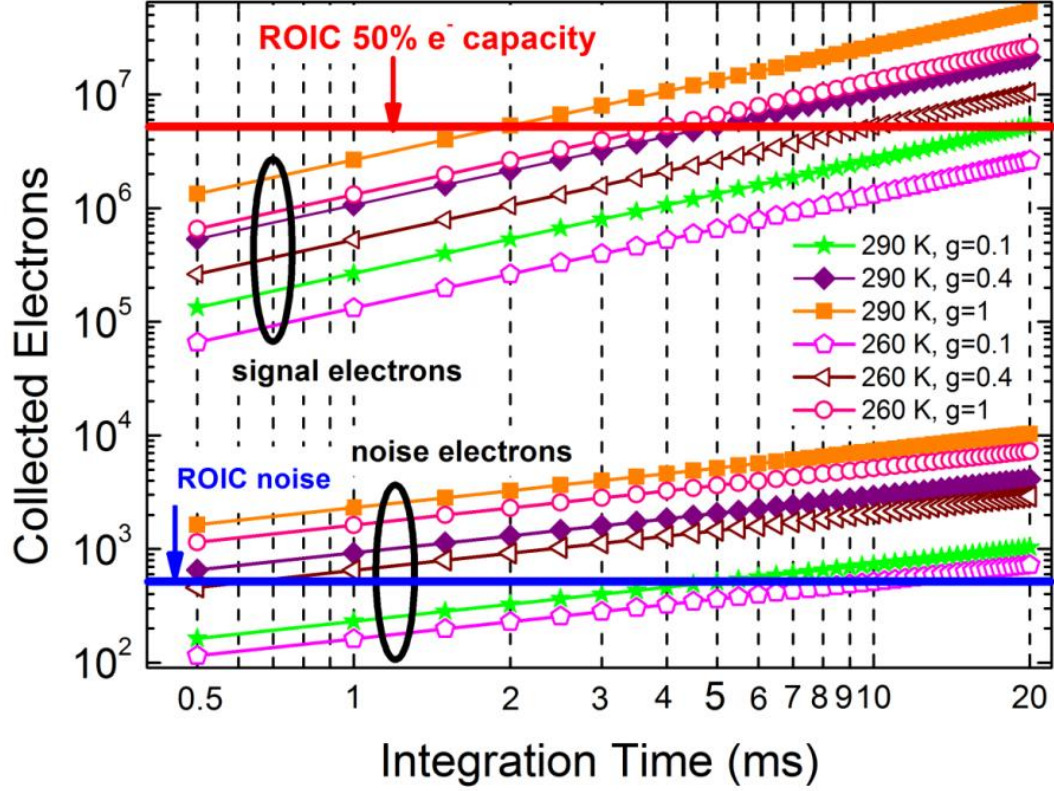
Figure 3.21 Noise- and photo-electrons versus integration time for a 20x20 µm2 FPA pixel sensitive in the wavelength range 8.0-9.0 µm (η=10%) looking at 260 and 290 K blackbody targets with *f/*2 aperture. The noise and 50% electron capacity levels of a typical ROIC are also shown for comparison [35].

As reflected by the results presented in Fig. 3.21, the sensitivity of the camera system approaches the limit established by the ROIC noise under low background/short integration time conditions in the case of low device gain. On the other hand, if the integration time is limited by the application at 2 ms, this detector needs a gain level of 1.0 in order to fill half of the integration capacitors of a typical ROIC while looking at 290 K target with *f/*2 aperture. It should be noted that larger *f* number optics and/or lower temperature targets require even larger gain values. The gain of a typical photoconductive AlGaAs/GaAs QWIP saturates at a value considerably smaller than 1 [24]. The drift distance in $Al_xGa_{1-x}As$/GaAs QWIPs with x~0.3 is less than 1 µm under large bias [51] corresponding to a maximum photoconductive gain

in the range of 0.3-0.5 for devices with a sufficiently large number of QWs [24]. Since tunneling leakage establishes a lower limit for the barrier thickness, the only possibility to achieve larger gain in AlGaAs/GaAs QWIPs is the employment of a smaller number of QWs in which case the quantum efficiency of the device would be degraded. The FPA demonstrated in this work provide both high quantum efficiency and a wide range of gain values (with sufficiently high detectivity) offering an additional flexibility in the design of thermal imagers especially for those to be operated under different conditions including high frame rates and/or low background environments.

The fabricated FPA was characterized in a Dewar with $f/1.5$ aperture connected to Pulse Instruments-System 7700. Without field of view correction and any calibration, the DC signal and NETD nonuniformities of the FPA are as low as 4.5% and 11%, respectively. Fig. 3.22 shows the NETD of the FPA calculated using the spectral response and detectivity measurements on the test detectors which are identical to the FPA pixels. The integration times shown at each bias voltage correspond to half-filled ROIC capacitors (1.1×10^7 electron capacity). Number of g-r noise electrons generated by the FPA pixels during this duration is also given for comparison with the ROIC noise level. NETD measurements made directly on the FPA are in reasonable agreement with those calculated with test detector data (25 mK under 1.5 V bias, $\tau = 1.8$ ms). The operability of the FPA is 99.5%.

The FPA yields reasonably low NETDs even under sub-millisecond integration with the sensitivity of the FPA/ROIC hybrid not limited by the read-out noise. It should be noted that considerable improvement in the NETD, especially under large bias voltages, can be obtained if the FPA is cooled to fully BLIP condition in which case it can be used with larger f-number optics and extended integration times if so desired.
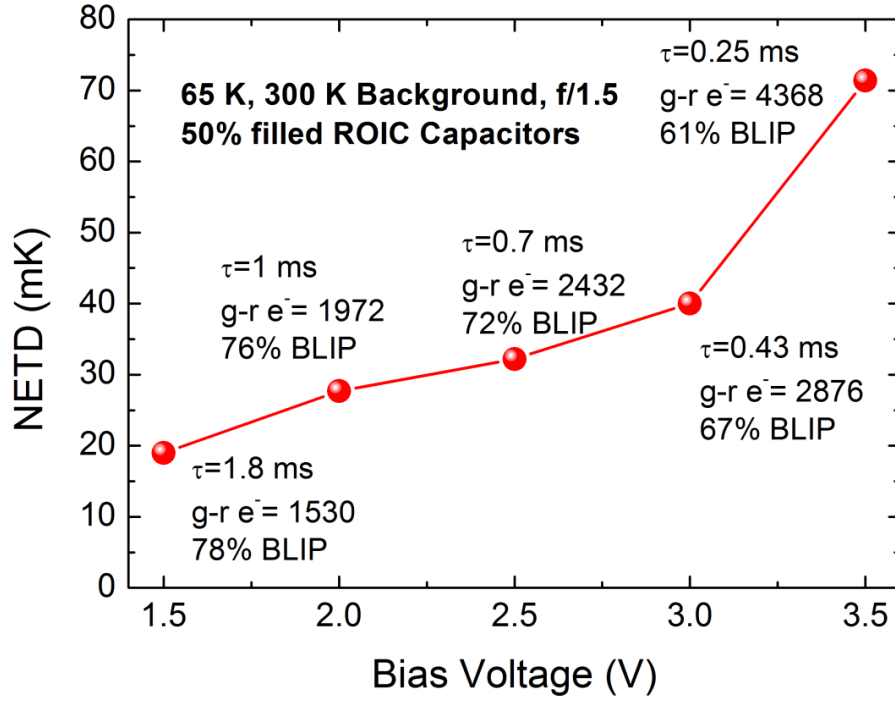
Figure 3.22 NETD of the FPA calculated using the measurements on the test detectors (identical to the FPA pixels). The integration times (corresponding to half-filled ROIC capacitors with 1.1×10^7 electron capacity) and the number of g-r noise electrons generated by the FPA pixels are given for each bias voltage [35].

Thermal images recorded with the FPA using a Dewar with *f/2* lens and 14-bit imager electronics under unusual conditions are shown in Fig. 3.23. The first image (a) is taken with the FPA cooled with liquid nitrogen at ~80 K under low bias, while the second image (b) is taken with a very short integration time of 500 μs under 3 V bias voltage (g_p=0.85) in snapshot mode when the FPA temperature is 65 K. The images display the successful operation of the FPA under these conditions due to high quantum efficiency and large conversion gain.

Figure 3.23 Thermal images recorded with the 640 × 512 InP/InGaAs FPA (a) at ~80 K detector temperature under low bias (0.3 V), (b) at ~65 K sensor temperature under 3 V bias voltage with an integration time of 500 μs and *f/*2 optics [35]

3.5 Concluding Remarks

The potential and advantages of the AlInAs/InGaAs and strained InP/InGaAs material systems for MWIR and LWIR QWIPs are assessed in this chapter. It has been shown that AlInAs/InGaAs MWIR QWIP structure on InP substrate is an excellent lattice matched alternative to the conventional InGaAs/AlGaAs QWIPs.

Both the pixel and FPA level characterization results showed that the performance of InP based MWIR QWIPs is comparable to the best results reported in the literature for AlGaAs/InGaAs strained MWIR QWIPs [39]. Further improvement in the device performance can be expected if the diffraction grating structure is optimized.

On the other hand, the detailed characteristics of a large format strained InP/In$_{0.48}$Ga$_{0.52}$As QWIP FPA with a cut-off wavelength of 9.7 µm are also investigated. The FPA provided excellent characteristics with an impressively high quantum efficiency and large responsivity in the bias region where the detectivity is reasonably high. Applications such as tracking of rapidly moving targets or utilization of micro scanning for resolution enhancement call for high gain and responsivity due to the need for low integration times. While, this FPA offers sufficiently large conversion efficiency for such applications, it also provides bias adjustable detector gain increasing the degree of design freedom and flexibility. The FPA providing a background limited performance temperature higher than 65 K (*f*/1.5) satisfies the requirements of most low integration time/low background applications where AlGaAs/GaAs QWIPs suffer from low conversion efficiency. It should also be noted that this FPA is fabricated in the conventional QWIP structure with standard (cross type) grating. The possibility of light coupling efficiency (η) improvement through utilization of a corrugated structure [23] must be investigated in order to overcome the important limitation of QWIPs in short integration time applications.

The production yield of InP/InGaAs QWIP FPAs is not expected to be considerably different than that of GaAs based QWIPs. While one may presume that the fragility of InP increases the difficulty level of fabrication process especially at the substrate thinning stage, the substrate can completely and safely be removed with wet etching following mechanical lapping due to the availability of wet etchants highly selective between InP and InGaAs.

It can be expected that the combination of the AlInAs/InGaAs and InP/InGaAs material systems in the form of a MWIR/LWIR dual-band QWIP structure will provide important advantages by combining the individual desirable properties of these material systems. This issue will be discussed in the next chapter.

CHAPTER 4

DUAL BAND QWIP FPAs

The preceding chapter presented the characteristics of InP based single band MWIR and LWIR QWIP sensors both at pixel and FPA levels. While the AlInAs/InGaAs MWIR QWIPs provide desirable characteristics with a lattice matched structure, slightly strained LWIR InP/InGaAs QWIPs offer a bias adjustable gain (and conversion efficiency) along with high quantum efficiency. Combining the advantages of these sensors in the form of a MWIR/LWIR dual-band QWIP structure on InP substrate will provide characteristics superior to those of GaAs based dual-band QWIPs. It is the aim of this chapter to discuss the techniques through which InP based dual-band QWIPs can be constructed. This chapter is organized as follows. Section 4.1 discusses the need for dual-band thermal imaging while Section 4.2 investigates the potential of InP based QWIP structures for single bump voltage tunable FPAs along with a comparison with the characteristics of GaAs based voltage tunable dual-band QWIP structures. This section also presents the demonstration of a GaAs based voltage tunable dual-band QWIP FPA developed in collaboration with Y. Arslan in the course of his M. Sc. thesis work [64]. Section 4.3 presents the studied made toward the implementation of InP based three-contact dual-band QWIP FPAs along with the characteristics of the FPA

4.1 Dual/Multi-Band Sensors for Third Generation Thermal Imagers

Third generation thermal imagers with dual/multi-band operation capability are the prominent focus of the current research in the field of infrared detection. Third generation IR sensors are targeted to provide enhanced capabilities such as higher resolution, higher temperature sensitivity and multispectral imaging. Multispectral imaging is highly important for advanced IR imaging systems considering the fact

that the IR radiation from the objects is emissivity dependent. For a blackbody, whose emissivity is 1, detection in a single band is enough to calculate the absolute temperature of the object. However, the objects in the nature display emissivity values varying with wavelength. In order to discriminate the absolute temperature of such objects, detection in more than one band is necessary.

Multispectral imaging not only allows distinguishing the absolute temperature of the target but also enables advance image processing algorithms to further increase the sensitivity of the system. This is extremely important for identifying temperature difference between missile target, war heads, and decoys [71]. Multispectral IR focal plane arrays (FPAs) also play important roles in Earth and planetary remote sensing and astronomy [71].

Each atmospheric window has advantages and disadvantages over each other. MWIR window is less affected form water vapor, and MWIR sensors have found a wide utilization area in maritime applications. These sensors, if constructed in the form of very large format arrays, can also be used with very narrow field of view optics for long line of sight detection due to the desirable diffraction limit in the MWIR window. On the other hand, high photon contrast in the MWIR window dramatically decreases the dynamic range of the imaging system making it difficult to image cold and hot targets together. LWIR window gains from low scattering rate through the imaging path and high dynamic range arising from low photon contrast. It is also advantageous for the low background applications when the photon flux is not sufficient for MWIR detectors. However, the performance of a LWIR detector decreases as the humidity level increases. Hence, it can be postulated that a dual band IR imager combining the advantages of each band in a single detector will have better performance than a single-color IR imager. Such a sensor would operate in a wider range of ambient conditions and is expected to be more effective in defeating IR countermeasures such as smoke, camouflage and flares.

Even though multispectral detection can also be implemented with HgCdTe and Type-II SLS photodetectors, certain unique properties of QWIP such as narrow spectrum and tailorable peak detection wavelength make it a good candidate for

multi-band thermal imaging. These properties allow the construction of multi-band imagers without the need for filters to prevent crosstalk [42].

A multi-band QWIP can be formed by growing different epilayer stacks on top of another. Each stack in the structure operates to detect in a particular wavelength interval. A sample epilayer structure of a dual band QWIP is given in Fig.4.1.

Figure 4.1 General structure of MWIR/LWIR dual band QWIP

Dual-band QWIP FPAs based on various detection and fabrication approaches have been reported [42] [45] [46] [72]. The reports on dual-band QWIP FPAs mostly cover the three-contact (bump) approach. This approach offers simultaneous integration of the detector output in two different bands. However, the three-contact approach decreases the FPA fill factor and greatly complicates the fabrication process resulting in presumably lower yield. Indeed, the typical format of three-contact dual-band FPAs is typically limited to 320x256. Very recently, a megapixel dual-band QWIP FPA with two contacts on each pixel was reported [44]. However, the pitch of this FPA (30 µm) is still too large for allowing a reasonably small volume optics in the thermal imager.

If a dual-band QWIP can be fabricated through the standard FPA fabrication process utilizing only one indium bump for each pixel, the low cost nature of single band QWIPs can be extended to the third generation thermal imagers. In this case, it would be possible to construct large format dual-band FPAs with reduced pitch

values (such as 20 µm) and the resolution of the FPA would be limited only by the diffraction limit in the LWIR window. This would be possible, if the responsivity spectrum of the pixels could be switched between two different windows with the applied bias. This approach does not allow simultaneous integration. However, it still offers a reasonably wide application area where extremely high frame rates are not required [73]. In the following section, realization of an AlGaAs/InGaAs/GaAs MWIR/LWIR dual-band QWIP FPA with this approach will be presented.

4.2 Fabrication and Characterization of a Large Format Voltage Tunable QWIP FPA on GaAs Substrate

If a multi-quantum well (MQW) stack sensitive in the MWIR atmospheric window is connected in series with a LWIR sensitive stack, the spectral response of the resultant structure depends on the distribution of the applied bias voltage between these stacks and the relative responsivities of the stacks [74]. The distribution of the applied bias voltage between the two QWIPs (based on their resistances) and the relative responsivities of the QWIPs determine the spectral response of the structure [75]. This behaviour can be modeled by the equivalent circuit shown in Fig.4.2 [75].
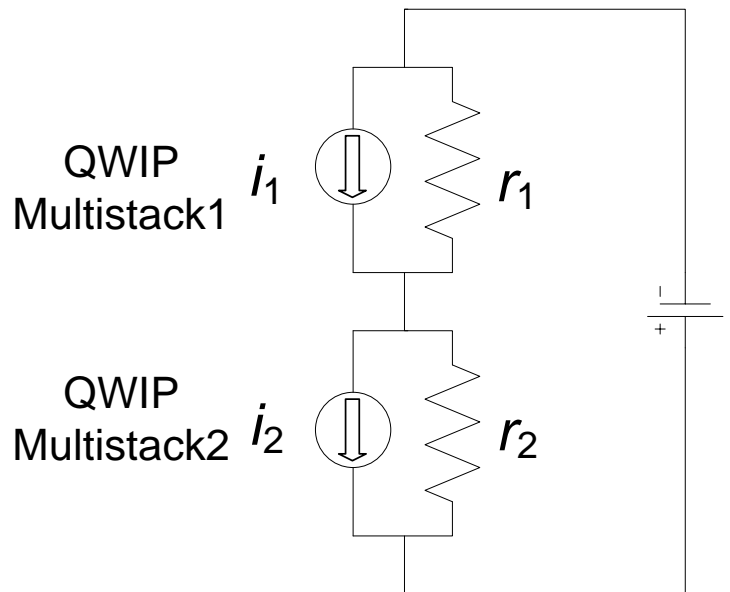

Figure 4.2 Equivalent circuit model of voltage tunable QWIP

The FPA epilayer structure was grown in our laboratory by solid source molecular beam epitaxy (MBE) on 4-inch semi-insulating GaAs substrate using the Riber Epineat MBE system. The substrate temperatures were 580 °C and 490 °C during the growth of LWIR and MWIR stacks respectively. III/V ratio was kept around 10 during the entire growth. The HRXRD Rocking Curve measurement and simulation results are in good agreement as shown in Fig. 4.3.
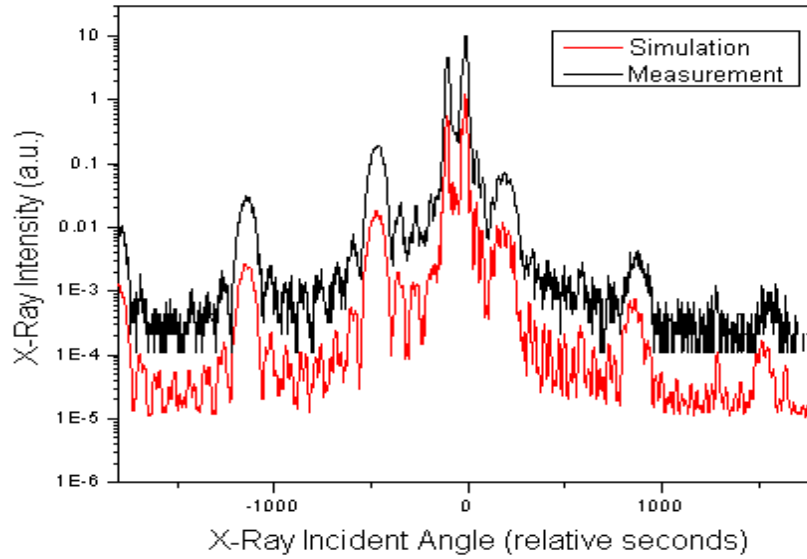
Figure 4.3 HRXRD Rocking curve measurement result of voltage tunable QWIP epilayer together with simulation results [64].

The epilayer structure includes two different MQW stacks constructed with the AlGaAs-InGaAs and AlGaAs-GaAs material system as shown in Fig.4.4 [73]. The LWIR stack consists of sixteen GaAs QWs sandwiched between 500 Å $Al_{0.27}Ga_{0.73}As$ barriers. The MWIR stack includes eight 5Å GaAs-32Å $In_{0.21}Ga_{0.79}As$-5Å GaAs QWs between 300 Å $Al_{0.36}Ga_{0.64}As$ barriers. The central 35 Å thick regions of the LWIR stack QWs are doped (with Si) at 5.2×10^{17} cm^{-3}. The InGaAs layers in the MWIR stack are doped at 8×10^{18} cm^{-3}. The two MQW stacks are grown between top and bottom GaAs contact layers doped to 1×10^{18} cm^{-3}. The MWIR and LWIR stacks are separated by a 0.5 μm thick doped ($N_D = 1 \times 10^{18}$ cm^{-3}) GaAs layer [73].

85
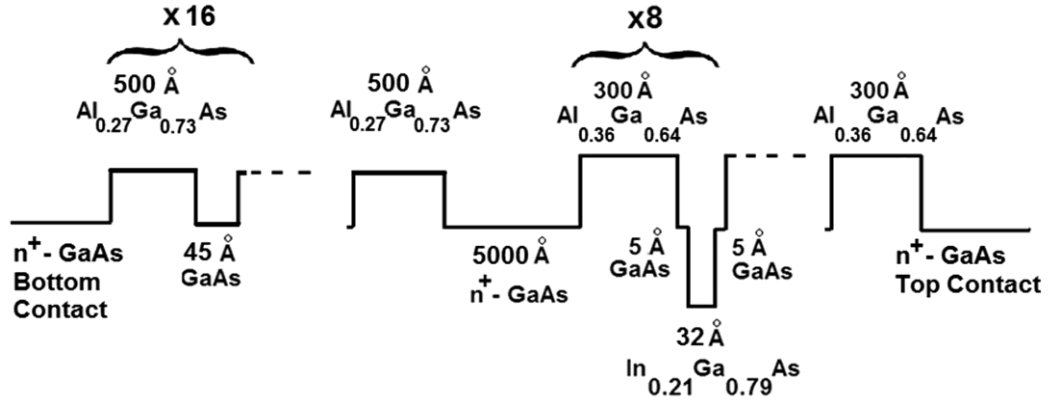
Figure 4.4 Conduction band edge profile of the dual color QWIP [73]

For the FPA fabrication, a 2-D optical grating structure tuned to the LWIR band and mesas with 25-μm pitch were defined. Following the formation of ohmic contacts, reflector, passivation, and under-bump metallization, indium bumps were formed through electroplating. The FPA was flip-chip bonded to Indigo ISC9803 ROIC, and the processing was completed by underfill injection and substrate thinning with a high-resolution lapping/polishing system [73]. In order to assess the characteristics of the FPA pixels accurately, pixel level characterization was performed on test QWIPs having the same dimensions ($\sim$21x21 μm^2) with the pixels of a typical large format FPA.

The spectral response of the test detectors under various reverse bias voltages (mesa top negative) at 65 K and 80 K is shown in Fig.4.5. The response under a 2 V bias peaks at 4.8 μm with a cutoff (50%) wavelength of 5.1 μm and $\Delta\lambda/\lambda_p$ = 13%. Under a 4 V bias, the peak responsivity wavelength is shifted to 8.4 μm with 8.95 μm cutoff wavelength and $\Delta\lambda/\lambda_p$ = 15% [73].
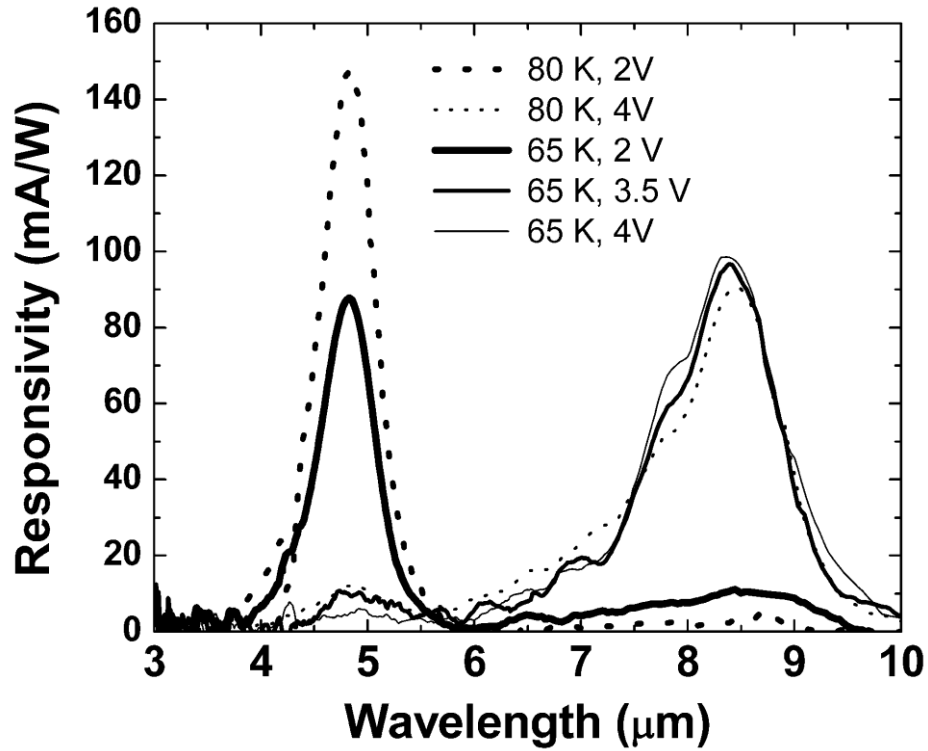
Figure 4.5 Spectral response of the FPA pixel-sized test detectors under various reverse bias voltages at ~80-K and 65-K sensor temperatures. A 750-K blackbody was used as the source for the FTIR system during 65-K measurements [73] [74].

The detectors show BLIP characteristic at 68 K up to a reverse bias voltage of 3.9 V with *f*/1.5 aperture and 300 K background. The peak detectivity is ~2×10^{10} cm√Hz/W and 7×10^{10} cm√Hz/W for LWIR (4 V) and MWIR (2 V) modes, respectively.

The FPA was characterized using a calibrated blackbody source and a Dewar (with *f*/1.5 aperture) connected to imager electronics yielding 14-bit digital output. Fig. 4.6 shows the measured mean NETD of the FPA versus detector bias with ~50% filled ROIC capacitors and *f*/1.5 optics at ~65-K FPA temperature. The FPA displayed NETDs of 32 mK in LWIR (3.5 V) and 20 mK in MWIR (2 V) modes with operabilities of 99.5% and 99%, respectively. Impressively low NETDs suggest that the individual performances of the MQW stacks are not significantly degraded by the series connection, allowing the fabrication of the FPA with the single-bump approach [73].
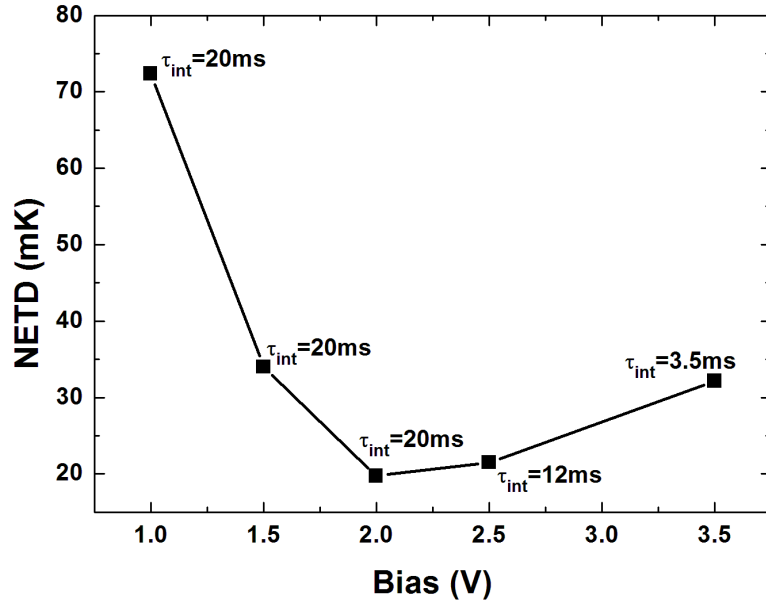
Figure 4.6 NETD of the FPA pixels versus detector bias voltage at ~ 65 K FPA temperature and 300 K background (*f*/1.5). The ROIC gain is adjusted to keep the ROIC capacitors approximately 50% filled at each bias voltage [73] [74].

Thermal images of a human, an 8–12 μm (LWIR) filter, and a soldering iron control unit recorded with the FPA in MWIR (2 V) and LWIR (3.5 V) modes are shown in Fig. 4.7. These thermal images were recorded with a wideband (3–12 μm) *f*/2.3 lens by manually changing the bias voltage applied to the FPA and keeping the as static as possible. The band pass filter is opaque in the MWIR mode where it is completely transparent in the LWIR mode which demonstrates the successful operation of the FPA [73].
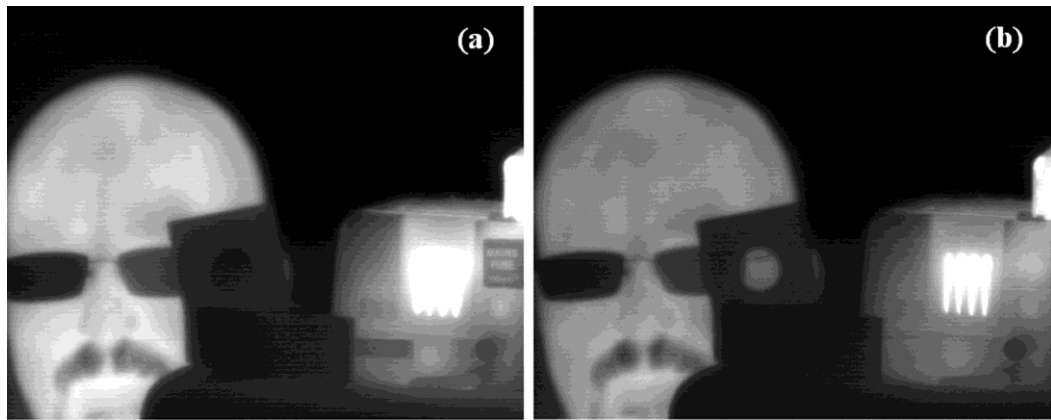
Figure 4.7 Thermal images of a human, an 8–12 μm (LWIR) bandpass filter, and a soldering iron control unit recorded with the FPA at ~65 K temperature (a) in MWIR (2 V) and (b) in LWIR (3.5 V) modes [73].

More detailed information on this work can be found in references [64] [73] [74]. The above results suggest that implementation of a dual-band QWIP FPA is feasible with the voltage tuning approach. The following part of this section will discuss the application of this technique to InP based QWIPs.

In order to assess the voltage tunable operation of InP based dual-band QWIPs, different structures with different period numbers and doping levels were grown with MBE. The best switching behavior was observed with a two-stack QWIP including a 16-period LWIR MQW stack with 54 Å thick $In_{0.51}Ga_{0.49}As$ QWs ($N_D=5.5 \times 10^{17}$ cm^{-3}) sandwiched between 400 Å InP barriers and a 10-period MWIR MQW stack with 22 Å thick $In_{0.53}Ga_{0.47}As$ QWs ($N_D=3 \times 10^{18}$ cm^{-3}) sandwiched between 300 Å $Al_{0.48}In_{0.52}As$ barriers. The top and bottom contact layers are $In_{0.53}Ga_{0.47}As$ doped to $N_D=1 \times 10^{18}$ cm^{-3}, and the two MQW stacks are separated by a 0.6 μm thick $In_{0.53}Ga_{0.47}As$ mid contact layer doped at the same level. The structure of the dual-band QWIP is given in Fig.4.8 [67]. After the growth of the wafer, 300 μm×300 $μm^2$ test detectors were fabricated.
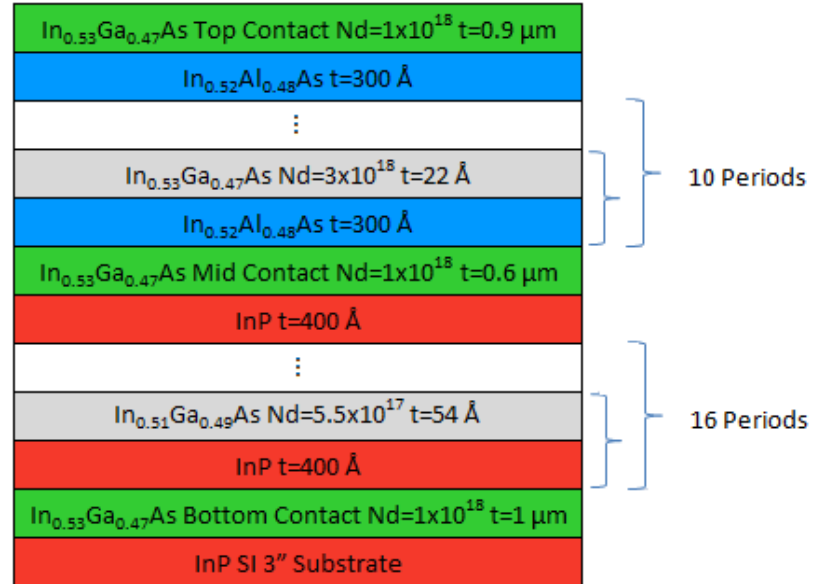
Figure 4.8 The structure of MWIR/LWIR QWIP

The normalized spectral response of the test detectors at 80 K is given in Fig. 4.9 for 2 V and 4 V biasing voltages [67]. While the detector provides MWIR dominated

spectral response under 2 V bias, the peak responsivity wavelength is shifted to 8.5 μm when the bias is increased to 4 V.
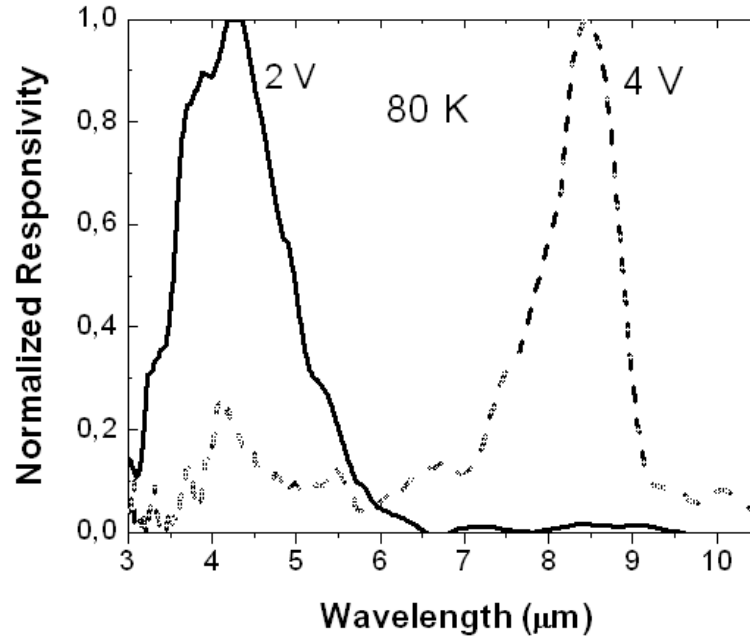
Figure 4.9 Normalized responsivity of large area (300x300 μm^2) detectors (without optical grating) at 80 K [67]

Serially connected QWIP stacks can be considered as serially connected resistors. The current of each stack is composed of dark and photo currents. At 80 K detector temperature, the dark currents are at significant level allowing different photocurrents to flow through the MWIR and LWIR stacks based on the voltage distribution which depends mostly on the dark currents of the stacks. Most of the applied voltage drops on the MWIR part under 2 V resulting in MWIR dominated spectral response. Under 4 V bias , on the other hand, the voltage drop on the LWIR stack is large enough to make the response LWIR dominant due to the higher responsivity of the LWIR part [67].

Fig. 4.10 shows the spectral responsivity of the detector at 65 K. It should be noted that the spectral response is dominated by the LWIR part and the voltage switchable spectral response behavior is no longer observable. This can be attributed to near BLIP operation which establishes a feedback between the responsivity (photocurrent) and the voltage drop on a stack [67] [75]. Under low bias voltages both MWIR and LWIR parts are likely to be BLIP leading to comparable photocurrents in the two-

stacks while most of the applied bias voltage drops on the MWIR part. Under 4 V bias, most of the bias voltage still drops on the MWIR part. The LWIR responsivity is slightly increased, while the relative responsivity of the MWIR part is weakened (which does not necessarily mean that the voltage drop on the MWIR part is decreased) [67].
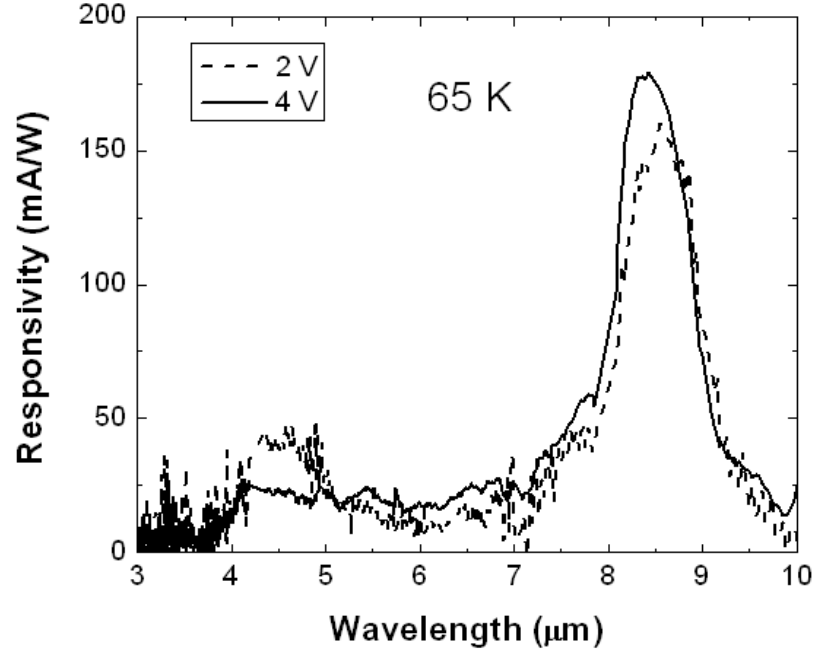
Figure 4.10 Normalized responsivity of large area (300x300 μm^2) detectors (without optical grating) at 65 K [67].

Due to the above reasons, the AlInAs/InGaAs MWIR-InP/InGaAs LWIR two-stack structure may not be promising for voltage tunable dual-band QWIPs at least with structures similar to the ones investigated in this work. However, this two-stack MQW structure displays high potential for three-contact dual-band FPAs due to the following reasons [67].

- AlInAs/InGaAs lattice matched MQW structure provides excellent imaging performance with desirable detector properties in the MWIR band
- InP/InGaAs MQW stack offers the flexibility of bias adjustable gain in a wide range including sufficiently high gain values for low background/high frame rate applications.

The following section will present the studies toward the realization of InP based three-contact dual-band QWIP FPAs.

4.3 Fabrication and Characterization of Three-Contact Dual Band InP QWIP FPA

The QWIP structure used for fabrication of three-contact dual-band QWIP FPA was grown with a solid source Riber Epineat MBE system on 3-inch semi insulating InP substrate. The LWIR stack contains 20 $In_{0.49}Ga_{0.51}As$ quantum wells (55 Å thick) sandwiched between 400 Å thick InP barriers. The quantum wells are n-type doped at $5x10^{17}$ cm^{-3}. The MWIR stack is formed of 10 periods of n-type doped $(5x10^{18}$ $cm^{-3})$ $In_{0.53}Ga_{0.47}As$ quantum wells (24 Å thick) surrounded by 300 Å thick $Al_{0.48}In_{0.52}As$ barriers. The top and bottom contact layers are $In_{0.53}Ga_{0.47}As$ doped to $N_D=1x10^{18}$ cm^{-3}, and the two MQW stacks are separated by a 0.5 μm thick $In_{0.53}Ga_{0.47}As$ mid contact layer doped at the same level. The structure of the dual-band QWIP is given in Fig. 4.11.
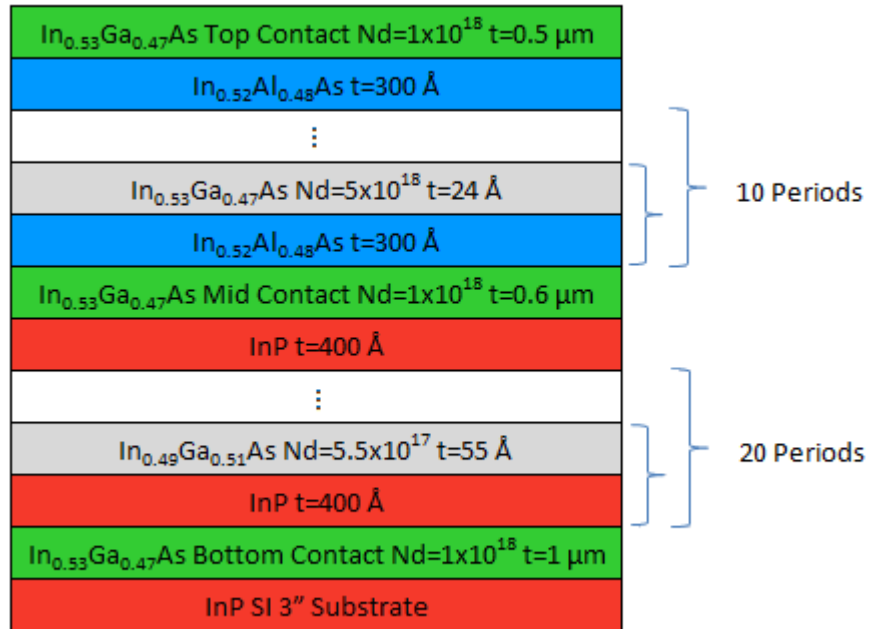
Figure 4.11 Dual-band QWIP epilayer structure used for the fabrication of three-contact QWIP FPA

After the growth of the structure, it was characterized with HRXRD in order to determine the layer thicknesses and mole fractions. The measurement data and simulation results perfectly agreed suggesting that the desired mole fractions and layer thicknesses were achieved. Figure 4.12 shows the HRXRD measurement data together with the simulation result.
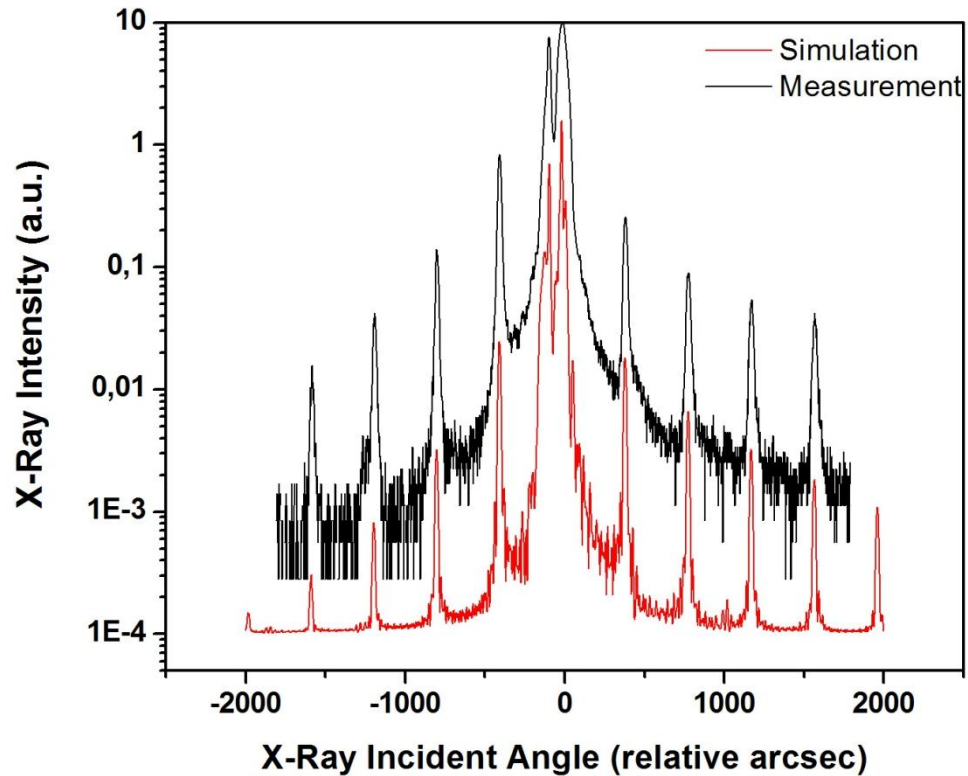
Figure 4.12 HRXRD Rocking curve measurement data of two stack QWIP structure together with simulation result

Following the HRXRD characterization, large area test detectors were fabricated and characterized. The fabrication process allowed the observation of the individual characteristics of the MWIR and LWIR stacks by contacting them independently from each other. Figure 4.13 and 4.14 shows the normalized spectral responses of MWIR and LWIR parts, respectively.
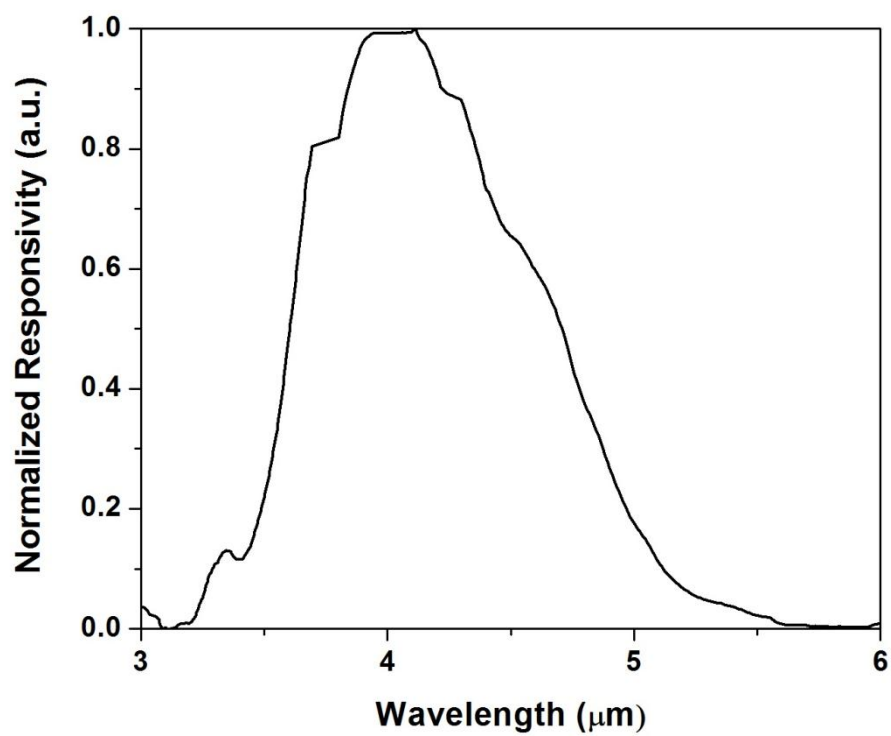
Figure 4.13 Normalized spectral response of MWIR stack
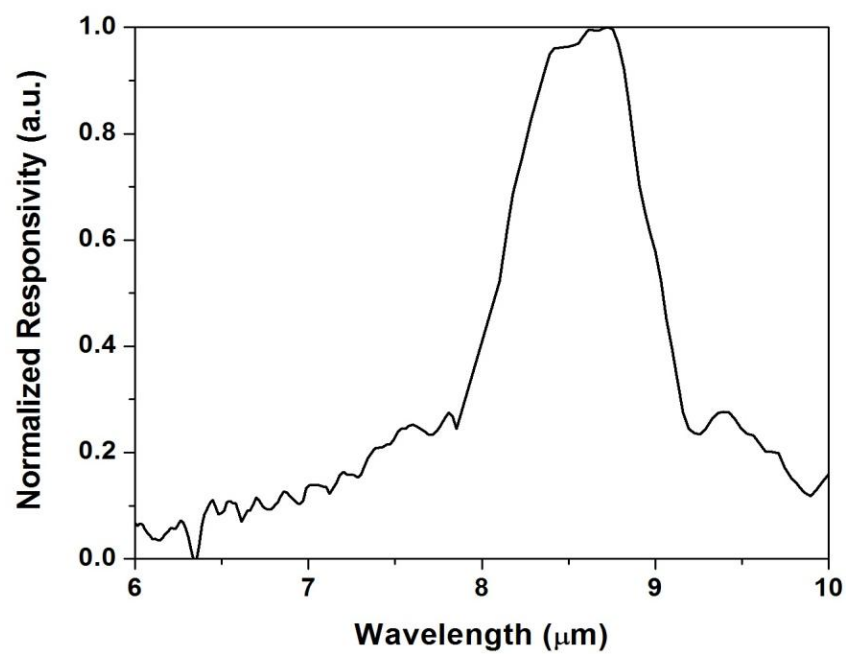
Figure 4.14 Normalized spectral response of LWIR stack

The three-contact FPA fabrication started with the formation of the alignment marks. Following the formation of alignment marks, LWIR tuned diffraction gratings were defined by optical lithography and dry etching with SI500 ICP-RIE system from SENTECH GmBH. Under chlorine chemistry based reactive ion etching conditions, there is difficulty in desorbing $InCl_x$ etch products in Cl_2 discharges unless the sample is heated to >200 ºC [76]. Even at elevated substrate temperatures, it is not possible to obtain vertical sidewalls [76]. Thus, CH_4/H_2 mixture became a widely used etch chemistry for InP based materials. However, this chemistry suffers from low etch rates, hydrogen passivation of near surface dopants and polymer deposition in the chamber and on the sample [76]. In some cases, it is completely impossible to remove the deposited polymere from the sample surface which decreases the yield dramatically. In this thesis work, a chlorine based etch process [76] was adopted properly for our ICP-RIE system in order to achieve acceptable etch rates without heating the sample. Complete etching process was performed at room temperature using BCl_3/N_2 mixture, thus photoresist could be used as a masking material.

The photographs of the ICP-RIE system and the diffraction gratings are given in Fig. 4.15 and 4.16 respectively.

Figure 4.15 SI500 ICP-RIE System installed in our laboratory
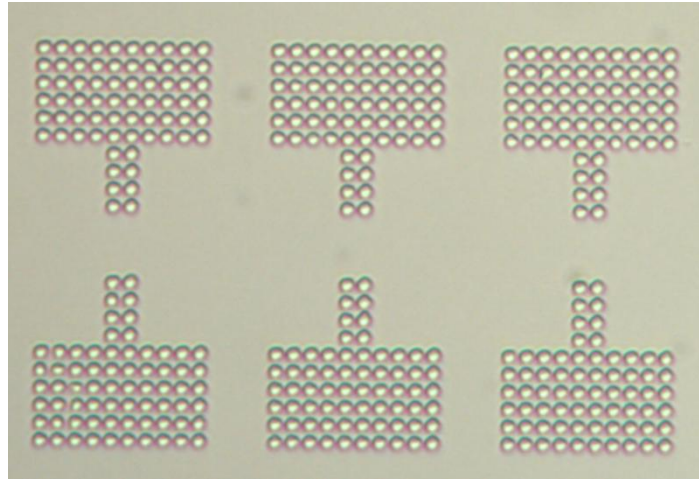
Figure 4.16 The photograph of diffraction grating structures taken under optical microscope

Following the formation of the diffraction gratings, the three step mesa etching was performed. First of all, the mesa structures were dry etched down to the mid contact. Then, another dry etching was performed until the bottom contact was reached. Finally, all the mesas were isolated from each other by dry etching down to the semi insulating substrate.

The fabrication was continued by evaporating ohmic contact metals on three-contact layers. A photograph of isolated mesa structures is shown in Fig. 4.17.
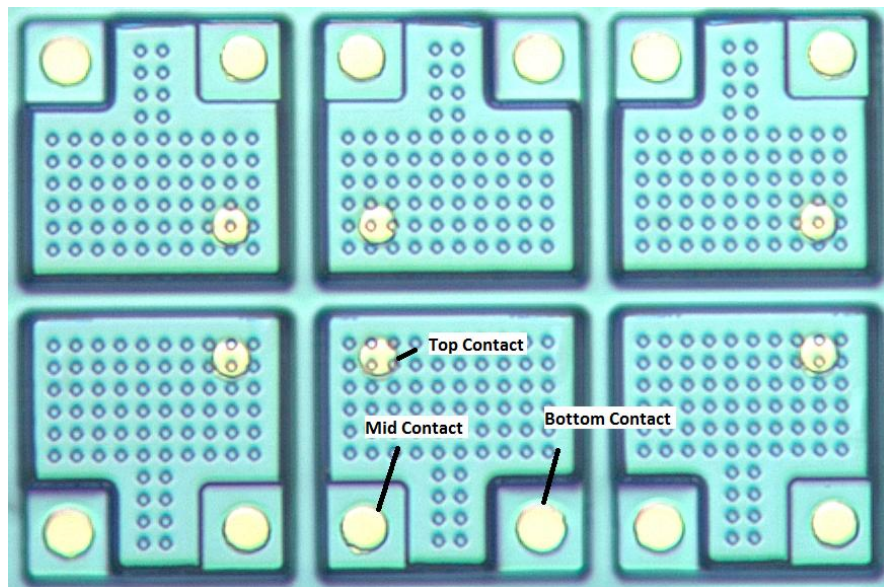
Figure 4.17 Optical microscope photograph of the isolated mesa structures and the ohmic contact metals

In order to reflect back the unabsorbed IR radiation into the active layer, reflector metal was evaporated on the mesa structures as shown in Fig 4.18.
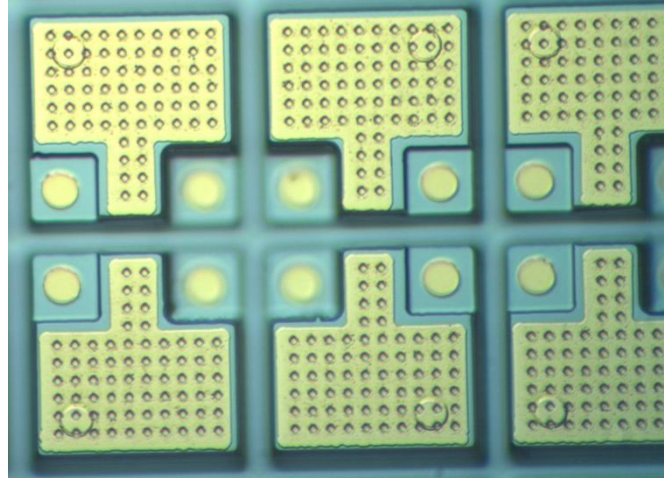
Figure 4.18 Photograph of mesa structures with reflector metal on top of them

Following the above described steps, Si_3N_4 was deposited on the sample as a passivation layer in order to minimize the surface leakages. Si_3N_4 was deposited with plasma enhanced chemical vapor deposition (PECVD) technique in METU-MEMS facility. The passivation layer on the ohmic contact points was opened with dry etching (CHF_3/O_2 chemistry) in order to provide contact to the ROIC.

Before electroplating of In bumps, an under bump metallization (UBM) layer was formed. This layer not only acts as a diffusion barrier for In but also carries the contact points in different parts to the mesa top. Finally, the In bumps were formed through electroplating resulting in a perfectly uniform In deposition. The photograph of the completed FPA is given in Fig. 4.19 showing the perfect height uniformity of the In bumps.
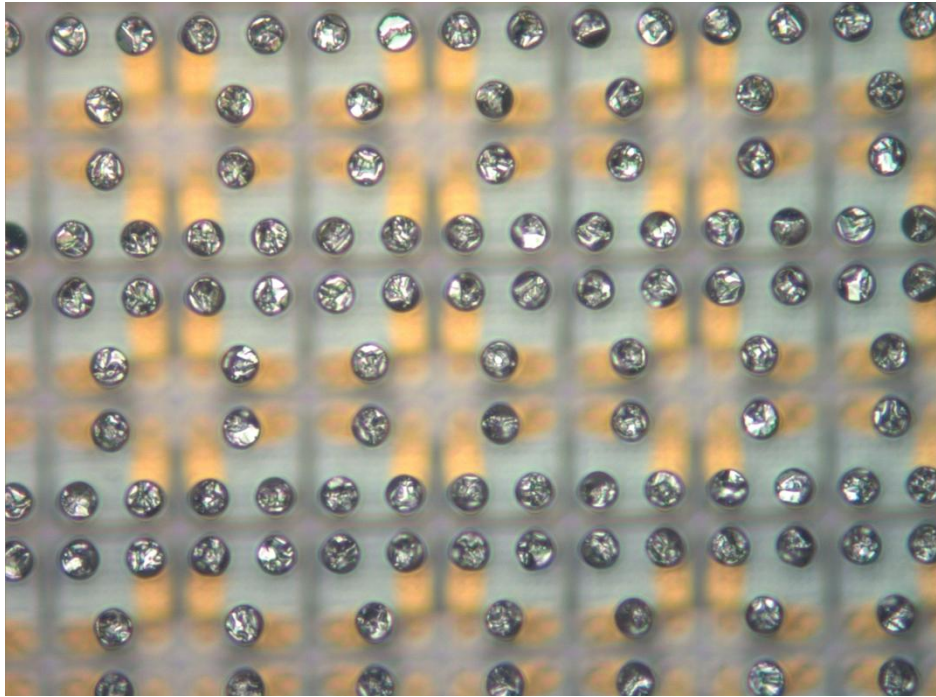
Figure 4.19 Sectional view of completed three-contact FPA

After the fabrication of the dual-band QWIP FPA was completed, the sample was diced and coupled to the ISC0006 ROIC from Indigo/FLIR Systems with flip- chip bonding technique. ISC0006 is a high performance CMOS ROIC for two color QWIPs [77]. The resolution of the ROIC is 320x256 with 40 µm pixel pitch with a shared unit cell. For each detector there is a p-channel direct injection input stage. The charge handling capacity of the ROIC is greater than 17e6 and 87e6 electrons for MWIR and LWIR bands respectively. The integration time, biasing voltage, and gain for each detector is adjusted independently through the serial control register. For full frame readout, the maximum achievable frame rate is 30 Hz. The unit cell contains two integration capacitors, one for each color, which also operate as sample and hold capacitors supporting snap shot integration. The unit cell signal is read out in charge mode by a column charge amplifier during the interline dead time [77].

Following the flip-chip bonding, underfill epoxy was injected between the FPA and ROIC, and the substrate was removed with a high resolution lapping/polishing system. The illustration of a dual-band FPA pixel flip-chip bonded to the ROIC unit cell is shown in Fig.4.20.
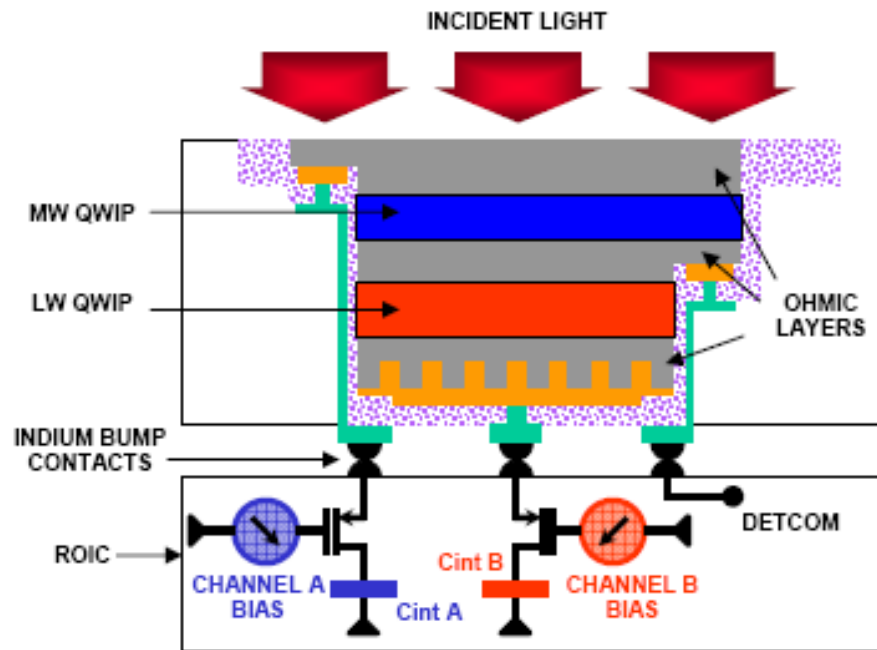
Figure 4.20 Illustration of a dual-band FPA pixel flip-chip bonded to the ROIC unit cell [77]

The detector was then installed in a laboratory type LN2 pour Dewar and characterized with Pulse Instruments System 7700. The setup is shown in Fig. 4.21.

Figure 4.21 The setup for characterizing dual-band three-contact FPA

System 7700 is a flexible system which allows adjusting of each clock and biasing signals individually. The analog output of the ROIC is fed back to the 14-bit analog-to-digital converter part of the unit and 14-bit digital data is displayed on the computer screen.

The MWIR stack of the dual-band FPA provided NETD value of 27 mK with *f*/1.5 optics and 19 ms integration time under 1.9 V bias voltage. The LWIR stack was biased with 0.75 V resulting in an NETD value of 29 mK with *f*/1.5 optics and 19 ms integration time. The operability of the MWIR stack was 95 % while it was 55% for the LWIR stack. The individual NETD histograms of MWIR and LWIR stacks are shown in Fig. 4.22 and 4.23, respectively. For operating pixels, the DC signal nonuniformities of the FPA in the MWIR and LWIR modes are 4% and 5%, respectively. NETD nonuformities are 24% (MWIR mode) and 46% (LWIR mode).

Low operability in the LWIR resulted from the nonuniform passivation thickness. The coating thickness is highly sensitive to the sample temperature [78]. The FPA sample was glued to a 4-inch Si carrier with a high temperature epoxy. The epoxy between the FPA sample and the carrier was not conformal resulting in a nonuniform temperature distribution on the sample during PECVD coating.
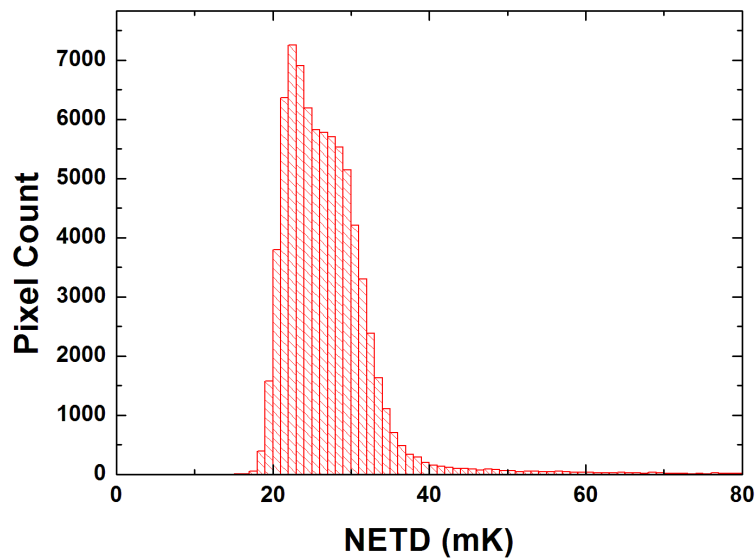
Figure 4.22 NETD histogram of the MWIR stack of the three-contact QWIP FPA. The mean NETD is 27 mK with *f*/1.5 optics, 19 ms integration time and 1.9 V bias voltage.
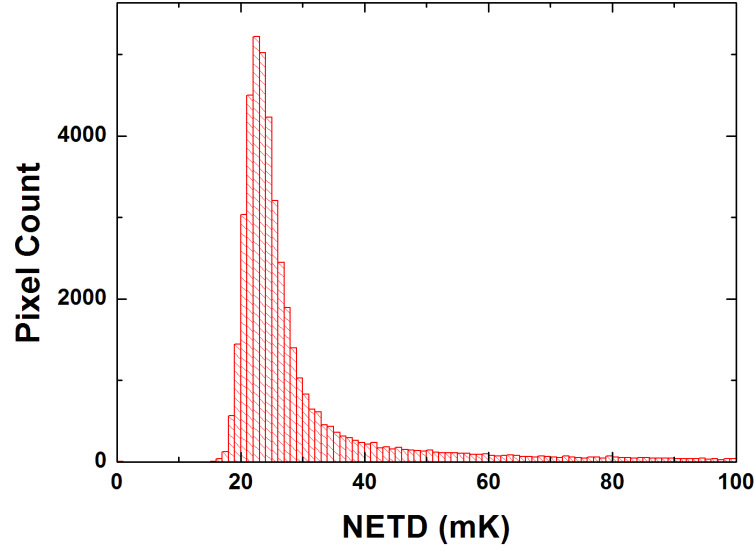
Figure 4.23 NETD histogram of the LWIR stack of the three-contact QWIP FPA. The mean NETD is 27 mK with *f/*1.5 optics, 19 ms integration time and 0.75 V bias voltage.

In conclusion, the FPA provides excellent sensitivity and uniformity demonstrating the feasibility of this sensor technology. It should be noted that it was not the objective of this work to achieve a fully operable FPA. The percentage of the operable pixels is sufficient to demonstrate the potential of InP material systems for dual-band FPAs using this technique.

It is also worth mentioning that due to the larger pitch size, three-contact ROICs provide larger capacitance sizes allowing higher integration times. This calls for large gain (responsivity) values in the detectors in order to be able to fill half of the ROIC capacitors under typical background conditions. InP based QWIPs, providing considerably larger gain and responsivity (when compared to GaAs based QWIPs), offer an important advantage for three-contact dual-band FPAs.

CHAPTER 5

CONCLUSION and FURTHER WORK

This thesis work reports the demonstration and detailed characterization of single and dual-band QWIP FPAs grown on InP substrates as well as their advantages over the standard GaAs based QWIPs. The conventional material systems used for MWIR and LWIR QWIPs are the AlGaAs/GaAs and AlGaAs/InGaAs heterostructures, respectively. While LWIR AlGaAs/GaAs QWIPs suffer from low conversion efficiency under high frame rate and/or low background conditions, MWIR AlGaAs/InGaAs QWIPs suffer from the degradations of lattice mismatched epitaxy due to considerable amount of strain introduced during the growth of the heterostructure. This thesis work has shown that alternative material systems on InP substrate display high potential for overcoming the limitations of the standard GaAs based QWIPs and extending the application area of this sensor technology in the field of high performance thermal imaging. When the low cost nature, maturity and excellent stability of the QWIP technology are considered, the results presented in this thesis are likely to have significant impact on the infrared sensing and imaging technology from both detector designer's and system engineer's points of view.

The important conclusions that can be drawn from this work can be summarized as follows.

1) While the cut off wavelength of the lattice matched $InP/In_{0.53}Ga_{0.47}As$ multi-quantum well structure falls short for LWIR thermal imaging [26], slight strain introduced to the InP/InGaAs material system by replacing the QW material $In_{0.53}Ga_{0.47}As$ with $In_{0.48}Ga_{0.52}As$ results in a desirable spectral response characteristics with ~9 and 9.7 μm peak and cut-off wavelengths, respectively [35].

The slightly strained InP/In$_{0.48}$Ga$_{0.52}$As QWIP FPA provides excellent characteristics with an impressively high peak quantum efficiency of 12% and broad spectral response ($\Delta\lambda/\lambda_p$=17%). The conversion efficiency of the device (η.g=20%) is larger than that of a typical AlGaAs/GaAs QWIP by a factor of four. The FPA demonstrated in this work provide both high quantum efficiency and a wide range of gain values (with sufficiently high detectivity) offering an additional flexibility in the design of thermal imagers especially for those to be operated under different conditions including high frame rates and/or low background environments. This is especially important for applications such as tracking of rapidly moving targets or utilization of micro scanning for resolution enhancement calling for high gain and responsivity due to the need for low integration times. The FPA providing a background limited performance temperature higher than 65 K (f/1.5) satisfies the requirements of most low integration time/low background applications where AlGaAs/GaAs QWIPs suffer from low conversion efficiency [35].

2) The FPA level investigations on the utilization of AlInAs/InGaAs on InP material system for MWIR QWIP applications have provided encouraging results. The tunability of the cut-off wavelength of AlInAs/InGaAs MWIR QWIPs by changing the quantum well width at lattice matched composition is experimentally demonstrated. The cut-off wavelength can be shifted up to ~5.0 μm with a QW width of 22 Å in which case very broad spectral response ($\Delta\lambda/\lambda_p$=~30%) and a reasonably high peak detectivity is achievable. The excellent sensitivity of the large format (640x512) FPA (14 mK NETD with f/2 aperture) display the potential of AlInAs/InGaAs QWIPs for thermal imaging applications in the MWIR band [29] [32] [67].

3) Combination of AlInAs/InGaAs (MWIR) and strained InP/InGaAs (LWIR) QWIP structures in the form of a dual-band sensor displayed high potential for satisfying the needs of the third generation thermal imagers with a low cost sensor technology as demonstrated by the encouraging results obtained with a mid format (320x256) dual-band QWIP FPA based on these material

systems. The FPA provided NETD (f/1.5, 65 K, 19 ms) values of 27 mK and 29 mK in the MWIR and LWIR modes with excellent DC signal uniformity.

Further work on the above issues can be listed as follows.

1) The detectivity of a QWIP is maximized at a specific doping level depending on the material properties. While QW doping dependency of QWIP detectivity has been extensively investigated for AlGaAs/GaAs QWIPs, there does not exist any related report on InP/InGaAs QWIPs to our knowledge. Therefore, the performance of the strained InP/InGaAs QWIP reported in this thesis can further be improved after this work. It should also be noted that the strained InP/InGaAs FPA was fabricated in the conventional QWIP structure with standard (cross type) grating. The possibility of light coupling efficiency (η) improvement through utilization of a corrugated structure [23] must be investigated in order to overcome the important limitation of QWIPs in short integration time applications. Furthermore, this FPA was coupled to a commercial ROIC (ISC 9803) from Indigo/FLIR systems with an electron capacity of 11 million electrons. As a result, the integration time should be kept low (in the order of hundred microseconds) when the detector is used with high gain while looking at 300 K background. If the charge storage capacitor of the ROIC can be increased further, the performance of the FPA may increase considerably by using larger integration times. It should be noted that higher *kTC* noise arising from larger capacitors will not be an important problem for InP based QWIPs because of the high gain of this material system (higher signal and noise levels at the detector stage).

2) It should also be kept in mind that optimizing the grating structure of MWIR AlInAs/InGaAs QWIPs will increase the performance of the detector by providing better coupling and quantum efficiency. The MWIR QWIP FPAs developed in this work are also coupled to ISC9803 ROIC. On the other hand, an ROIC optimized for MWIR QWIPs (with lower charge storage capacitor and lower noise) will also help to improve the sensor performance. As the total current of MWIR QWIPs is lower compared to the LWIR QWIPs, they can only fill a small portion of the integration capacitor while

looking at 300 targets with typical integration times. Thus, ROIC with smaller charge storage capacitor and lower *kTC* noise will be better for a MWIR QWIP.

3) Finally, the performance of the dual-band FPA can be increased by employing a bidirectional grating structure in order to maximize the coupling efficiency in both LWIR and MWIR bands.

REFERENCES

[1] FLIR Systems, ThermoVision SC4000-SC6000 User's Guide, September 2007.

[2] A. Rogalski, J. Antoszewski, and L. Faraone, "Third-generation infrared photodetector arrays," *Journal of Aplied Physics*, vol. 105, p. 091101, 2009.

[3] Cengiz Beşikci, "EE755 Infrared Devices and Systems," Lecture Notes 2008.

[4] Selçuk Özer, "InSb And InAsSb infrared photodiodes on alternative substrates and InP/InGaAs quantum well infrared photodetectors : pixel and focal plane array performance," Ph.D. Thesis 2005.

[5] Wikimedia Foundation. [Online]. http://en.wikipedia.org/wiki/Infrared

[6] Tayfun AKIN, "CMOS-based Thermal Sensors," in *CMOS-MEMS*, O. Brand, G. K. Fedder, C. Hierold, J. Kornivk, and O. Tabata H. Baltes, Ed.: Wiley-VCH, 2005, pp. 479-512.

[7] A. Fraenkel et al., "The architecture and performance of SCD's 17 µm pitch VOx µ-bolometer detector," *Proceedings of SPIE*, vol. 7298, p. 72980R, 2009.

[8] M. Hirota, Y. Nakajima, M. Saito, and M. Uchiyama , "120x90 element thermoelectric infrared focal plane array with precisely patterned au-black absorber," *Sensors and Actuators A: Physical*, vol. 135, no. 1, pp. 146-151, 2007.

[9] J-B. Chevrier, K. Baert and T. Slater , "An infrared pneumatic detector made by micromachining technology," *Journal of Micromechanics and Microengineering*, vol. 5, no. 2, pp. 193-195, 1995.

[10] M. Henini and M. Razeghi, Ed., *Handbook of Infrared Detection Technology*.: ELSEVIER, 2002.

[11] H. Schneider, M. Walther,C. Schonbein,R. Rehm, J. Fleissner,W. Pletschen,J. Braunstein,P. Koidl, G. Weimann,J. Ziegler,W. Cabanski , "QWIP FPAs for high-performance thermal imaging," *Physica E*, vol. 7, pp. 101-107, 2000.

[12] A. Rogalski, "Infrared detectors: status and trends," *Progress in Quantum Electronics*, vol. 27, no. 2-3, pp. 59-210, 2003.

[13] B-Y Tsaur, M Weeks, R Trubiano, P Pellegrini, and T-R Yew, "IrSi schottky-barrier infrared detectors with 10 μm cutoff wavelength," *Electron Device Letters*, vol. 9, no. 12, pp. 650-653, 1988.

[14] B.F. Levine, K.K. Choi, C.G. Bethea, J. Walker, R.J. Malik, , "New 10 μm infrared detector using intersubband absorption in resonant tunneling GaAlAs superlattices," *Appl. Phys. Lett.*, vol. 50, no. 16, pp. 1092-1094, 1987.

[15] R. Rehm, M. Walther, J. Schmitz, J. Fleißner, F. Fuchs, J. Ziegler, W. Cabanski , "InAs/GaSb superlattice focal plane arrays for high-resolution thermal imaging," *Opto-Electron. Rev.*, vol. 14, no. 1, pp. 19-24, 2006.

[16] A. Rogaslki, "Insight on quantum dot infrared photodetectors," *Journal of Physics: Conference Series*, vol. 146, p. 012030, 2009.

[17] H.C. Liu, "Quantum Dot Infrared Photodetector," *Opto-Electronics Review*, vol. 11, no. 1, pp. 1-5, 2003.

[18] H. Schneider, H.C. Liu , *Quantum Well Infrared Photodetectors: Physics and Appliccations*.: Springer Series in Optical Sciences, 2007.

[19] Wikimedia Foundation. [Online]. http://en.wikipedia.org/wiki/Pink_noise

[20] S.D. Gunapala and S.V. Bandara, "Quantum Well Infrared Photodetector (QWIP) Focal Plane Arrays," *Semiconductors and Semimetals*, vol. 62, pp. 1-83, 1999.

[21] W.A. Beck, "Photoconductive gain and generation-recombination noise in multiple-quantum-well infrared detectors," *Applied Physics Letters*, vol. 63, pp. 3589-3591, 1993.

[22] K.K. Choi, *The Physics of Quantum Well Infrared Photodetectors*.: World Scientific Publishing, 1997.

[23] D.P. Forrai, D.W. Endress, K.K. Choi, and J.J. O'Neill. (2008) 26th Army Science Conference. [Online]. http://www.asc2008.com/manuscripts/N/NO-01.pdf

[24] B.F. Levine, "Quantum Well Infrared Photodetectors," *J. Appl. Phys.*, vol. 74, no. 8, pp. R1-R81, 1993.

[25] (2010) EE 174 Semiconductor Optoelectronics UCLA Electrical Engineering Department. [Online]. http://www.ee.ucla.edu/~wu/ee174/images/Bandgap-vs-Lattice%20Constant.jpg

[26] O.O Cellek, S. Ozer, and C. Beşikci, "High Responsivity InP/InGaAs Quantum Well Infrared Photodetectors: Characteristics and Focal Plane Array Performance," *IEEE Journal of Quantum Electronics* , vol. 41, pp. 980-985, 2005.

[27] S. Ozer, U. Tumkaya, B. Asici, and C. Besikci, "Demonstration and Performance Assessment of Large format InP-InGaAsP Quantum Well Infrared Photodetector Focal Plane Array," *IEEE Journal of Quantum Electronics*, vol. 43, pp. 709-713, 2007.

[28] O.O. Cellek and C. Beşikci, "Detailed Investigation of Electron Transport, Capture and Gain in Al 0.3 Ga 0.7 As/GaAs Quantum Well Infrared Photodetectors," *Semiconductor Science and Technology*, vol. 19, pp. 183-190, 2004.

[29] M. Kaldırım, Y. Arslan, S.U. Eker, and C. Beşikci, "Lattice Matched AlInAs-InGaAs Mid-wavelength QWIPs: Characteristics and Focal Plane Array Performance," *Semiconductor Science and Technology*, vol. 23, p. 085007, 2008.

[30] A. Cho, "Film Deposition by Molecular Beam Techniques," *J. Vac. Sci. Tech.*, vol. 8, pp. S31-S38, 1971.

[31] MBE Growth. [Online].
http://projects.ece.utexas.edu/ece/mrc/groups/street_mbe/mbechapter.html

[32] Melih Kaldırım, "Dual and Single Color Mid-Wavelength Infrared Quantum Well Photodetectors," M.Sc. Thesis 2008.

[33] M.Z. Tidrow, "Type II strained layer superlattice: A potential future IR solution," *Infrared Physics and Technology*, vol. 52, pp. 322-325, 2009.

[34] M. Razeghi et al., "Recent Advances in LWIR Type-II InAs/GaSb Superlattice Photodetectors and Focal Plane Arrays at the Center for Quantum Devices," *Proceedings of the IEEE*, vol. 97, pp. 1056-1066, 2009.

[35] S.U. Eker, Y. Arslan, A.E. Onuk, and C Beşikci, "High Conversion Efficiency InP/InGaAs Strained Quantum Well Infrared Photodetector Focal Plane Array With 9.7 μm Cut-Off for High-Speed Thermal Imaging," *IEEE Journal of Quantum Electronics*, vol. 46, pp. 164-168, 2010.

[36] B.F. Levine et al., "Photoexcited escape probability, optical gain, and noise in quantum well infrared photodetectors," *Journal of Applied Physics*, vol. 72, pp. 4429-4443, 1992.

[37] Y. Yang et al., "Optimal Doping Density for Quantum Well Infrared Photodetector Performance," *IEEE Journal of Quantum Electronics*, vol. 45, pp. 623-628, 2009.

[38] QWIP Tech. [Online].
http://www.qwip.com/images/stories/PDFs/1Kx1KFormatFpaSpecifications.pdf

[39] S.D. Gunapala et al., "1024x1024 pixel mid-wavelength and long-wavelength infrared QWIP focal plane arrays for imaging applications," *Semiconductor Science and Technology*, vol. 20, pp. 473-480, 2005.

[40] B. Simolon et al., "High performance two-color one megapixel CMOS ROIC for QWIP detectors," *Infrared Physics and Technolgy*, vol. 52, pp. 391-394, 2009.

[41] A. Goldberg et al., "Dual Band QWIP MWIR/LWIR Focal Plane Array Test Results," *Proceedings of SPIE*, vol. 4029, p. 276, 2000.

[42] M. Sundaram et al., "Two-color quantum well infrared photodetector focal plane arrays," *Infrared Physics and Technology*, no. 42, pp. 301-308, 2001.

[43] H. Schneider et al., "Dual-band QWIP focal plane array for the second and third atmospheric windows," *Infrared Physics and Technology*, no. 47, pp. 53-58, 2005.

[44] S.D. Gunapala et al., "1024x1024 Format pixel co-located simultaneously readable dual-band QWIP focal plane," *Infrared Physics and Technology*, vol. 52, pp. 395-398, 2009.

[45] S.V. Bandara et al., "Four-band quantum well infrared photodetector array," *Infrared Physics and Technolgy*, vol. 44, pp. 369-375, 2003.

[46] E. Varley et al., "Single bump, two-color quantum dot camera," *Applied Physics Letters*, vol. 91, p. 081120, 2007.

[47] D. King et al., "Third Generation 1280x720 FPA Development Status at Raytheon Vision Systems," *Proceedings of SPIE*, vol. 6206, 2006.

[48] R. Rehm et al., "Dual-color thermal imaging with InAs/GaSb superlattices in midwavelength infrared spectral range," *Electronics Letters*, vol. 42, pp. 577-578, 2006.

[49] S. Adachi, "GaAs,AlAs,and AlxGa1-xAs: Material parameters for use in research and device applications," *Journal of Applied Physics*, vol. 58, pp. R1-R29, 1985.

[50] T.P. Pearsall, *GaInAsP Alloy Semiconductors*.: John Wiley and Sons, 1982.

[51] O.O. Cellek, S. Memis, U. Bostanci, S. Ozer, and C. Besikci, "Gain and transient photoresponse of quantum well infrared photodetectors: a detailed ensemble Monte Carlo study," *Physica E*, vol. 24, pp. 318-327, 2004.

[52] J. Jiang et al., "Demonstration of 256x256 focal plane array based on Al-Free GaInAs-InP QWIP," *IEEE Phootnics Technology Letters*, vol. 15, pp. 1273-1275, 2003.

[53] Y. Gusakov, E. Finkman, G. Bahir, and D. Ritter, "The effect of strain in InP/InGaAs quantum-well infrared photodetectors on the operating wavelength," *Applied Physics Letters*, vol. 79, pp. 2508-2510, 2001.

[54] S.D. Gunapala, Levine B.F., D. Ritter, R. Hamm, and M.B. Panish, "Lattice matched InGaAsP/InP long-wavelength quantum-well infrared photodetectors," *Applied Physics Letters*, vol. 60, pp. 636-638, 1992.

[55] S.D. Gunapala, Levine B.F., D. Ritter, R. Hamm, and M.B. Panish, "InGaAs/InP long wavelength quantum well infrared photodetectors," *Applied Physics Letters*, vol. 58, pp. 2024-2026, 1991.

[56] J.Y. Andersson, L. Lundqvist, Z.F. Paska, K. Streubel, and J. Wallin, "Long-wavelength quantum-well infrared detectors based on intersubband transitions in InGaAs/InP quantum wells," *Proceedings of SPIE*, vol. 162, pp. 216-226, 1992.

[57] C. Jelen, S. Slivken, T. David, M. Razeghi, and G.J. Brown, "Noise performance of InGaAs-InP quantum-well infrared photodetectors," *IEEE Journal of Quantum Electronics*, vol. 34, pp. 1124-1128, 1998.

[58] A. Majumdar et al., "High-responsivity high-gain In0.53Ga0.47As-InP quantum-well infrared photodetectors grown using metal-organic vapor phase epitaxy," *IEEE Journal of Quantum Electronics*, vol. 41, pp. 872-878, 2005.

[59] D.K. Sengupta et al., "Growth and characterization of n-type InP/InGaAs quantum well infrared photodetectors for response at 8.93 μm," *Journal of Electronic Materials*, vol. 26, pp. 1376-1381, 1997.

[60] B.F. Levine et al., "InGaAs/InAlAs multiquantum well intersubband absorption at a wavelength of λ=4.4 μm," *Applied Physics Letters*, vol. 52, pp. 1481-1483, 1988.

[61] G. Hasnain, B.F. Levine, D.L. Sivco, and A.Y. Cho, "Mid-infrared detectors in the 3-5 μm band using bound to continuum state absorption in InGaAs/InAlAs multiquantum well structure," *Applied Physics Letters*, vol. 56, pp. 770-772, 1990.

[62] A. Fathimulla, H. Hier, L. Aina, T. Worchesky, and P. Uppal, "InP-based multi-wavelength QWIP technology," *Proceedings of SPIE*, vol. 5406, pp. 589-599, 2004.

[63] S. Ozer, U. Tumkaya, and C. Besikci, "Large Format AlInAs-InGaAs Quantum Well Infrared Photodetector Focal Plane Array for Midwavelength Infrared Thermal Imaging," *IEEE Photonics Technology Letter*, vol. 19, pp. 1371-1373, 2007.

[64] Yetkin Arslan, "Large format dual-band quantum well infrared photodetector focal plane arrays," M.Sc. Thesis 2009.

[65] Introduction to X-Ray Diffraction. [Online].
http://www.mrl.ucsb.edu/mrl/centralfacilities/xray/xray-basics/index.html

[66] M. McElhinev and C.R. Stanley, "Reduced indium incorporation during the MBE growth of In(Al,Ga)As," *Electronics Letters*, vol. 29, pp. 1302-1304, 1993.

[67] S.U. Eker, Y. Arslan, M. Kaldırım, and C. Beşikci, "QWIP FPAs on InP Substrates for Single and Dual Band Thermal Imagers," *Infrared Physics and Technology*, vol. 52, pp. 385-390, 2009.

[68] V. Donchev, J.C. Bourgoin, and P. Bois, "Dark current through GaAs/AlGaAs multiple quantum wells," *Semicondcutor Science and Technology*, vol. 17, pp. 621-624, 2002.

[69] G. Gaussorgues, *Infrared Thermography*.: Chapman and Hall, 1994.

[70] R. Rehm, H. Schneider, M. Walther,P. Koidl,G. Weimann , "Avalanche multiplication due to impact ionization in quantum-well infrared photodetectors: A quantitative approach," *Applied Physics Letters*, vol. 82, pp. 2907-2909, 2003.

[71] A. Rogalski, "Competetive Technologies of Third Generation Infrared Photon Detectors," *Opto-Electronics Review*, vol. 14, pp. 87-101, 2006.

[72] S. Krishna et al., "Demonstration of a 320x256 two-color focal plane array using InAs/InGaAs quantum dots in well detectors," *Applied Physics Letters*, vol. 86, pp. 193501/1-3, 2005.

[73] S.U. Eker, M. Kaldırım, Y. Arslan, and C. Beşikci, "Large Format Voltage Tunable Dual-Band Quantum-Well Infrared Photodetector Focal Plane Array For Third Generation Thermal Imagers," *IEEE Electron Device Letters*, vol. 29, pp. 1121-1123, 2008.

[74] Y. Arslan, S.U. Eker, M. Kaldırım, and C. Beşikci, "Large Format Voltage Tunable Dual-Band QWIP FPAs," *Infrared Physics and Technology*, vol. 52, pp. 399-402, 2009.

[75] L.C. Lenchyshyn, H.C. Liu, M. Buchanan, and Z.R. Wasilewski, "Voltage-tuning in multi-color quantum well infrared photodetector stacks," *Journal of Applied Physics*, vol. 79, pp. 8091-8097, 1996.

[76] T. Maeda et al., "Inductively coupled plasma etching of III-V semiconductors in BCl3-based chemistries. II. InP,InGaAs,InGaAsP,InAs and AlInAs," *Applied Surface Science*, vol. 143, pp. 183-190, 1999.

[77] J. Bundas et al. (2006) Readout Integrated Circuit - ISC0006. [Online]. http://www.corebyindigo.com/PDF/SPIE/2-color_submission.pdf

[78] K. Byungwhan, P. Kyungyoung, and L. Dukwoo, "Use of neural network to model the deposition rate of PECVD-silicon nitride films ," *Plasma Soources Science and Technology*, vol. 14, pp. 83-88, 2005.

[79] R. Rehm et al., "Dual-color thermal imaging with InAs/GaSb superlattices in midwavelength infrared spectral range," *Electronics Letters*, vol. 42, pp. 577-578, 2006.

[80] I. Bar-Joseph et al., "Quantum-confined Stark effect in InGaAs/InP quantum wells grown by organometallic vapor phase epitaxy," *Applied Physics Letters*, vol. 50, pp. 1010-1012, 1987.

[81] M. Kaldırım, S.U. Eker, Y. Arslan, Ü. Tümkaya, and C. Beşikci, "Large Format Voltage Tunable Dual Color Midwavelength Infrared Quantum Well Infrared Photodetector Focal Plane Array," *IEEE Photonics Technology Letters*, vol. 20, pp. 709-711, 2008.

CIRRUCULUM VITAE

PERSONAL INFORMATION

Surname, Name: Eker, Süleyman Umut
Nationality: Turkish (TC)
Date and Place of Birth: 8 November 1977 , Sivas
Marital Status: Married
Phone: +90 312 210 45 17
Fax: +90 312 210 23 04
email: umuteker@hotmail.com

EDUCATION

Degree	Institution	Year of Graduation
M.Sc.	Cumhuriyet University	2004
B.Sc.	Dokuz Eylül University	2001
High School	Sivas Selçuk Anadolu High School	1996

WORK EXPERIENCE

Year	Place	Enrollment
2005-Present	Middle East Technical University	Research Assistant
2001-2005	Cumhuriyet University	Research Assistant

FOREIGN LANGUAGES

Advanced English, Beginner German

JOURNAL PUBLICATIONS

1. S. U. Eker, Y. Arslan, A.E. Onuk and C. Besikci, "High Conversion Efficiency InP/InGaAs Strained Quantum Well Infrared Photodetector Focal Plane Array With 9.7 μm Cut-Off for High-Speed Thermal Imaging", *IEEE Journal of Quantum Electronics*, vol 46, pp.164-168, 2010

2. S. U. Eker, Y. Arslan, M. Kaldirim and C. Besikci, "QWIP FPAs on InP Substrates for Single and Dual Band Thermal Imagers", *Infrared Physics and Technology*, vol 52, pp.385-390, 2009

3. Y. Arslan, S. U. Eker, M. Kaldirim and C. Besikci, "Large Format Voltage Tunable Dual-Band QWIP FPAs", *Infrared Physics and Technology* , vol 52, pp.399-402, 2009

4. S.U. Eker, M. Kaldırım, Y.Arslan and C. Besikci, "Large Format Voltage Tunable Dual-Band Quantum-Well Infrared Photodetector Focal Plane Array For Third Generation Thermal Imagers", *IEEE Electron Device Letters*, vol. 29, pp. 1121-1123, 2008

5. M. Kaldırım, Y. Arslan, S. U. Eker and C. Besikci, "Lattice Matched AlInAs-InGaAs Mid-wavelength QWIPs: Characteristics and Focal Plane Array Performance, *Semiconductor Science and Technology*, vol. 23, 085007, 2008.

6. M. Kaldırım, S. U. Eker, Y. Arslan, U. Tumkaya and C. Besikci, "Large Format Voltage Tunable Dual Color Midwavelength Infrared Quantum Well Infrared Photodetector Focal Plane Array", *IEEE Photonics Technology Letters*, vol. 20, pp.709-711, 2008.

7. S.U. Eker, M. Hostut, Y. Ergun, İ. Sökmen "A New Approach to Quantum Well Infrared Photodetectors: Staircase Like Quantum Well and Barriers", *Infrared Physics and Technology*, 48**,** *Issue 2*, 2006, 101-108

8. Y. Ergun, M. Hostut, S.U. Eker, İ. Sökmen "Broadband Staircase Quantum Well Infrared Photodetector with Low Dark Current", *Infrared Physics and Technology*, 48**,** *Issue 2*, 2006, 109-114

9. Y. Ergun, M. Hostut, S.U. Eker, İ. Sökmen "Intersubband Electron Transport Across a Staircase Potrential Containing Quantum Wells: Light Emission", *Superlattices and Microstructers,* 37*, Issue 3,* 2005*,*163-170

HOBBIES

Cinema, fishing, sports